Large enhancement of capacitance driven by electrostatic image forces

A DISSERTATION
SUBMITTED TO THE FACULTY OF THE GRADUATE SCHOOL
OF THE UNIVERSITY OF MINNESOTA
BY

Matthew Scott Loth

IN PARTIAL FULFILLMENT OF THE REQUIREMENTS
FOR THE DEGREE OF
Doctor of Philosophy

Boris Shklovskii

April, 2011

Acknowledgements

At the end of my graduate school career, as I reflect upon my development as a scientist, it is clear that I owe my adviser, Boris Shklovskii, the largest debt of thanks. In retrospect, when I began working with him four years ago, I did not understand what it meant to do theoretical physics. The evolution of my understanding has occurred through a process best compared with learning a language through immersion; Boris has been extremely generous with his time, devoting hours a day to working directly with all of his students. It is during these discussions, working side by side, that I have developed my physics intuition and ultimately learned what it means to make an original scientific contribution.

This thesis is the result of a long term collaborative effort with Boris and my co-worker Brian Skinner. I am thankful to Brian for his many contributions, insights and helpful conversations. I would be remiss not to thank Toan Nguyen for providing me the code for my very first Monte Carlo simulation, remnants of which still remain even in my most recent simulations. Thanks are also in order for my committee members, Charles Campbell, Cheng-Cher Huang, and Paul Ruden. Additionally, I have appreciated the years of financial support from the William I. Fine Theoretical Physics Institute as well as the Physics Department.

I could not have succeeded as a graduate student without the support of my loving family. My wife Katie has enthusiastically encouraged me when I struggled, celebrated with me when I succeeded, and in general kept our lives together when I was too busy to realize the car needed an oil change, the fridge was empty, and the rent needed to be paid. She did all of this while also being a Ph.D. student and a wonderful mother to our son, Charlie. Charlie's bright smile and high energy hugs have made me quicker at my work because I can't wait to see him at the end of every work day; thanks for your

help, Charlie.

Obtaining a Ph.D. is an accomplishment that is built on more than just the years in graduate school; I am deeply thankful to my parents, Don and Lois, for all the years of consistent love, encouragement, support and advice that have helped make me successful. Where would I be without my Mom reminding me to take time for myself? How far would I have made it without my Dad's stubbornness and refusal to give up on a problem? To my brother, Chris, I am thankful for his unwaivering support as I continued to go to more and more school. Having grown up very near to many of my grandparents, aunts, uncles and cousins, I have appreciated everyones encouragement through the years, and their understanding as I have been too busy to visit as often as I would have liked. I have also been very lucky to receive a great deal of support from all of my Katie's family.

At its best, graduate school is about balance; finding sometime to leave the work behind and enjoy the company of good friends. Mike, Ania, Tom, Laura, Tanner, Elizabeth, Seth, Eric and Annie, if I departed from graduate school without my diploma, but with our friendship, it would have been time well spent.

Finally, I need to thank my high school physics teacher, Patricia Westphal. Her enthusiasm for physics was infectious, her teaching was engaging, and her influence was apparently long lasting.

Dedication

To my wife Katie, our son Charlie, and our new baby.
The world is vast and full of rich experiences; let us never forget to be curious.

Abstract

The purpose of this thesis is to examine the role of electrostatic images in determining the capacitance and the structure of the electrostatic double layer (EDL) formed at the interface of a metal electrode and an electrolyte. Current mean field theories, and the majority of simulations, do not account for ions to form image charges in the metal electrodes and claim that the capacitance of the double layer cannot be larger than that of the Helmholtz capacitor, whose width is equal to the radius of an ion. However, in some experiments, and simulations where the images are included, the apparent width of the capacitor is substantially smaller.

Monte Carlo simulations are used to examine the interface between a metal electrode and a room temperature ionic liquid (RTIL) modeled by hard spheres (the "restricted primitive model"). Image charges for each ion are included in the simulated electrode. At moderately low temperatures the capacitance of the metal/RTIL interface is so large that the effective thickness of the electrostatic double-layer is up to 3 times smaller than the ion radius. To interpret these results, an approach is used that is based on the interaction between discrete ions and their image charges, which therefore goes beyond the mean-field approximation. When a voltage is applied across the interface, the strong image attraction causes counterions to condense onto the metal surface to form compact ion-image dipoles. These dipoles repel each other to form a correlated liquid. When the surface density of these dipoles is low, the insertion of an additional dipole does not require much energy. This leads to a large capacitance C that decreases monotonically with voltage V, producing a "bell-shaped" $C(V)$ curve. In the case of a semi-metal electrode, the finite screening radius of the electrode shifts the reflection plane for image charges to the interior of the electrode resulting in a "camel-shaped" $C(V)$ curve, which is parabolic near $V = 0$, reaches a maximum and then decreases. These predictions are in qualitative agreement with experiment.

A similarly simple model is employed to simulate the EDL of superionic crystals. In this case only small cations are mobile and other ions form an oppositely charged background. Simulations show an effective thickness of the EDL that may be 3 times

smaller than the ion radius. The weak repulsion of ion-image dipoles again plays a central role in determining the capacitance in this theory, which is in reasonable agreement with experiment.

Finally, the problem of a strongly charged, insulating macroion in a dilute solution of multivalent counterions is considered. While an ideal conductor does not exist in the problem, and no images are explicitly included, simulations demonstrate that adsorbed counterions form a strongly correlated liquid of at the surface of the macroion and acts as an effective metal surface. In fact, the surface screens the electric field of distant ions with a negative screening radius. The simulation results serve to confirm existing non-mean-field theories.

Contents

List of Tables

List of Figures

Chapter 1

Introduction

1.1 Historical perspective

Upon heating table salt (NaCl) to over 800°C the coulomb attraction between oppositely charged ions, Na^+ and Cl^-, is overcome by the thermal energy and the once solid crystal melts into a molten salt. Unlike aqueous electrolytes, molten salts do not contain solvent molecules; only ions are present. Molten salts have been extensively studied over the past 200 years. In 1807, Sir Humphry Davy used the electrolysis of a molten salt (KOH) to isolated Potassium (K) for the first time [1]. During WWII, German scientists developed a thermally activated battery that used a molten salt as its electrolyte [2]; this technology was instrumental in the operation of the infamous V-2 rocket, providing electrical power to its guidance system. More recently, and more peacefully, molten salts have been put to use as a medium for storing solar energy as heat [3]. As useful as they are, the potential technological impact of molten salts is limited given the high temperatures needed to keep them in the liquid state.

The high melting temperature of traditional molten salts is a product of the strong coulomb attraction between their small ions with diameter $a \approx 2\mathring{A}$. In 1914 Paul Walden reported the synthesis of a molten salt, ethylammonium nitrate, that has larger ions $a \approx 5\mathring{A}$, and a correspondingly low melting temperature of 12°C [4]; unfortunately it was not stable when exposed to air or water. New synthesis techniques developed in the 1990s [5, 6] gave experimentalists access to a plethora of stable molten salts with the vital properties intact, large ions and low melting temperatures. These new molten

salts are commonly refereed to as room temperature ionic liquids (RTILs) [7]. RTILs had a powerful influence on research; before the year 2000, there were approximately 150 journal articles that contained the phrase, "ionic liquid", while in the last 11 years there have been approximately 9000 [8]. Much of this research was focused on the use of RTILs as green, designer solvents; *green*, because with negligible vapor pressure ($\sim 10^{-5}$ bar), they do not emit volatile organic compounds, and *designer* because today there are thousands of cation-anion combinations from which to choose [9, 7].

Beyond their use as solvents, the new RTILs are ideally suited for any use where a thin or intensely concentrated layer of ionic charge is required. This is due to their maximal electrolyte density. Further, these new RTILs have a larger than normal electrochemical stability window (some do not breakdown until $6V$), and reasonable conductivity ($\sim$ 10 mS/cm) [10]. Applications range from electrochemical capacitors and batteries [10] to gating new electronic materials [11]. In each of these application, rational design advancements hinge on understanding the nature of the interface between a RTIL and a metallic electrode. This region is known as the electric double layer (EDL) of the electrochemical capacitor and can be experimentally probed by measuring its differential capacitance, $C(V) = dQ/dV$.

In a conventional double-plate capacitor, where metal electrodes of area S are separated by an insulator of width d and dielectric constant ε, the capacitance[1] is given by, $C = \varepsilon S/4\pi d$. In an electrochemical capacitor, depicted in Fig. 1.1, the intervening medium is actually a conductor (i.e., an electrolyte) with finite resistivity ρ; however, both ionic and electronic currents are blocked at the electrode-electrolyte interface. Applying a voltage V across the electrodes produces an electric field that polarizes the electrolyte, driving cations and anions toward opposite electrodes. Due to the blocking nature of the electrodes, ions pile up at the electrodes forming an electric double-layer (EDL). For simplicity we first assume that the cations and anions of the electrolyte have the same diameter a, and magnitude of charge e (the elementary charge). Additionally, while an electrochemical capacitor has two EDLs in series (see Fig. 1.1), one at each electrode, we will concentrate on just one EDL, with voltage measured relative to the distant bulk of the electrolyte.

Despite the potential applications, and the simplicity of the system, experimental

[1] Gaussian units will be used through out this thesis unless otherwise specified

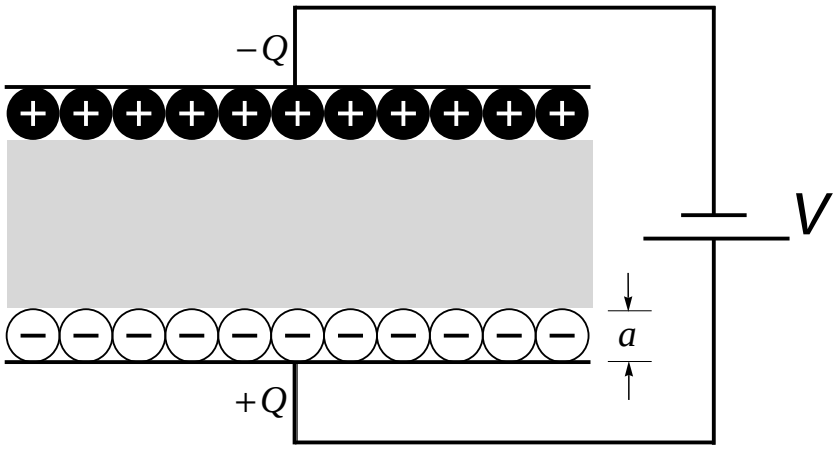

Figure 1.1: Schematic view of an electrochemical capacitor with applied voltage V, electrode charge $|Q|$, and ion diameter a; the ions' scale is exaggerated for clarity. A full layer of ions is condensed on each electrode forming a thin electric double layer (EDL) with maximal capacitance, C_H, the Helmholtz capacitance. The total capacitance of the system is given by the two EDL capacitors in series, $C = C_H/2$. The gray area represents the neutral bulk of the electrolyte

measurements of the capacitance as a function of voltage, C(V), have only recently become available for the electrode/RTIL interface [10]. An analytic prediction for the C(V) curve was also conspicuously absent [12]. The Gouy-Chapman-Stern (GCS) theory [13, 14, 15], which was derived for *dilute* electrolytes nearly a century earlier, was used to predict the capacitance at the electrode/RTIL interface.

The GCS theory is based on a solution to the nonlinear Poisson-Boltzmann (PB) equation. As a mean field theory, PB theory operates in the limit when $e \to 0$, i.e., the discreetness of charge is eliminated. It is instructive to examine both the high and low voltage limits of this curve. At low voltages, $eV \ll k_B T$, the linear expansion of the GCS capacitance gives a transparent result, $C_{GCS} \approx \varepsilon S/r_{DH}$, where

$$r_{DH} = \sqrt{\frac{\varepsilon k_B T}{4\pi e^2 N}} \tag{1.1}$$

is known as the Debye-Hückel screening length of the electrolyte. Here N is the very small concentration of ionized (separated) anions and cations of the electrolyte, T is the temperature, and k_B is the Boltzmann constant. At small voltages, the average distance at which the neutralizing charge resides is r_{DH}. When $eV \ll k_B T$, r_{DH} is large and

the capacitance is very small. In the opposite limit, $V \gg k_B T$, all of the neutralizing charge collapses into a single, uniform, layer forming a very thin capacitor of width $a/2$, the radius of the electrolyte ions. The resulting capacitance,

$$C_H = \frac{\varepsilon S}{2\pi a}, \tag{1.2}$$

is known as the "Helmholtz capacitance". In 1853, Helmholtz envisioned this to be the maximal capacitance for the EDL [16, 17].

Although useful for dilute electrolytes, applying the mean-field GCS theory to ion-dense RTILs is enough to make even the most cavalier theorist sweat. Without a more appropriate theory, progress in understanding the capacitance of the electrode/RTIL interface was difficult. In 2007, Kornyshev reignited the field by publishing a new analytical formula for the $C(V)$ curve of the electrode/RTIL electric double layer [12]. While still mean-field in nature (i.e., lateral ion correlations are not considered), this new theory accounts for the finite size of the RTIL ions. In contrast to the GCS theory, Kornyshev's new theory predicts that the capacitance has a maximum at zero voltage. At non-zero voltages the surface becomes crowded and new ions must reside further away from the electrode; as a result, capacitance decreases with increasing voltage. Even though the shape of the $C(V)$ curve is different from GCS, the maximum capacitance is not; this theory reiterates that for all voltages, $C(V) \leq C_H$.

In this thesis I report on a new theoretical approach aimed at understanding the capacitance of the electrode/RTIL double layer. Based on classical electrostatics, this new theory goes beyond mean-field approximations by carefully considering the role of electrostatic image charges that are formed in the metallic electrodes. The theory qualitatively reproduces key features of both experiment and simulation, and unambiguously claims that image charges, not crowding, are primarily responsible for creating a capacitance maximum around zero voltage. Moreover, this capacitance peak is shown to be several times larger than C_H, as shown in Fig. 1.1. This important result is only possible because the new theory abandons mean-field approximations and considers correlations among ions and image charges, as well as lateral correlations between similarly charged ions near the electrode.

1.2 Main results

Every major theoretical and computational result reported in this thesis is the product of treating the electrode as a conductor. In both theory and simulation, the role of the electrode is possible to distill because of the simplicity of the model employed to describe the electrode/RTIL interface: an infinite, planar, metallic electrode is placed in contact with a semi-infinite volume that contains a total concentration N of mobile positively and negatively charged hard spheres, each with the same diameter a and the same absolute value of charge e. Such a model of the RTIL is called the restricted primitive model. The metallic nature of the electrode implies that every ion in the RTIL has an electrostatic image charge created in the electrode. For brevity they will be referred to as image charges, whose origin is described next.

When a charge q is placed a distance $x' > 0$ away from a grounded conducting plane at $x = 0$, the electric potential in the region $x' > 0$ is given by

$$\phi(x, y, z) = \frac{q}{\sqrt{((x - x')^2 + y^2 + z^2)}} - \frac{q}{\sqrt{((x + x')^2 + y^2 + z^2)}}. \tag{1.3}$$

where the second term can be said to be the result of an image charge, $-q$ at $x = -x'$. This phenomenon is completely incompatible with a mean field theory as individual ions are attracted to their own, discreetly charged image. The energy of this interaction is given by,

$$U_{im}(x') = -\frac{q^2}{4\varepsilon x'}, \tag{1.4}$$

which is half of the interaction energy of two real ions separated by $2x'$. When the ion is touching the electrode, $x' = a$, the interaction energy is maximal and is referred to as $u_{im} \equiv U_{im}(a)$. For $u_{im} \gg k_B T$ an ion may become strongly bound to the metallic electrode resulting in an increased concentration of ions near the electrode, even with zero applied voltage. This is clearly at odds with the results of mean-field theories, along the lines of Gouy-Chapman-Stern, in which the concentration of ions is homogeneous at $V = 0$. The reason for this incompatibility is that the image attraction is beyond the mean-field paradigm where each ion is subjected to the average, (x, y) independent, potential of all other ions. On the other hand, the potential responsible for u_{im} depends on the position of an individual ion only.

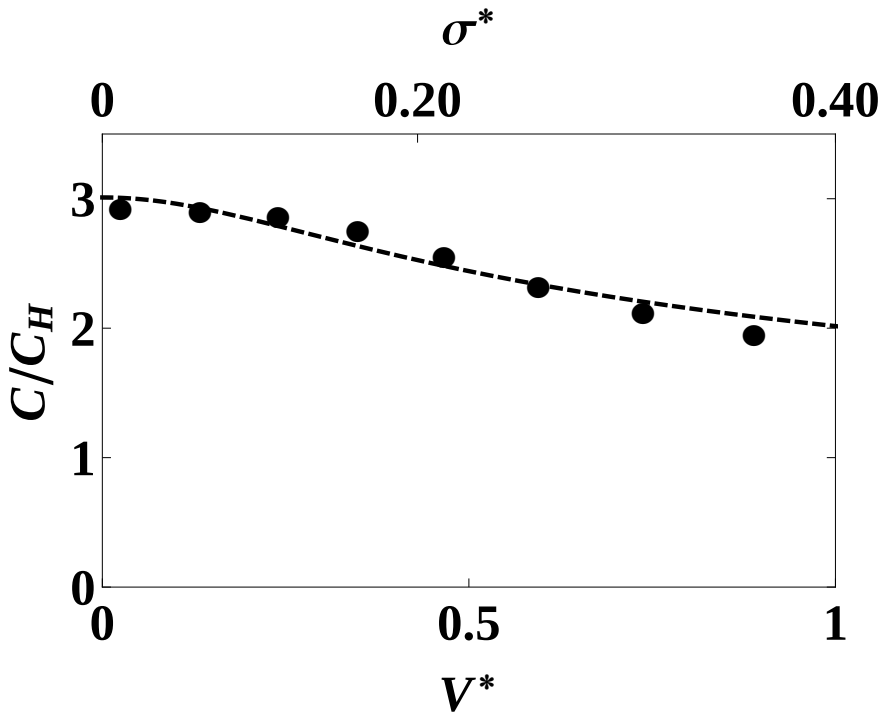

Figure 1.2: The capacitance as a function of the dimensionless voltage $V^* = V/(e/\varepsilon a)$ at $T* = Tk_B a\varepsilon/e^2 = 0.042$ for a system with ion density $Na^3 = 0.4$. The upper axis shows the dimensionless charge density $\sigma^* = Qa^2/\varepsilon Se$, which is equal to 1 when the first layer is completely filled with excess ions. Using typical values for a RTIL, $a = 10\mathring{A}$ and $\varepsilon = 2$ the maximum voltage is this figure is $V \approx 0.75V$, $T \approx 350K$ and the maximum capacitance is $C \approx 11\mu F/cm^2$. The theoretical result from Sec. 2.4 is presented by the dashed line.

Noting the apparent importance of the ion-image interaction, Chapter 2 explores the effect of including image charges in the Monte Carlo (MC) simulation of the electrode/RTIL interface; the effect is profound. In Fig. 1.2, the capacitance as a function of $V* \equiv V/(e/a)$ achieves a maximum nearly three times larger than the expected limit, C_H. Moreover, as indicated on the top axis, the dimensionless charge density $\sigma^* = Qa^2/Se < 1$, which implies that excessive ions on the surface are not densely packed. Incredibly, the system has achieved $C > C_H$ for an electric double layer in which excess ions are sparse rather than densely packed as in the Helmholtz capacitor. This is truly a non-mean-field effect.

These results are interpreted through an analytical, semi-quantitative theory that operates in the limited temperature range where ions may tightly bind to their images, $u_{im} \gg k_B T$, but are still not frozen in the bulk. At zero applied voltage, equal numbers of positive and negative ions are bound to the metal surface. This is possible because the energy of an ion binding to its image charge, $-e^2/2a$, is exactly half the energy of a bound ion pair, $-e^2/a$; therefore, if a bound pair in the bulk is separated and each ion is brought to the surface, there is no net change in electrostatic energy.

As the voltage of the electrode is increased from zero, some number of pairs in the system are separated so that free counterions can move to neutralize the electrode surface. Naturally, the excessive ions that are condensed on the metal surface will repel each other. As depicted in Fig. 1.3, these excess charges form compact ion-image dipoles with dipole moment ea. As a result, excess ions repel each other via the dipole-dipole interaction. In the low temperature limit, these dipoles are strongly correlated and resemble a two-dimensional Wigner crystal.

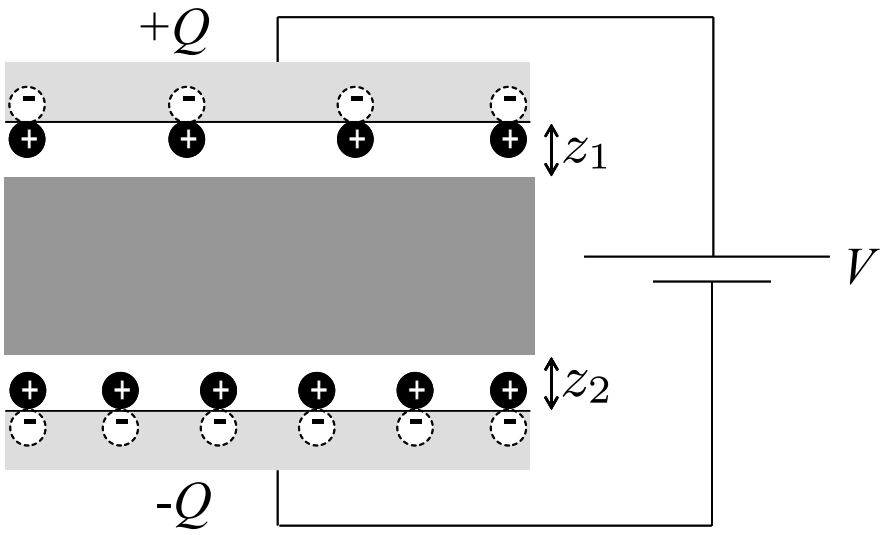

Figure 1.3: A capacitor consisting of parallel metal plates (lightly shaded) bounding an ionic conductor with mobile positive ions. The neutral region of the ionic conductor is heavily shaded, while negative depletion regions (z_1 and z_2) are left white. The relative size of the ions has been greatly exaggerated.

A low temperature theory (see Fig. 1.2) for capacitance, $C(V) \propto C_H/V^{1/3}$, is derived by minimizing the system's energy (the repulsive dipole energy and the work done by

the voltage source) with respect to the number of ions at the surface. To address the divergence at zero voltage, entropic effects are considered that serve to truncate the capacitance at the point when the thermal energy, k_BT is approximately equal to the dipole repulsion energy, thus the bell shape seen in Fig. 1.2. Chapter 2 concludes that the large capacitance around zero voltage is possible for two reasons: (1) an ion pair in the bulk has the same electrostatic energy as two ions bound to the surface; (2) at small voltages, excessive ion dipoles are sparse and repel each other weakly. Near $V = 0$, this makes it possible for a very small change in voltage to attract many counterions. At larger voltages excessive counterions become more tightly packed, until they comprise the first full layer of ions, at which point Kornyshev's theory takes over.

In addition to the bell shaped $C(V)$ curve, experiments have also observed camel shaped $C(V)$ curves, where the capacitance grows parabolically near $V = 0$, reaches a maximum, and then falls again at larger V. This type of curve has been observed when using electrodes made from the semi-metals, graphite and glassy carbon [18, 19, 20]. Chapter 2 briefly addresses this possibility by considering the effects of a poorly conducting electrode, where the screening radius b is larger than the ion diameter a. While still in the limit of linear screening, this type of electrode can be simulated by shifting the position of the image plane deeper into the electrode. This shift, breaks the energetic symmetry between pairs and bound ions; there is now a cost associated with breaking a pair and binding to the electrode. This means that until some threshold voltage is applied to the system, which can over come the energy asymmetry, ions will not condense for free onto the surface and the capacitance will be small. When the threshold voltage is reached, the capacitance peaks and then falls again as it did with an ideally conducting electrode.

Chapter 3 begins by exploring the role of cation/anion size asymmetries in MC simulations of the electrode/RTIL interface. A system in which cations are twice the size of anions is illustrated in Fig. 1.4. The capacitance of such a system again approaches $3C_H$. When the large ions become so big that their movement is sterically prohibited, the system is reminiscent of an ionic conducting glass, in which small mobile ions move between large immobile ions. Chapter 3 reports a theoretical model for this type of system, and the predicted $C(V)$ curve is in good agreement with recent capacitance

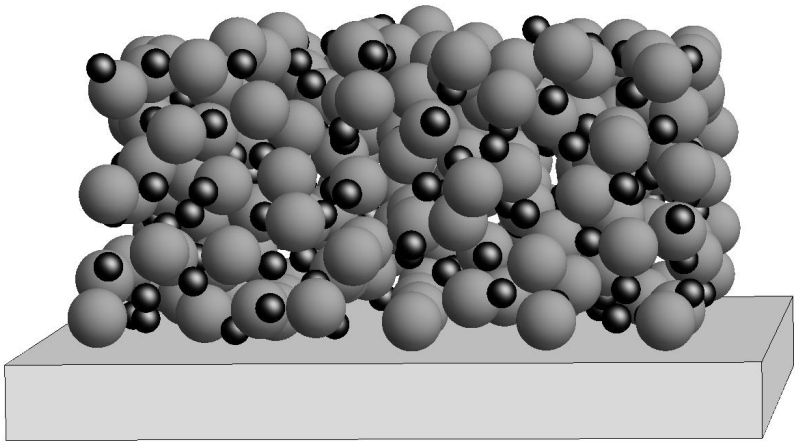

Figure 1.4: A snapshot from the simulation of a primitive model electrolyte in contact with one electrode (bottom) at $V = 0$. Anions are twice as large as the cations in this example. Our theory in Chapter 3 considers the case where the large anions are immobile and form a neutralizing background for the mobile cations.

measurements on ionic conducting glasses (see Fig. 1.5). The theory behind the predicted $C(V)$ curve in Fig. 1.5 is not derived from a primitive model of the ionic glass, but rather a one component plasma model of the system. In this model, the charge of the large immobile ions is considered to be smeared into a continuous background of negative charge through which small mobile positive ions move.

At zero applied voltage, mobile ions are drawn to the surface of the electrode by the image attraction, $u_{im} \gg k_B T$, forming stable ion-image dipoles. These dipoles once again form a strongly correlated liquid. Because only positive ions are mobile, both electrodes possess condensed cations at $V = 0$. Adjacent to each electrode, a negatively charge depletion layer is left behind by the vacating cations (see Fig. 1.3). Upon applying a voltage across the electrodes, charge can easily be moved from one plate to the other because the only resistance to the build up of charge is the weak dipole-dipole repulsion. A a result of this low energy process for moving charge, the capacitance observed in Fig. 1.5 is initially very large. However, when one plate becomes depleted, the energy cost of adding an ion may still be low, but the cost of obtaining that charge has become huge; an ion must be taken from the neutral bulk, leading to a larger depletion layer. This causes the sudden drop in capacitance of the theoretical curve in Fig. 1.5.

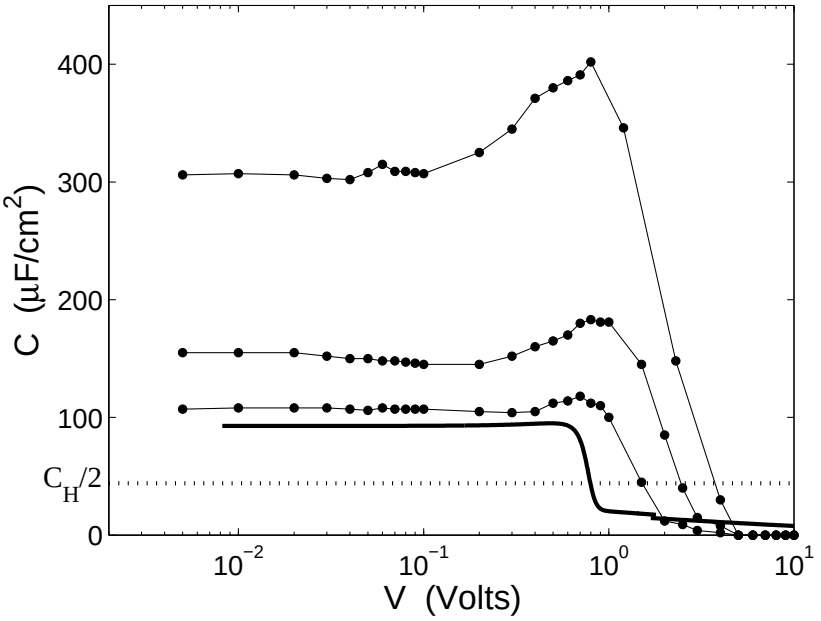

Figure 1.5: The capacitance of a sodium (Na^+) ion-conducting glass between metal plates. The thin lines with dots show data from Ref. [21] from three different samples. The heavy solid line is our theoretical prediction, using $Na^3 = 0.1$, $a = 2$ Å, where a is the diameter of Na^+. The dotted line shows the corresponding Helmholtz value $C_H/2$.

In Chapter 4, the central idea of the image charge is again used, however the focus is not on the capacitance of the EDL of RTILs. Instead, the system in mind is a large, highly charged, insulating macroion that is screened by a dilute aqueous electrolyte composed of much smaller but still multivalent counterions, each with a large charge Ze (for brevity they are called Z-ions). This chapter demonstrates that even though there is no electronic conductor, the concept of an image charge is still essential for understanding the distribution of counterions around the macroion.

When the Z-ions condense onto the macro-ion's surface they repel each other strongly due to their large charge, forming a strongly correlated liquid reminding of a Wigner crystal. This charged liquid, however, can slide along the macro-ion's surface forming a conducting layer. To correctly predict the concentration of stray Z-ions, at distances larger than the average separation of surface Z-ions, image charges, formed in the correlated liquid, must be taken into account.

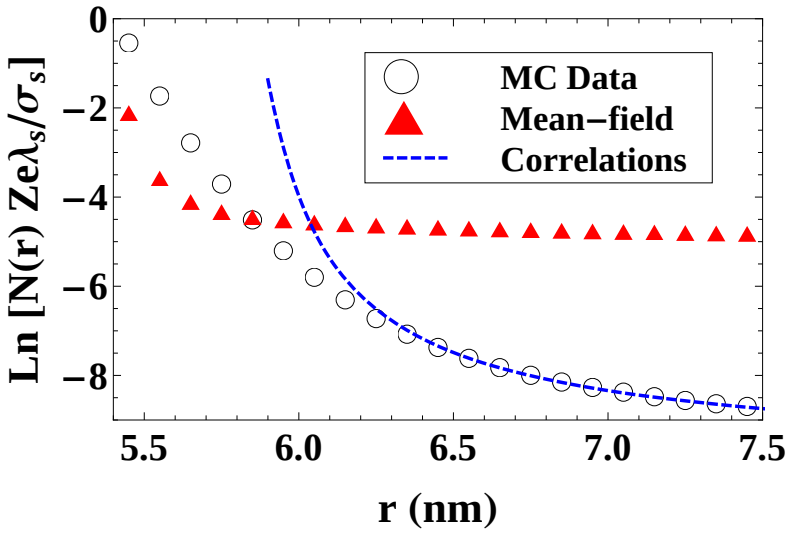

Figure 1.6: The dimensionless concentration of counterions as a function of distance from the macroion as obtained from a Monte Carlo simulation (open circles) and calculated from a theory that includes ion-ion and ion-image correlations (blue dashes). The empirical mean field theory (red triangles), described in the text, fails to predict the MC results because it ignores correlations.

This can be understood as follows. As a stray Z-ion from the bulk approaches the surface of the macroion, it repels adsorbed Z-ions and creates an area of the macroion that is deficient in adsorbed Z-ions. The area of depletion has net charge $-Ze$ and a radius that goes as x', the distance from the stay Z-ion to the macroion surface. An approaching Z-ion experiences an attractive potential created by the depletion area it produced for its self. In this way, one is led to think of the condensed liquid of Z-ions on the surface of the macro-ion as a metallic surface in which a stray Z-ion is attracted to its negative image charge.

Shklovskii [22] predicted that the distribution of Z-ions was significantly influenced by the image interaction, however this was never tested. This task is undertaken in Chapter 4 where a Monte Carlo simulation is employed to measure $N(r)$, the Z-ion concentration as a function of distance from a large, spherical, macroion with surface

charge density, $\sim \sigma_s$. Fig. 1.6[2] shows the MC simulation results for the dimensionless concentration of Z-ions (open circles), along with Shklovskii's theoretical prediction (short blue dashes), and an empirical mean-field prediction (red triangles). The empirical mean-field prediction is the result one would expect, if the Z-ions were Boltzmann distribute according to the spherically symmetric potential derived from the radial Z-ion distribution $N(r)$ (obtained from the MC simulation). Because the empirical mean-field approach does not take correlations into account the radial distribution of Z-ions that it predicts is at odds with the MC results used to derive it.

[2] λ_S is the Gouy-Chapman length, which characterizes the distance a lone Z-ion can move away from the charged macroion when given energy k_BT

Chapter 2

Simulation of the RTIL/electrode interface

Recent experimental studies have measured the capacitance of various room temperature ionic liquids (RTILs) in an electrochemical capacitor [23, 18, 24, 25, 20]. Despite the wide variety of electrode materials and the different properties (e.g., polarizability, size, shape, density) of the RTILs, the $C(V)$ curves always have one of two shapes. The "bell shaped" curve has one maximum near $V = 0$, while the "camel shaped" curve has two maxima, with a minimum near $V = 0$. Current mean-field theories predict that these two cases are the result of ions overcrowding the electrode surface in either a largely incompressible RTIL ("bell shaped") or a highly compressible RTIL ("camel shaped"). Unfortunately, it is difficult to experimentally probe the ionic structure of the EDL at present.

Computer simulations have the ability to report both the capacitance and structure of the RTIL/electrode interface, and have therefore become a popular tool in the research of electrochemical capacitors. A computer simulation is, however, only helpful when the model system resembles the real system of interest. Many simulations of the RTIL/electrode interface model the electrode as a uniformly charged insulator [26, 27, 28, 29, 30, 31], while in most experiments the electrode is metallic . In this chapter the metallic nature of the electrode is shown to be vital in both simulation and theory.

This chapter is based on the work reported in [32].

2.1 How does a RTIL behave near a metallic electrode?

In its simplest form, the question of how a RTIL behaves in the vicinity of a charged metal surface seems remarkably straightforward. While real-life experiments probing the structure of the ionic double-layer can be marked by a number of complications [33], the essential description is encapsulated in a very simple model: an infinite, planar, metallic electrode is placed in contact with a semi-infinite volume that contains a total concentration N of mobile positively- and negatively-charged hard spheres, each with the same diameter a and the same absolute value of charge e. Such a model of the RTIL is called the "restricted primitive model" (RPM); one can think that it reflects the properties of a real RTIL reasonably well because typical ion sizes in a RTIL, $a \sim 1$ nm, are much larger than atomic sizes. The dielectric constant of the RTIL is set equal to unity, since we are considering a model of non-polarizable ions in a solvent-free environment. If a voltage V is applied between the electrode and the bulk of the RTIL, how large is the charge density σ of the metal surface? In other words, what is the capacitance per unit area $C(V) = d\sigma/dV$ of the interface?

Surprisingly, despite the great simplicity of the problem statement, and despite a large number of practical applications for energy storage devices [10], the answer to this question is unknown except in certain extreme limiting cases. The answer to this question is well-known in the limit of large temperature and low applied voltage. In this case the ionic double-layer is well-described as a diffuse screening layer with a characteristic size equal to the Debye-Hückel (DH) screening radius

$$r_{DH} = \sqrt{\frac{k_B T}{4\pi e^2 N}}. \tag{2.1}$$

Here, $k_B T$ is the thermal energy. The diffuse layer of counter-charge effectively comprises the second half of a parallel-plate capacitor of thickness r_{DH}, so that the capacitance per unit area is equal to $C_{DH} = 1/4\pi r_{DH}$. At large density $Na^3 \sim 1$ this result for capacitance is valid as long as the temperature is high enough that $T \gg T_0 \equiv e^2/k_B a$ and the voltage is small enough that $eV \ll k_B T$.

More generally, one can characterize the capacitance by the effective thickness of the

double-layer $d^* = 1/4\pi C$. In the DH limit, $d^* = r_{DH}$. In realistic situations, however, the characteristic temperature T_0 is very large and the DH approximation fails at room temperature. One can think that as a result ions become more strongly bound to the charged electrode and the size of the double-layer shrinks, so that d^* decreases and the capacitance grows. One may ask, then, how thin the double-layer can be, or in other words, how large the capacitance can be?

As explained in Sec. 1.1, the apparent answer to this question goes back to Helmholtz [16], who imagined that in an extreme case a neutralizing layer of ions could collapse completely onto the electrode surface, thereby forming the second half of a plane capacitor at a distance equal to the ion radius $a/2$. The result is a double-layer of size $d^* = a/2$ and a capacitance per unit area equal to the "Helmholtz capacitance"

$$C_H = 1/2\pi a. \tag{2.2}$$

In classical mean-field theories of the electrostatic double-layer [13, 14, 15], and in the recent influential theory of the metal/RTIL capacitance which accounts for the excluded volume among ions [12], C_H plays the role of a maximum possible capacitance per unit area. Monte Carlo simulations [34, 35, 27] seem to confirm this statement. However, these and the majority of other simulations make the simplification of replacing the metal electrode by a uniformly-charged, insulating plane. It is argued below that in this way the essential physics of image charges in the metal surface is lost (see also Refs. [36, 37, 38]).

It is the purpose of this chapter to demonstrate that capacitance $C > C_H$ is possible, or in other words, that the effective thickness of the double-layer can be smaller than the ion radius. As described below, the metallic nature of the electrode — specifically, the ability of ions to form image charges in the metal surface — plays a key role in the development of large capacitance. Additionally, the two general $C(V)$ curve shapes (i.e., "bell" and "camel") are qualitatively reproduced in our simulations without the electrode surface becoming overcrowded by excess ions.

Notably, the critical role of the image charges for the structure of the double-layer has in fact been recognized by previous authors. Torrie [39] developed the first MC simulation of the restricted primitive model that included image charges; however, because of the high temperatures and low concentrations of the simulation, only a slight

increase in ion density was observed at the electrode surface and capacitance was not addressed at all. Perhaps due to the middling effects seen, few simulations investigating capacitance over the next three decades included image charges. Alawneh et al. [40] included image charges, but again explored only very low ion density $Na^3 = 0.01$, where $C(V = 0) < C_H$. Another paper [41] studied the capacitance of a RTIL between two identical metal plates and obtained large capacitance $C(0) \sim 2C_H$, but this study used a much more complicated model of the RTIL.

Theoretical work has also addressed the effect of image charges on the capacitance of the electric double layer. Outhwaite and Bhuiyan [42] developed a modified Poisson Boltzmann (MPB) theory of the electric double layer that includes electrode polarization and excluded volume effects. The effect of the images, however, only serve to modify the concentration gradient of ions perpendicular to the electrode as lateral correlations are not included [43]. The MPB theory, therefore, cannot predict a capacitance larger than the Helmholtz capactiance, $C < C_H$. As this Chapter demonstrates $C > C_H$ is only possible when image charges *and* lateral correlations are allowed.

The Monte Carlo (MC) simulation of the restricted primitive model of a RTIL is described in Sec. 2.2. The results of the Monte Carlo (MC) simulations at various temperatures and densities are presented in Sec. 2.3. A basic theoretical explanation of these results based on the weak repulsion between dipoles composed of bound ions and their images in the metal surface is suggested in Sec. 2.4, where our analytical prediction for $C(V, T)$ is presented. Sec. 2.5 considers the role of the electrode material on $C(V, T)$. This chapter closes with Sec. 2.6, a summary of the main results.

2.2 Simulation of the restricted primitive model

The MC simulation described in this chapter contains the same basic structure that will be repeated in Chapters 3 and 4. At the core of each MC simulation is the Metropolis method, which is clearly described in [44]. In this chapter, the most important feature of the simulation is that it reproduces the conducting properties of the electrode. To this end, the success of the simulation depends on having a convenient method for incorporating the electronic response of the electrode to the presence of an ion; this is accomplished through the use of image charges.

2.2.1 Including the electrostatic image charges

When a charge q is placed a distance x' away from a grounded conducting plane at $x = 0$, the free charge of the conductor arranges itself such that the potential is zero both at the surface of the plane and as $x \to \infty$. The electric potential, $\phi(x, y, z)$ in the region $x > 0$, must satisfy both Poisson's equation and these boundary condition. Proper placement of an image charge $-q$ at $x = -x'$, opposite the original charge, leads to such a solution,

$$\phi(x, y, z) = \frac{q}{\sqrt{((x - x')^2 + y^2 + z^2)}} - \frac{q}{\sqrt{((x + x')^2 + y^2 + z^2)}}. \tag{2.3}$$

where the second term can be attributed to the image charge. This simplification provides an efficient method for incorporating the conducting nature of the electrode into our simulation. Calculating the electrostatic energy of the system is simply a matter of knowing the charge and position of each ion and its image charge, with one caveat. If all of the charges were real (i.e. the image charges were replace by real ions), the system's electric field would permeate all of space, however, due to the metallic electrode, half of the charges are just images and the electric field is restricted to half of space leading to a reduced electrostatic energy, $U_{real\ ions} = 1/8\pi \iiint E^2 dV = 2U_{ions\ \&\ images}$.

2.2.2 Monte Carlo simulation method

In our MC simulations, a canonical ensemble of M_a anions and M_c cations is placed in a square prism cell of dimensions $L \times L \times L/2$ and corresponding volume $\Omega = L^3/2$. The metallic electrode coincides with one of the cell's square faces. Every charge within the cell forms an electrostatic image in the electrode surface ($z = 0$), *i.e.* a charge $q = \pm e$ at position (x, y, z) has an image charge $-q$ located at $(x, y, -z)$. The total electrostatic energy $\mathcal{E}$ of the cell is calculated as $1/2$ times the energy of a system twice as large composed of the real charges and their images, so that

$$\mathcal{E} = \frac{1}{2} \sum_{\{i,j\}}^{M_t} u(d_{i,j}), \tag{2.4}$$

where the indices i, j label the set of all particles in the system (ions and images), $M_t = 2(M_a + M_c)$ is the total number of these particles, $d_{i,j}$ is the distance between

particles i and j, and the two-particle interaction energy $u(d_{i,j})$ is

$$u(d_{i,j}) = \begin{cases} \infty, & d_{i,j} < a \\ q_i q_j / d_{ij}, & d_{i,j} > a \end{cases}. \tag{2.5}$$

Here, $q_i = \pm e$ is the charge of particle i.

The charge of the electrode is varied by changing the number of anions M_a and cations M_c in the system by equal and opposite amounts, so that the total number of ions $M_a + M_c = N\Omega$ remains fixed for a given overall density N. The corresponding electronic charge (in the form of image charges) in the electrode is $Q = e(M_a - M_c)$ and the capacitance dQ/dV can be determined from the resulting voltage. The system size $L = 20a$ is used everywhere.

At the beginning of each simulation, positive and negative ions are placed within the simulation cell in such a way that they do not overlap with each other or with the metal surface. The MC program then selects an ion at random and attempts to reposition it to a random position within a cubic volume of $(2a)^3$ centered on the ion's current position. The change in the energy $\mathcal{E}$ associated with this move is then calculated, and the move is accepted or rejected based on the standard Metropolis algorithm. For one in every 100 attempted moves, the MC program chooses the random position from within a larger volume $(10a)^3$ as a means of overcoming the effects of any large, local energy barriers. The simulation cell is given periodic boundaries, so that an ion exiting one face of the cell re-enters at the opposite face. To ensure thermalization, 2,500 moves per ion are attempted before any simulation data is collected. After thermalization, simulations attempt 2×10^4 moves per ion, of which 15% – 50% are accepted.

The voltage of the electrode is measured by defining a "measurement volume" near the back of the simulation cell — occupying the range $-L/4 < x < L/4$, $-L/4 < y < L/4$, $L/4 < z < 3L/8$, where the origin $(x, y, z) = (0, 0, 0)$ is located at the center of the electrode surface — inside of which the electric potential is measured. After performing thermalization, the total electric potential is measured at 500 equally-spaced points within the measurement volume after every $3(M_a + M_c)$ attempted moves. These measured values of potential are then averaged both temporally and spatially to produce a value for the voltage V of the electrode relative to the bulk. There was no noticeable

systematic variation in electric potential across the measurement volume. The capacitance $C(V = 0)$ is determined from the discrete derivative $\Delta Q/\Delta V$ at sufficiently small values of Q that the relationship Q vs. V is linear.

Our results are shown in Fig. 2.1. For all Na^3 studied, the lowest value of T^* in Fig. 2.1 is larger than the corresponding liquid-gas or liquid-solid coexistence temperature. For comparison, the triple point in the phase diagram of the RPM ionic liquid is located at $Na^3 = 0.5$ and $T^* = 0.025$ while the gas-liquid critical point is at $Na^3 = 0.02$ and $T^* = 0.05$ [45]. For each simulation, it was verified that there was no phase separation within the simulation cell.

In order to quantify the finite-size effects of our simulation cell, we examined the capacitance at zero voltage, $C(0, T^*)$, obtained from three simulation volumes of size $L = 10a$, $20a$, and $30a$. For $Na^3 = 0.4$, $C(0, T^*)$ was seen to scale linearly with $1/L$ at all values of the temperature that we examined ($T^* = 0.042$, 0.072, and 0.14). In each case, the value of $C(0, T^*)$ obtained by extrapolation to infinite system size was within 20% of the value of $C(0, T^*)$ corresponding to $L = 20a$. These results allow us to conclude that the simulation cell with $L = 20a$ provides a reasonable approximation of an infinite system. All MC results presented below correspond to this choice.

2.3 Temperature dependence of capacitance observed in simulation

Figure 2.1 shows the zero voltage capacitance $C(0)/C_H$, as measured by our MC simulations, as a function of reduced temperature $T^* = T/T_0$ for three different dimensionless ion densities Na^3. The points correspond to results from the MC simulation and solid lines are a fit to the form $C/C_H = A \cdot (T^*)^{-1/3}$, where A is a numerical constant. The motivation for this $(T^*)^{-1/3}$ dependence is explained in Sec. 2.4. For all three values of the density that are examined, the capacitance at low temperature is significantly higher than the Helmholtz value.

These results should be contrasted with previous simulation studies [34, 35] of the capacitance of the RPM, in which the metallic electrode was replaced by a charged insulator with uniform charge density σ. These studies report a capacitance $C(V = 0, T)$ that grows with decreasing T^* before reaching a peak at $T^* = T_p^*$ and then collapsing

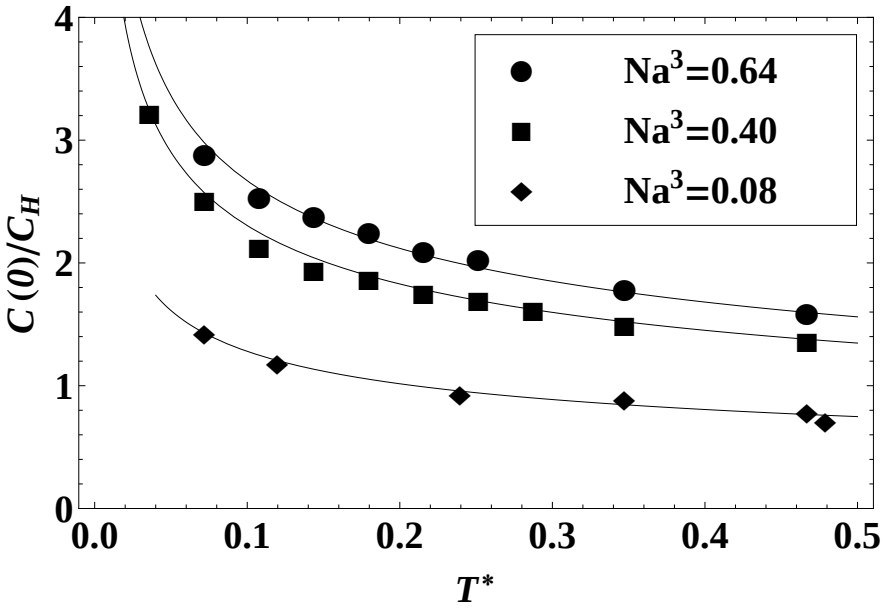

Figure 2.1: The capacitance of the metal/RTIL double-layer at zero voltage as a function of the dimensionless temperature T^*, plotted for three values of the dimensionless ion density Na^3. Symbols represent results from the MC simulation and solid lines show a best fit to the form $C/C_H = A \cdot (T^*)^{-1/3}$ for each density. Error bars are smaller than the symbol size.

rapidly at $T^* < T_p^*$. For $Na^3 = 0.08$ and 0.64, $T_p^* \approx 0.17$ and 0.28, respectively.

The collapse of the capacitance at low temperatures $T^* < T_p^*$ was interpreted by the authors of Refs. [34, 35] as the result of strong binding of positive and negative ions to form neutral pairs. Such binding leads to an extreme sparsity of free charges in the RTIL, so that their total concentration $N_f \ll N$. Substituting N_f for N into Eq. (2.1) at $T^* \ll 1$, we arrive at a large screening radius r_{DH} and therefore much smaller capacitance $C(0)$. These arguments are generic and convincing. Why, then, does the capacitance in Fig. 2.1 continue to grow with decreasing temperature?

2.4 Interpreting the capacitance growth at small voltage and temperature

Our goal is to interpret the large capacitance of the metal/RTIL interface at $T^* \ll 1$. In this section we suggest an analytical, semi-quantitative theory of a mechanism which produces such large capacitance. This theory operates in the limited range of temperature $0.05 < T^* < 1$, where the RTIL does not freeze. Thus, our theory (as any theory of the liquid state) does not have any true asymptotically small parameters and should be considered only semi-quantitative.

We begin by observing that when the electrode is metallic, the energy of an ion binding to its image charge, $-e^2/2a$, is exactly half the energy of a bound ion pair, $-e^2/a$. This fact implies that if an ion pair is separated in the bulk and then both ions are brought to the metal surface there is no net change in electrostatic energy. Thus, even in the absence of applied voltage there are plenty of free charges at the metallic surface. Roughly speaking, this allows the double-layer to be very thin and leads to the large capacitance shown in Fig. 2.1.

The zero-energy process of ion pairs dissociating and sticking to their images on the metal surface implies that at low temperatures $T^* \ll 1$ effectively all ions in the system are either paired in the bulk or bound to their images on the electrode. This statement is correct even in a relatively dense liquid, where a significant fraction of ion pairs in the bulk form larger neutral clusters, and ions sticking to the metal may be decorated by one or more neutral pairs. Let us imagine a bulk cluster made of $2m$ ions, where m is an odd number — for example, $m = 3$. If the cluster is sufficiently symmetric, then it can be dissociated into two smaller clusters, one positive and one negative, which have an equal number m of ions and which differ only by the inversion of the charge of each ion. When these two charged clusters stick to their images in the metal surface they also recover the energy spent on their dissociation. Thus we are dealing with a statistical physics problem of very high degeneracy, which may have a beautiful exact solution. (Less symmetric clusters may have a small contribution to the partition function of the system.) In this Chapter the term "excess ions" will be used to refer to all charged objects at the surface, regardless of whether they are decorated by neutral pairs.

At zero applied voltage, equal numbers of positive and negative ions are bound to the

metal surface. The area density n_0 of these ions can be estimated from the requirement that the chemical potential of pairs in the bulk be equal to the chemical potential of ions at the surface, which gives $\ln(2/Na^3) \simeq 2\ln(1/n_0a^2)$, so that $n_0 \simeq \sqrt{N/2a}$.

As the voltage V of the electrode is increased from zero, some number of pairs in the system are separated so that the free counterion can come to neutralize the electrode surface. The corresponding density of these "excess ions" δn on the metal surface is related to the charge density σ by $\delta n = |\sigma|/e$. If $\sigma > 0$, then δn represents an excess of anions on the surface; if $\sigma < 0$ the excess ions are cations. Naturally, excess ions condensed onto the metal surface repel each other. Since each ion on the metal surface is separated by a distance a from its image charge in the metal, ions and their images constitute compact ion-image dipoles with dipole moment ea, and so excess ions repel each other via a dipole-dipole interaction

$$u_{dd}(\delta n) = \frac{e^2a^2(\delta n)^{3/2}}{2}. \tag{2.6}$$

Excess ions at the metal surface are surrounded by n_0 other ions per unit area, which effectively neutralize each other by forming $n_0/2$ bound pairs. These $n_0/2$ bound pairs, along with bound pairs in the bulk, may serve to modify the effective dielectric constant for the interaction of excess ions. We comment on this possibility later in this article.

At low temperatures, the excess ions will seek to maximize their distance from each other while maintaining a given density δn. One can hypothesize a zero-temperature description of the resulting positional correlations, where excess ions form a strongly-correlated liquid reminiscent of a two-dimensional Wigner crystal. The corresponding total electrostatic energy per unit area of the system is

$$U = \alpha \cdot \delta n \cdot u_{dd}(\delta n) - e\delta nV, \tag{2.7}$$

where α is a numerical coefficient which describes the structure of the lattice of excess ions; for a triangular lattice, $\alpha \approx 4.4$ [46]. The term $-e\delta nV$ describes the work done by the voltage source.

The voltage V which corresponds to a given charge density $\sigma = e\delta n$ can be found by the equilibrium condition $\partial U/\partial(e\delta n) = 0$, which gives

$$V = \frac{5\alpha ea^2}{4}(\delta n)^{3/2}. \tag{2.8}$$

The resulting capacitance per unit area $C = d\sigma/dV = e[dV/d(\delta n)]^{-1}$ is

$$C(\delta n) = \frac{8}{15\alpha a\sqrt{\delta n a^2}}. \tag{2.9}$$

Substituting Eq. (2.8) into Eq. (2.9) gives the capacitance in terms of voltage:

$$C(V) = \frac{8}{3}\left(\frac{1}{10\alpha}\right)^{2/3}\left(\frac{e}{aV}\right)^{1/3}\frac{1}{a} \approx 1.3\left(\frac{e}{aV}\right)^{1/3} C_H. \tag{2.10}$$

The expression of Eq. (2.10) implies that C can be significantly larger than C_H when V is small. At such small voltages, the fractional coverage of excess ions on the electrode surface $\delta n a^2 \ll 1$, so that it is incorrect to think of the double-layer in the mean-field way: as a series of uniform layers of charge. Rather, the neutralizing ionic charge consists of discrete ion-image dipoles. The correlated nature [1] of these dipoles allows for lower energy than what is possible in mean-field descriptions, and therefore larger capacitance that is not limited by the physical distance $a/2$ between the electrode and its countercharge.

Of course, the validity of Eqs. (2.6) – (2.10) is limited to the range of voltage where $\delta n a^2 \ll 1$. By Eq. (2.8), this corresponds to a dimensionless voltage $V^* = V/(e/a) \ll 5\alpha/4 \approx 5.5$. At large enough voltages that $\delta n a^2 \simeq 1$, excess ions constitute a uniform layer of charge, and therefore the capacitance approaches C_H. At even larger voltages, the capacitance declines as complete layers of counterions accumulate next to the electrode and the double-layer becomes thicker. This leads to a mean-field capacitance $C \propto V^{-1/2}$ at large voltages, as described in Ref. [12].

Formally, Eq. (2.10) diverges as the voltage goes to zero. Of course, this expression neglects entropic effects of the excess ions, which tend to destroy the lattice structure of excess ions on the metal surface. Such effects will truncate the low-voltage divergence of Eq. (2.10), resulting in a finite capacitance at zero voltage. Intuitively, one would expect that the value of this capacitance maximum can be estimated by evaluating the capacitance at the point where $u_{dd}(\delta n) = k_B T$. This procedure gives

$$C_{max}(T) = \frac{A}{(T^*)^{1/3}} C_H, \tag{2.11}$$

[1] In principle, the correlations among excess ions on the metal surface can be identified from MC data. This process is made difficult, however, by the large number of neutral pairs and larger neutral clusters present on the metal surface at small voltages. A more exhaustive MC investigation of the surface correlations will be the subject of future work.

where $A \approx 0.6$. In other words, the effective thickness $d^* = a(T^*)^{1/3}/2A$. At $T^* \ll 1$, we find that $d^* \ll a$. The corresponding voltage at which the capacitance plateaus (u becomes equal to $k_B T$) is $V_c^* \approx 11T^*$.

Figure 2.2 shows the capacitance as a function of V^*, as measured by our MC simulation, at density $Na^3 = 0.4$ and at two values of the temperature T^*. The inset shows the dimensionless charge density $\sigma^* = \sigma a^2/e$ of the electrode as a function of the voltage V^* for the temperature $T^* = 0.042$. The capacitance is determined by a numerical derivative of the σ vs. V curve. Here, e/a^2 is the maximal density for a square lattice of ions on the metal surface, so that σ^* can be interpreted as a filling factor of the first layer of ions. Note that the capacitance drops substantially even at low filling factor σ^*, so that the capacitance is already reduced by a factor two at $\sigma^* = 0.5$. This suggests that for $V^* \lesssim 2$ the decline in capacitance is not driven by the excluded volume effects emphasized in the theory of Ref. [12].

The conclusion $C_{max}(T) \propto (T^*)^{-1/3}$ can also be reached by an analytical description of the metal surface which is appropriate for small charge density σ, where the excess ions can no longer be described as a strongly-correlated liquid. When the density of excess ions is small enough that $\delta n a^2 \ll (T^*)^{2/3}$, the total free energy F per unit area can instead be written using a virial expansion:

$$F \simeq F_{id} + (\delta n)^2 k_B T B(T) - e\delta n V. \tag{2.12}$$

Here, $F_{id} = \delta n k_B T \ln(\delta n a^2)$ is the free energy of a two-dimensional ideal gas, $B(T)$ is the second virial coefficient, and $-e\delta nV$ is the source work term. $B(T)$ is calculated from the dipole-dipole interaction energy $u_{dd}(r)$ between two ion-image dipoles as

$$B(T) = \frac{1}{2}\int_0^\infty \left(1 - e^{-u_{dd}(r)/k_B T}\right) 2\pi r dr, \tag{2.13}$$

$$\approx 2.65 \left(\frac{e^2 a^2}{k_B T}\right)^{2/3}. \tag{2.14}$$

As before, we can use the equilibrium condition $\partial F/\partial(e\delta n) = 0$ to define the voltage with respect to the density of excess ions δn, which gives

$$V^* \simeq T^* \left[5.3\delta n a^2 (T^*)^{-2/3} - \ln\left(1/\delta n a^2\right)\right]. \tag{2.15}$$

In the limit $V^* \to 0$, the two terms on the right hand side of Eq. (2.15) become equal, and the corresponding capacitance $d(e\delta n)/dV$ is $C_{max}(T) \simeq A \cdot C_H/(T^*)^{1/3}$. Hence,

this approach arrives at the same conclusion as that of Eq. (2.11), although it gives a somewhat different estimate for the constant $A \approx 1.2$.

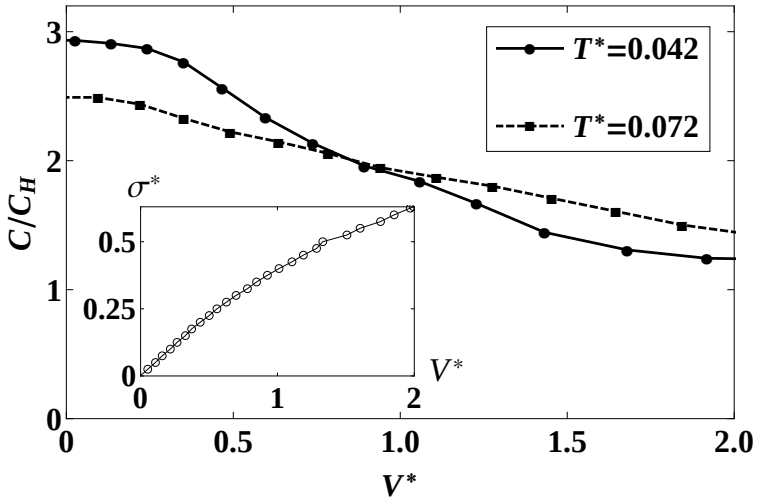

Figure 2.2: The capacitance as a function of the dimensionless voltage $V^* = V/(e/a)$ at two different temperatures for a system with ion density $Na^3 = 0.4$. The inset shows a plot of the dimensionless charge density $\sigma^* = \sigma a^2/e$ as a function of the voltage V^* measured by the MC simulation at the temperature $T^* = 0.042$.

The prediction of Eq. (2.11) provides a good fit to the capacitance measured by our MC simulation over a range of ion densities, as shown in Fig. 2.1. The value of the coefficient A is found to be 0.6, 1.1, and 1.2 for $Na^3 = 0.08$, 0.4, and 0.64, respectively, which is consistent with our earlier estimates. The dependence of the constant A on the ion density, which produces larger capacitance at larger Na^3, is perhaps an indication that the dipole interaction suggested in Eq. (2.6) is weaker at higher ion density. One possible explanation is that at high densities ion pairs in the vicinity of two excess ions can polarize in the direction of the electric field, thereby producing an effective dielectric constant between them. If such a dielectric constant ε' is added to Eq. (2.6), then we find that $A \approx 0.6(\varepsilon')^{2/3}$. The values of the constant A from above suggest that for bulk densities $Na^3 = 0.08, 0.4$, and 0.64, the value of ε' is $1.0, 2.4$, and 2.9, respectively. These values are consistent with our interpretation that the effective dielectric constant should increase with ion density, driving the capacitance upward. This increase is also

reflected in Fig. 2.2, where the capacitance at finite voltage is somewhat larger than predicted by Eq. (2.10), consistent with the increase in the constant A.

Based on our arguments from this section about the dependence of the capacitance on voltage and temperature, we can hypothesize a general scaling relationship $C(V^*, T^*)$ which reproduces Eqs. (2.10) and (2.11):

$$\frac{C(V^*, T^*)}{C_H} = \frac{\beta_1}{[(\beta_2 T^*)^2 + (V^*)^2]^{1/6}}. \tag{2.16}$$

Here, β_1 and β_2 are numerical coefficients. Applying this fit to the curves shown in Fig. 2.2 gives a reasonably good fit with $\beta_2 \approx 8$, suggesting that the capacitance plateaus at about $V^* = 8T^*$, as compared to the theoretically estimated value $V_c^* = 11T^*$.

2.5 Model variations

In this section, the goal is to expand our simulation and theory beyond the restricted primitive model and a perfectly conducting electrode, to better reflect the diversity of electrode material and RTILs used in experiment.

2.5.1 Electrode material: from perfect to poor metal

So far we have assumed that the electrode is a perfect metal, or in other words, that the screening radius b of the metal is much smaller than the ion diameter a. This assumption is justified for RTILs with large ions and electrodes made from a good metal. Experiments on such systems have indeed reported large capacitance that declines with absolute value of voltage [18] (the $C(V)$ curve is "bell-shaped"). However, for smaller ions and for electrodes made from semi-metals, such as graphite or glassy carbon, experimental values of $C(V = 0)$ are smaller and the $C(V)$ curves are "camel-shaped", i.e., the capacitance grows parabolically near $V = 0$ [18, 19, 20].

In order to interpret this difference qualitatively, let us recall that in such poor metals the density of states at the Fermi level is relatively small and the screening radius b of the metal may become comparable to $a/2$. As a result, the image potential changes. When $b < a/2$ one can think that the electric field produced by ions at the metal surface is relatively weak and slowly-varying. In such a case the screening charge of the metal is effectively situated at the distance b away from the metal surface, *i.e.*

at $z = -b$. Therefore, the reflection plane for the image charge is at $z = -b$, so that an ion at distance z from the surface experiences a smaller attraction $-e^2/4(z+b)$ to the surface, rather than the standard $-e^2/4z$ for a perfect metal. At the distance of closest approach $z = a/2$, the ion-to-surface attraction energy becomes $-e^2/2(a+2b)$. This leads to a finite energy cost E_0 for dissociating a bulk ion pair and bringing it to the metal surface, given by $E_0 = e^2/[a^{-1} - (a+2b)^{-1}]^{-1}$. Thus, a finite voltage is necessary to break pairs in the bulk and obtain free ions which can provide screening. This means that, for an electrode with finite screening radius b, the bell-shaped $C(V)$ curve splits into two peaks located at $V = \pm E_0/e$, thereby becoming camel-shaped, in agreement with the above-mentioned data.

The capacitance $C(V)$ at $V > E_0/e$ can be estimated with the help of the theory in Sec. 2.4 leading up to Eq. (2.10). In this case, however, the voltage V in Eq. (2.10) should be replaced by $V - E_0/e$ and the dipole arm a should be replaced by the longer arm $a + 2b$. These substitutions give

$$C(V) = 1.3 \left(\frac{e}{(a+2b)(V - E_0/e)} \right)^{1/3} \frac{a}{a+2b} C_H \tag{2.17}$$

for $V > E_0/e$. Since the dipole-dipole repulsion is much stronger due to the longer dipole arm, $C(V)$ is substantially smaller and reaches its geometrical limit $C_H(b) = C_H \cdot a/(a+2b)$ at a smaller voltage $V - E_0/e = 5\alpha e/4(a+2b)$, or $V^* - E_0/(e^2/a) \approx 5.5/(1+2b/a)$. Starting from this voltage the capacitance saturates at the level of $C_H(b)$.

Only at even larger voltage $V^* - E_0/(e^2/a) \gtrsim [5.5a^2 + 8\pi b(a+b)]/[a(a+2b)]$ do counterions comprise a full layer at the surface, after which the theory of multi-layer arrangement of ions [12] becomes applicable. This same behavior for $C(V)$ is expected in the case where a good metal is covered by a thin insulating layer, for example, its own oxide.

In order to verify this theory we repeated our MC calculations for $T^* = 0.04$ and $Na^3 = 0.5$ using a relatively large $b = a/2$, which is at the limit of applicability for linear screening by the electrode surface. For simplicity, we have also assumed that the metal ion lattice has the same dielectric constant as our RTIL. Results are shown on Fig. 2.3, plotted as a function of V^* and σ^*. As expected, the peak at $V = 0$ is split into a camel-like structure (we show only the positive half of the symmetric C–V curve). The characteristic dimensionless voltage of the peak is $V_p^* \approx 0.5$, in agreement with the

above estimate for E_0. Note that the capacitance maximum occurs at $\sigma^* = 0.1$ and is apparently not related to excluded volume effects among counterions. As predicted by Eq. (2.17), the peak capacitance $C(V_p^*)$ is approximately 2.5 times smaller than at $b = 0$ [recall that $C_H(b)$ in Fig. 2.3 is twice smaller than C_H in Fig. 2.2].

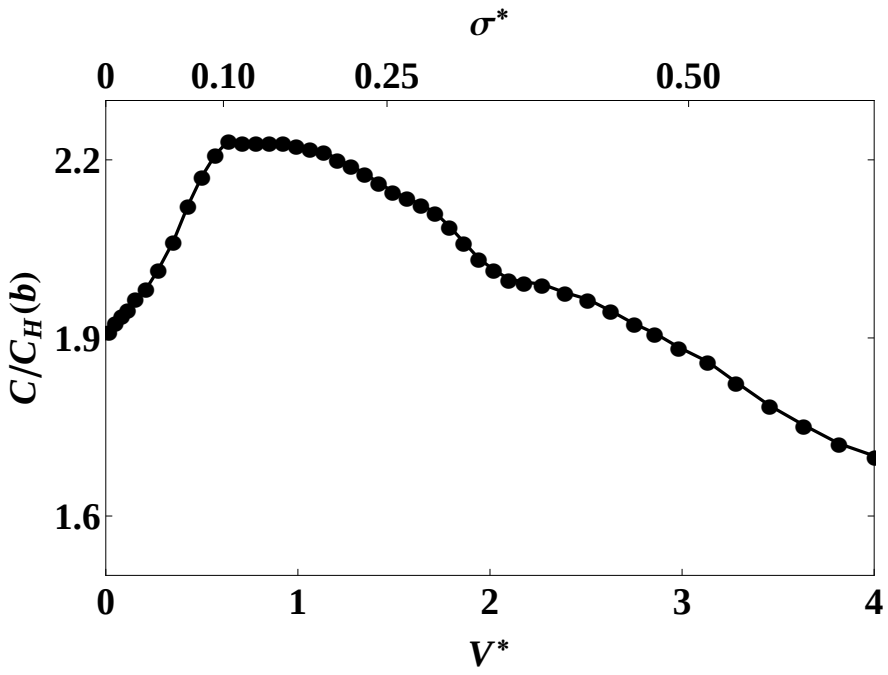

Figure 2.3: The ratio of the capacitance of the metal/RTIL interface C to the geometrical capacitance $C_H(b)$, plotted as a function of dimensionless voltage V^* (bottom axis) and charge density σ^* (top axis) for a system with ion density $Na^3 = 0.4$ and metal screening radius $b = a/2$. The capacitance is determined by a numerical derivative of the σ vs. V data obtained from a MC simulation at temperature $T^* = 0.042$.

2.5.2 Asymmetric ion size

The results of Fig. 2.4 can be compared to those of a recent study [27] which performed a molecular dynamics simulation of an ionic liquid with size ratio $A/a = 2$ near a uniformly charged interface. In this study, the capacitance was found to be similarly asymmetric with voltage, with the larger capacitance resulting when the voltage has the same sign as the larger ion. However, since the study considered only the response of the ionic liquid to a uniformly-charged plane (essentially treating the metal electrode as

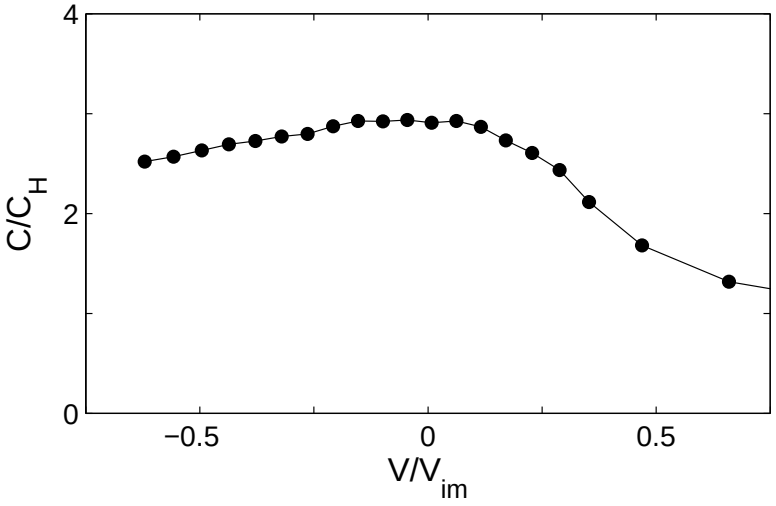

Figure 2.4: The capacitance of a single metal/ionic liquid interface as a function of voltage for an ionic liquid with $A/a = 2$. The temperature is $T^* = 0.036$ and the density is $\rho_b^* = 0.5$. Error bars are smaller than the symbols. .

a charged insulator), it arrived at capacitances $C < C_H$ at all voltages. It is also worth emphasizing that over the range of voltage in Fig. 2.4 we are still far from complete coverage of the electrode surface. Indeed, at $V/V_{im} = 0.5$ the area coverage of the surface is only 35% and 0.2% by anions and cations, respectively, while at $V/V_{im} = -0.5$ it is 3% and 28%. Thus, in our case the collapse in capacitance is not caused by the building of a second layer of ions, as proposed by Ref. [12]. The effects of cation–anion size asymmetry are addressed in more detail in Chapter 3.

2.6 Summary and polarization considerations

To summarize, this chapter is concerned with Monte Carlo simulations of the restricted primitive model of a RTIL at a metal interface. Within this model, we obtain capacitance at zero voltage as large as $3C_H$. We also find that for a good metallic electrode at small voltage, C decreases with T as $T^{-1/3}$. When the temperature is fixed and is relatively small, $C(V)$ decreases as $1/V^{1/3}$ (the C–V curve is "bell-shaped"). On the other hand, when the electrode is made from a semi-metal the C–V curve is "camel-shaped", meaning that the capacitance first grows with V and then goes through a maximum and

decays as $1/V^{1/3}$. We interpret these results with the help of a semi-quantitative analytical theory based on the weak repulsion between ion-image dipoles. Our conclusions are in qualitative agreement with experimental data.

While there are a number of effects ignored by the restricted primitive model — asymmetry of anion and cation sizes, polarizability of ions, and disorder at the electrode surface, to name a few — our results may be quite relevant for real-world experiments on room temperature ionic liquids. A typical ionic liquid has anions and cations with diameter $a \sim 1$ nm, which apparently corresponds to a Helmholtz capacitance $C_H \sim 2$ μF/cm^2 and a dimensionless temperature $T^* \sim 0.02$. This temperature is extremely low, and within the assumptions of the RPM would imply crystallization of ions in the bulk. However, in real RTILs the ions are polarizable, which means that the bulk of the RTIL has a dielectric constant $\varepsilon > 1$ that reduces the magnitude of interactions at long distances; typically $\varepsilon \sim 3$. Thus, T^* should generally be replaced by $\varepsilon T^* \sim 0.06$ and C_H by $\varepsilon C_H \sim 6$ μF/cm^2. In this sense, our result that in the RPM the capacitance can be as large as $3C_H$ should be taken as an indication that polarizable RTILs can have $C \sim 3\varepsilon C_H = 18$ μF/cm^2, a value that is in agreement with typical capacitance measurements on RTILs [18, 19, 20]. The typical electrochemical stability window of about 6 Volts corresponds to $\varepsilon|V^*| \lesssim 12$, which is well within the range of our predictions [47].

Finally, we note that if both ionic species have the same polarizability, then our basic description of the interface remains valid. Polarizability of ions modifies both the attraction energy between ions and the attraction energy between an ion and its image. However, the attraction energy of a pair of oppositely-charged, polarizable ions in the bulk is still equal to the sum of the attraction energies of the two ions to the metal surface, so that at zero voltage the metal surface is highly populated by dissociated ions. At small finite voltage, excess ions seek to maximize their distance from each other, and the resulting correlations allow $C > C_H$ in the way described by Sec. 2.4.

Chapter 3

Capacitance of a one component plasma

In the pursuit of more compact forms of energy storage with high power output, a number of materials, in addition to RTILs, are being investigated for use in electrochemical capacitors [48, 49]. One of these materials is an ion-conducting glass [50, 21], in which small mobile cations move among anions which are large and frozen in place. Simulation results from Sec. 2.5.2 demonstrate that even with asymmetrically sized ions, the capacitance of a room temperature ionic liquid electric (RTIL) may be large, $C > C_H$. The theory presented in Sec. 2.4, however, is not appropriate to describe the capacitance of size–asymmetric RTILs. The goal of this chapter is to provide a theoretical framework for understanding the EDL formed by electrolytes with very large size asymmetries in which one ion is so large that it is sterically prohibited from significant motion, and the other ion is small enough that it may move between the larger ions.

This chapter is based on the work reported in Refs. [51, 52].

3.1 How large can the capacitance be?

A recent experiment [21], has reported much larger values of the EDL capacitance in phosphosilicate glasses placed between platinum electrodes (see Fig. 1.5). Capacitance per unit area as large as 400 μF/cm^2 was measured, corresponding to an effective capacitor thickness $d^* = \varepsilon S/4\pi C$ in the range 0.2 – 0.7 Å, much smaller than any ion

radius. The glass was held at a temperature of 573 K, at which only the smallest ions, Na^+ with diameter $a = 2$Å, are mobile. The dielectric constant of the glass ε is between 2 and 10.

As previously noted, current theories of electric double layer (EDL) capacitors, based on the mean-field approach, fail to explain such large capacitance. The most widely-used theory is that of Gouy, Chapman, and Stern (GCS) [13, 14, 15], which extends the Helmholz capacitor concept to allow for the thermal motion of counterions. When excluded volume of ions is properly taken into account [12, 47, 53, 54, 55, 56] such theories lead only to a larger effective capacitor thickness, and therefore a smaller capacitance than the Helmholtz value.

In this chapter, an alternate theory is proposed to explain the large differential capacitance of the EDL. Following Chapter 2, the mean-field approximation is abandoned and instead discrete ion charges are dealt with. These ions interact strongly with the metal surface in a way that is not captured by the mean-field approximation. For simplicity, this chapter focuses primarily on the case where only the cations are mobile, and therefore may form the EDL, while anions comprise a fixed background of negative neutralizing charge. This "one component plasma" (OCP) model is used here to describe the ion-conducting glasses examined in Ref. [21]. We also suggest a number of other systems to which it can be applied.

One other application of the OCP model is to super-ionic crystals, where only the smallest positive ionic species (such as Na^+ or Li^+) is mobile. Less obvious is the application of the OCP model to ionic liquids, where both positive and negative ions are mobile. Nevertheless, we show below that for ionic liquids composed of monovalent cations and much larger, rigid anions, one can think about space-filling anions as a weakly-compressible negative background on which the small cations rearrange to form the EDL. If the cations are multivalent, then monovalent anions can again be treated as a negative background even if they are of the same size as the cations. These applications will be explained in greater detail in a later section.

Section 3.2 develops the general OCP model of capacitance for a parallel double-plate capacitor, while Sec. 3.3 investigates the capacitance at low temperatures, where all entropic effects can be ignored. Section 3.4 extends this low-temperature theory to the case of an asymmetric double-plate capacitor, where the anode and cathode have

different areas. In the limit of one area going to infinity, this includes the description of a single EDL capacitance. Section 3.5 examines the temperature-dependence of the capacitance, and Sec. 3.6 presents the results of a simple Monte Carlo simulation and compares them with our analytic theory. Section 3.7 examines the application of the OCP model to ionic liquids, and Sec. 3.8 explores its relevance for electrolyte solutions in water. In Sec. 3.9 the main conclusions and summarized and it is argued that this work suggests an improved theory of "pseudo-capacitance".

3.2 One component plasma model

We begin our theory of the OCP model by noting that a cation adjacent to a metal electrode produces electronic polarization of the metal surface, and the cation experiences an attraction to the resulting image charge. For ions of small radius, the image attraction is significantly larger than the thermal energy k_BT, so that ions form stable, compact ion-image dipoles at the metal surface. Cations may also experience some chemically-specific attraction to the metal electrodes, which enhances the effects of image attraction. Repulsion between adjacent dipoles results in the formation of a strongly-correlated liquid of dipoles along the surface of both electrodes. This is in contrast to the model presented in Chapter 2, where the surface layer of excess ions was complicated by the neutral pairs.

The adsorbed cations leave behind a region of negative background, or a depletion layer. Thus, each border of the sample is spontaneously polarized in the direction perpendicular to it (see Fig. 1.3). When a voltage V is applied between the electrodes, these opposite-facing, spontaneous polarizations are easily rearranged in the direction of the external electric field, leading to the rapid build-up of an electronic charge $\pm Q$ on the metal surfaces.

As the charge $\pm Q$ is added to the electrodes, cations are driven to detach from the positive electrode and to bind to the negative one. Below, we demonstrate that the resulting capacitance dQ/dV of the two EDLs can be significantly larger than the Helmholtz value $C_H/2$, since the dipole-dipole repulsion that resists ion transfer is relatively small. In other words, the effective capacitor thickness d^* can be much smaller than the ion radius. Below we derive an expression for d^* that is reasonably close to

experimental values. Our theory also explains another peculiarity of the experiment [21], namely the sharp drop in capacitance at a certain critical voltage, as in Fig. 1.5. We show that, indeed, the capacitance should collapse to a much smaller value at a particular nonzero voltage. Contrary to the mean-field theories developed in Refs. [12, 53, 54, 47, 55, 56], this drop-off (shoulder) in capacitance is not driven by excluded volume effects among bound ions. Rather, it occurs far below the complete filling of an ionic layer at either electrode [57], when the voltage difference induces the positively-charged electrode to lose all of its bound ions.

3.3 Low-temperature theory of a symmetric parallel-plate capacitor

We consider the case of a parallel-plate capacitor, where an ion-conducting medium is bounded on two sides by metal plates which are maintained at a relative potential difference V by some voltage source. The intervening medium is modeled as a fixed negative background with charge density $-eN$, upon which resides a neutralizing concentration of mobile positive ions with charge $+e$ and bulk density N. We model the conducting ions as hard spheres with diameter a, and this Chapter generally assumes that $Na^3 \ll 1$. When an ion is up against the metal surface, it experiences an attractive potential energy of approximately

$$u_{im} = -\frac{e^2}{2\varepsilon a}. \tag{3.1}$$

For $T = 573$ K, $\varepsilon = 5$, and $a = 2$ Å, as estimated for the experiments of Ref. [21], we get $|u_{im}|/k_BT \approx 15$, so that such ions are bound strongly to the surface. In fact, the attraction of ions to the metal surface may be stronger than u_{im}, either because of local behavior of the dielectric constant or because of some specific chemical affinity that ions may have for the metal surface. In general, we will write the strength of ion attraction to the metal surface as γu_{im}, where γ is a positive constant of order one. Unless otherwise stated, all numerical estimates will use $\gamma = 1$.

At a given voltage V, some area densities n_1 and n_2 of ions bind to the anode and cathode, respectively. The attachment of these positive ions to the metal surface results in the formation of regions with negative net charge q_1 and q_2 near the anode

and cathode, respectively. Each of these charges exactly cancels the net charge of the adjoining plate and its bound ions, so that there is no electric field in the bulk of the ionic conductor. This implies $q_1 = -en_1S - Q$ and $q_2 = -en_2S + Q$, where Q is the electronic charge that moves through the voltage source. In other words, the dipoles at each metal-glass interface are effectively embraced by a capacitor composed of the charge q and its positive image $-q$ in the metal. As in every plane capacitor, the charges q_1 and q_2 are uniformly distributed along the plane.

Since positive ions gain a large energy $|u_{im}|$ by adsorbing to the metal surface, at equilibrium there must be a correspondingly large potential difference $V_{im} \equiv |u_{im}|/e$ between the metal surface and the bulk of the ionic conductor, so that the chemical potential of ions is uniform. This large potential difference can be defined as the potential of zero charge (PZC), which has a nonzero value because of the strong spontaneous polarization of the system. In this Chapter we consistently use the external electrode-electrode potential V, which by definition is zero when there is no charge Q on the electrode surfaces, to define capacitance, rather than the potential difference between the electrode and the bulk.

With such a large internal potential difference $V_{im} \gg k_BT/e$ at each electrode, the negative regions are strongly depleted of ions even at very small applied voltage V. The charges q_1 and q_2 therefore constitute depletion layers of width z_1 and z_2 which form at the anode and cathode, respectively; here it is assumed that $z_1, z_2 \gg a$. These layers are devoid of mobile ions and have a charge density equal to that of the negative background, so that $q_1 = -eNz_1$ and $q_2 = -eNz_2$. Thus

$$eNz_1 - en_1 = Q/S \tag{3.2}$$

$$eNz_2 - en_2 = -Q/S, \tag{3.3}$$

where Q is the electronic charge that moves through the voltage source of the capacitor. The electrostatic energy associated with the formation of the depletion layers and their corresponding positive image charge in the metal can be estimated as

$$U_{dep} = \frac{2\pi e^2 S}{3\varepsilon N}\left[\left(n_1 + \frac{Q}{Se}\right)^3 + \left(n_2 - \frac{Q}{Se}\right)^3\right]. \tag{3.4}$$

Fig. 3.1 gives a schematic depiction of the potential energy $w(z)$ of an ion near the anode as a function of its distance z from the metal surface, relative to a position in the

bulk of the ionic conductor. There are two main contributions to $w(z)$: the attraction energy $w_{im}(z) = -e^2/4\varepsilon z$ of the ion to its image charge and the electrostatic energy $w_{dep}(z) = 2\pi e^2 N(z_1 - z)^2/\varepsilon$ associated with moving the ion from the bulk into the depletion region. At equilibrium, these two contributions satisfy $w_{im}(a/2) = u_{im} = -w_{dep}(a/2)$, so that bound ions at the surface have the same energy as ions in the bulk and the chemical potential is uniform.

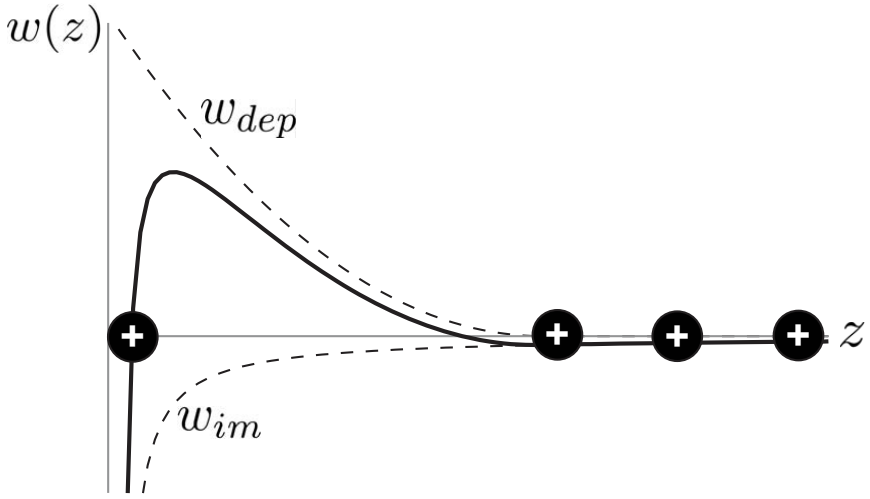

Figure 3.1: Schematic depiction of the potential energy $w(z)$ of an ion in the vicinity of the metal plate. The image attraction energy w_{im} and the energy associated with moving through the depletion layer w_{dep} are shown as a function of distance z from the metal surface, along with the total $w = w_{im} + w_{dep}$. At equilibrium, ions bound to the surface have the same potential energy as ions in the bulk.

Eq. (3.4) assumes that positive bound ions are effectively neutralized by their negative image charges, so that these ions can be ignored in calculating the electrostatic self-energy of the depletion region and its image charge. One can consider, however, the small correction to Eq. (3.4) resulting from the interaction between bound ion-image pairs and the negative background. In the limit $z_1, z_2 \gg a$, this correction can be viewed as the potential energy of a collection of ion-image dipoles, each with dipole moment $|\vec{p}| = ea$, aligned with an external field $\vec{E}$ produced by the negative depletion layer and its positive image charge. If the number of dipoles on a given metal surface is nS, then the total interaction energy of these dipoles with the external field is $-nS\vec{p}\cdot\vec{E}$, so that

to the energy associated with forming the depletion layers there should be added a term

$$U_{dE} = -4\pi u_{im} S \left[n_1 \left(n_1 + \frac{Q}{eS} \right) + n_2 \left(n_2 - \frac{Q}{eS} \right) \right] a^2. \tag{3.5}$$

In addition to the ions' interaction with the background, there is a positive energy associated with repulsion between bound ions. When the density of bound ions is low enough that $na^2 \ll 1$, ions repel each other by a dipole-dipole interaction: the potential created by a bound ion and its image charge repels an adjacent ion. In this limit the repulsive interaction between two adjacent bound ions is

$$u_{dd}(n) \simeq e^2 a^2 n^{3/2} / 2\varepsilon. \tag{3.6}$$

This repulsion results in the formation of a strongly-correlated liquid of ions on the electrode surface, reminiscent of a two-dimensional Wigner crystal [33]. The total dipole energy at a given plate is $\alpha n S u_{dd}(n)$, where α is a numerical coefficient which depends on the structure of the lattice of dipole positions. Thus, the total dipole interaction energy can be written as

$$U_{dd} = \alpha S [n_1 u_{dd}(n_1) + n_2 u_{dd}(n_2)]. \tag{3.7}$$

For the minimum energy triangular lattice, $\alpha \approx 4.4$. Further calculations will use this value.

We now assemble a full description of the total energy U associated with the bound charge densities n_1 and n_2, taking as our reference the case where $n_1 = n_2 = 0$:

$$U = S(n_1 + n_2)\gamma u_{im} + U_{dep} + U_{dE} + U_{dd} - QV. \tag{3.8}$$

Here, $-QV$ represents the work done by the voltage source.

It should be noted that this expression neglects another potential contribution to the total energy: that of the finite chemical potential of ions in the bulk. At zero temperature, for example, ions in the bulk are crystallized into a three-dimensional Wigner crystal with finite self-energy $u_{WC} \approx -1.4 e^2 N^{1/3}/\varepsilon$ per ion [58]. The energy U is defined relative to the state where no ions have left the bulk, so the attachment of $(n_1 + n_2)S$ ions to the electrodes should involve an additional energy cost of $-(n_1 + n_2) S u_{WC}$. At small N, this energy provides only a small correction to the binding energy u_{im} and can be effectively absorbed into the coefficient γ.

At equilibrium, the values of $Q(V)$, $n_1(V)$, and $n_2(V)$ are those which minimize U. They can therefore be found by the conditions $\partial U/\partial Q = \partial U/\partial n_1 = \partial U/\partial n_2 = 0$, the latter two of which produce

$$\frac{5\alpha}{2} n_1^{3/2} a^3 + \frac{4\pi}{Na^3}\left(n_1 + \frac{Q}{eS}\right)^2 a^4 = \gamma + 4\pi\left(2n_1 + \frac{Q}{eS}\right)a^2, \tag{3.9}$$

$$\frac{5\alpha}{2} n_2^{3/2} a^3 + \frac{4\pi}{Na^3}\left(n_2 - \frac{Q}{eS}\right)^2 a^4 = \gamma + 4\pi\left(2n_2 - \frac{Q}{eS}\right)a^2. \tag{3.10}$$

If ions are relatively sparse in the bulk, so that $Na^3 \ll 1$, then the first and final terms of both equations can be neglected. Setting $Q = 0$ suggests that at zero voltage, when the net charge of the capacitor is zero, there is still a finite concentration n_0 of ions bound to each plate given by

$$n_0 a^2 \simeq \sqrt{\frac{\gamma N a^3}{4\pi}} \ll 1. \tag{3.11}$$

Since the "filling factor" na^2 on each metal surface is small, bound ions are sufficiently distant that our approximation of a dipole interaction between them is justified. This condition also verifies our assumption that the first and final terms of Eqs. (3.9) and (3.10) are much smaller than unity.

As the voltage is increased from zero, ions are driven away from the anode and attracted to the cathode, so that n_1 decreases and n_2 increases. Eqns. (3.9) and (3.10) imply that n_1 and n_2 depend linearly on Q:

$$n_0 - n_1 \simeq Q/eS, \tag{3.12}$$

$$n_2 - n_0 \simeq Q/eS. \tag{3.13}$$

Subtraction of Eqs. (3.12) and (3.13) suggests that the total number of adsorbed ions $n_1 + n_2 \simeq 2n_0$ per unit area remains almost constant with increasing voltage. This result is a direct consequence of the large difference between the depletion layer energy U_{dep} and the dipole-dipole energy $\alpha S n u_{dd}(n)$. Indeed, by comparing Eqs. (3.4) and (3.7), we see that the condition $Na^3 \ll 1$ implies that the energy cost associated with increasing the total number of bound ions, and thereby causing the depletion layers to swell, is much larger than the dipole-dipole interaction energy. As a consequence, the total number of bound ions remains nearly constant with voltage. The electronic charge

$Q \simeq eS(n_2 - n_1)/2$ that passes through the voltage source can therefore be thought of as the corresponding movement of image charges from one plate to another.

When enough charge has moved through the voltage source that $Q = eSn_0$, the anode becomes completely depleted of bound ions, so that $n_1 = 0$ and $n_2 \simeq 2n_0$. This corresponds to a particular voltage V_c. At voltages $V > V_c$, the number of bound ions on the non-depleted electrode may still increase, but only through the costly widening of the depletion layer.

A relation between charge Q and voltage V can be derived by substituting Eqs. (3.12) and (3.13) into Eq. (3.8), so that the total energy $U(Q)$ is written as a function of the charge only. A subsequent application of the condition $\partial U/\partial Q = 0$ gives

$$V \simeq \frac{5\alpha}{2}\left[\left(n_0 + \frac{Q}{eS}\right)^{3/2} - \left(n_0 - \frac{Q}{eS}\right)^{3/2}\right] a^3 V_{im}. \tag{3.14}$$

By taking the derivative of this expression with respect to V, we can derive the capacitance $C = dQ/dV$. This gives

$$\begin{aligned} C &= \frac{8}{15\alpha}\left[\left(\frac{\varepsilon S}{a\sqrt{n_0 a^2 - Qa^2/eS}}\right)^{-1} + \right. \\ &\qquad \left.\left(\frac{\varepsilon S}{a\sqrt{n_0 a^2 + Qa^2/eS}}\right)^{-1}\right]^{-1}. \end{aligned} \tag{3.15}$$

In this expression the terms inside the parentheses represent the capacitance of the anode and cathode, respectively, which add like capacitors in series. At zero voltage, $Q = 0$, so that the capacitance becomes

$$C(0) \simeq \frac{4}{15\alpha}\left(\frac{4\pi}{\gamma N a^3}\right)^{1/4}\frac{\varepsilon S}{a} = \frac{8\pi}{15\alpha}\left(\frac{4\pi}{\gamma N a^3}\right)^{1/4} C_H. \tag{3.16}$$

For $Na^3 \ll 1$ one gets $C(0) \gg C_H/2$ because at small voltages charging of the capacitor is limited only by the dipole-dipole repulsion energy. Since $n_0 a^2 \ll 1$, the dipole-dipole interaction is weak, so that the resulting capacitance can be large.

At higher voltages, the capacitance of the EDL near the positive plate increases strongly as this plate becomes depleted of ions and the corresponding dipole repulsion energy goes to zero. Thus the contribution of the positive plate to the total capacitance

vanishes when $Q = en_0S$. The corresponding voltage V_c can be found by substituting $Q = en_0S$ into Eq. (3.14):

$$V_c \simeq \frac{5\alpha}{2}\left(\frac{\gamma N a^3}{\pi}\right)^{3/4} V_{im}. \tag{3.17}$$

Immediately prior to $V = V_c$, the capacitance achieves its maximum value

$$C_{max} \simeq \frac{8}{15\alpha}\left(\frac{\pi}{\gamma N a^3}\right)^{1/4} \frac{\varepsilon S}{a} = \sqrt{2}C(0). \tag{3.18}$$

The effective thickness d^*_{min} corresponding to C_{max} is

$$d^*_{min} \simeq \frac{15\alpha}{32\pi}\left(\frac{\gamma N a^3}{\pi}\right)^{1/4} a \approx 0.49\left(Na^3\right)^{1/4} a. \tag{3.19}$$

Thus we arrive at a remarkable prediction: the effective capacitor thickness can be much smaller than the ion diameter a. As an example, an ion-conducting medium with mobile sodium atoms of diameter $a = 2$ Å and density $Na^3 = 0.01$ can be used to make a capacitor with capacitance nearly six times larger than $C_H/2$. As mentioned before, this surprisingly high capacitance is a result of the weak dipole-dipole interaction between bound ions that comprise the double-layer. Indeed, near the capacitance maximum the filling factor on the negative plate $n_2a^2 \simeq 2n_0a^2 \ll 1$, so that it is incorrect to think of the EDL as a series of uniformly charged layers. This difference represents an important change of paradigm, from a mean-field capacitor to a capacitor composed of discrete, correlated dipoles.

At $V > V_c$, ions can no longer simply be transferred from anode to cathode, and the capacitance collapses to a much smaller value. The value of this "depleted capacitance" can be found through optimization of the total energy U under the condition $n_1 = 0$, which yields

$$C_{dep}(V) \simeq \frac{\varepsilon S}{a}\sqrt{\frac{Na^3}{4\pi(V/V_{im} + \gamma)}}. \tag{3.20}$$

This expression neglects the weak dipole-dipole interaction at the non-depleted negative plate. At $V/V_{im} \gg \gamma$ the capacitance is dominated by the depletion layer next to the positive electrode, and therefore it approaches the standard value for capacitance of a depletion layer.

Fig. 3.2 shows the capacitance and the density of bound ions as a function of voltage, as calculated by a numerical minimization of the total energy in Eq. (3.8). We have

used $Na^3 = 0.1$, following the estimate of Ref. [21]. All results are within 10% of the approximate analytic expressions in Eqs. (3.11) – (3.13), (3.15) – (3.20).

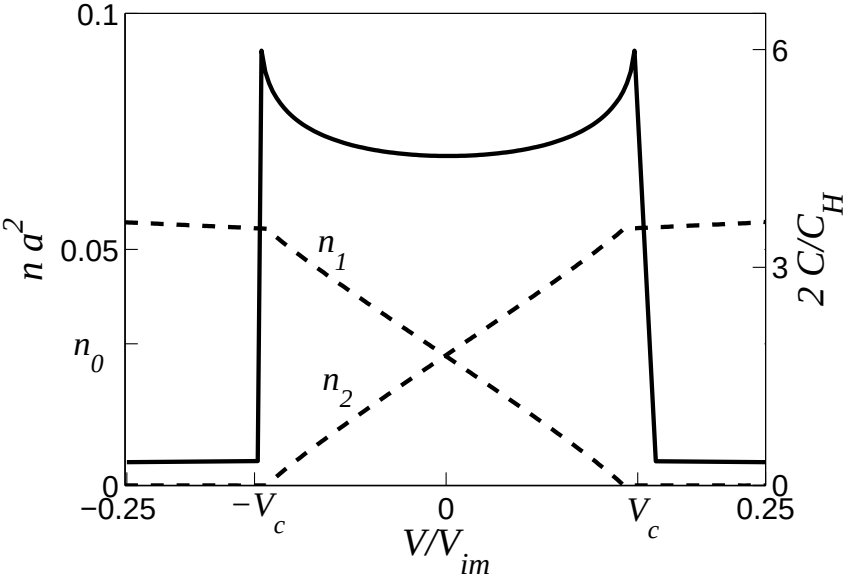

Figure 3.2: The area densities of bound ions (dashed lines, left vertical axis) and the capacitance (solid line, right vertical axis) as a function of applied voltage for $Na^3 = 0.01$, as given by a numerical minimization of the total energy in Eq. (3.8)

3.4 Low-temperature theory of an asymmetric Capacitor

We may also consider the case of an asymmetric capacitor, where the two electrodes have unequal areas. This may be the case, for example, in a coaxial cylindrical capacitor where the inner electrode has a smaller radius than the outer electrode. For the sake of argument, we assume that at positive voltages the smaller electrode (area S_1) is the anode and the larger electrode (area S_2) is the cathode. The corresponding Helmholtz capacitance for the double layer at each electrode is $C_{H,1} = \varepsilon S_1/2\pi a$ and $C_{H,2} = \varepsilon S_2/2\pi a$ for the small and large electrodes, respectively. These two capacitances add in series, so that by the GCS theory the maximum possible capacitance is

$$\left(\frac{1}{C_{H,1}} + \frac{1}{C_{H,2}}\right)^{-1} = \frac{\varepsilon}{2\pi a}\left(\frac{1}{S_1} + \frac{1}{S_2}\right)^{-1}. \tag{3.21}$$

When $S_1 = S_2 = S$, this result reduces to $C_H/2$, as in the previous section. In the limit $S_2 \gg S_1$, Eq. (3.21) approaches $C_{H,1}$, so that the total capacitance is limited by the smaller area.

Let us now see how our theory of the previous section can be generalized to the asymmetric case. The conditions of neutrality at anode and cathode become

$$eNz_1 - en_1 = Q/S_1 \tag{3.22}$$

$$eNz_2 - en_2 = -Q/S_2, \tag{3.23}$$

so that the electrostatic energy of the depletion layers can be written as

$$U_{dep} = \frac{2\pi e^2}{3\varepsilon N}\left[S_1\left(n_1 + \frac{Q}{S_1 e}\right)^3 + S_2\left(n_2 - \frac{Q}{S_2 e}\right)^3\right]. \tag{3.24}$$

Similarly, the interaction between dipoles and the depletion layer becomes

$$U_{dE} = -4\pi u_{im}\left[n_1 S_1\left(n_1 + \frac{Q}{eS_1}\right) + n_2 S_2\left(n_2 - \frac{Q}{eS_2}\right)\right]a^2. \tag{3.25}$$

and the total dipole-dipole interaction energy is

$$U_{dd} = \alpha\left[S_1 n_1 u_{dd}(n_1) + S_2 n_2 u_{dd}(n_2)\right]. \tag{3.26}$$

The total energy is therefore

$$U = (S_1 n_1 + S_2 n_2)\gamma u_{im} + U_{dep} + U_{dE} + U_{dd} - QV. \tag{3.27}$$

As before, the values of $Q(V)$, $n_1(V)$, and $n_2(V)$, are those which minimize U.

At zero voltage, the conditions $\partial U/\partial n_1 = \partial U/\partial n_2 = 0$ suggest $n_1 = n_2 = n_0$, where n_0 is the same as in the symmetric case [Eq. (3.11)]. At finite V they imply

$$n_0 - n_1 = Q/eS_1 \tag{3.28}$$

$$n_2 - n_0 = Q/eS_2, \tag{3.29}$$

so that, as in the symmetric case, the charge Q can be thought of as the movement of image charges from one electrode to another. Here we have again assumed that $Na^3 \ll 1$.

Using Eqs. (3.28) and (3.29), we can rewrite the total energy as a function of Q only. By optimizing $U(Q)$ with respect to Q we obtain an expression $V(Q)$ from which we can define the capacitance. This procedure yields

$$V \simeq \frac{5\alpha}{2}\left[\left(n_0 + \frac{Q}{eS_2}\right)^{3/2} - \left(n_0 - \frac{Q}{eS_1}\right)^{3/2}\right] a^3 V_{im}. \tag{3.30}$$

Taking the derivative with respect to V, and using $C = dQ/dV$, we get

$$\begin{aligned} C &= \frac{8}{15\alpha}\left[\left(\frac{\varepsilon S_1}{a\sqrt{n_0 a^2 - Qa^2/eS_1}}\right)^{-1} + \right. \\ &\qquad \left.\left(\frac{\varepsilon S_2}{a\sqrt{n_0 a^2 + Qa^2/eS_2}}\right)^{-1}\right]^{-1}. \end{aligned} \tag{3.31}$$

In this expression the terms inside the parentheses represent the capacitance of the anode and cathode, respectively, which add like capacitors in series. At zero voltage, $Q = 0$, so that the capacitance becomes

$$C(0) \simeq \frac{8}{15\alpha}\left(\frac{4\pi}{\gamma N a^3}\right)^{1/4} \frac{\varepsilon}{a}\left(\frac{1}{S_1} + \frac{1}{S_2}\right)^{-1}. \tag{3.32}$$

When $S_1 = S_2$, this expression reduces to the symmetric result of Eq. (3.16). When $S_1 \ll S_2$, the capacitance is dominated by the smaller area, as expected. In either case, $C(0)$ is again much larger than the corresponding Helmholtz values $C_H/2$ and $C_{H,1}$.

Below we consider the behavior of the capacitance as a function of voltage, examining separately the cases of positive and negative voltage applied to the small electrode.

3.4.1 Positive voltage

When the voltage is increased from zero, the capacitance increases as ions unbind from the anode and bind to the cathode. At a certain critical voltage $V_{c,1}$ the anode becomes depleted of bound ions. This occurs when $n_1 = 0$, or $Q = eS_1 n_0$, so that by Eq. (3.30)

$$V_{c,1} \simeq \frac{5\alpha}{2}\left(\frac{\gamma N a^3}{4\pi}\right)^{3/4}\left(1 + \frac{S_1}{S_2}\right)^{3/2} V_{im}. \tag{3.33}$$

At this point, the double-layer capacitance of the anode diverges as ions bound to the anode become sparse and the corresponding dipole-dipole interaction energy goes to

zero. The total capacitance is therefore limited only by the capacitance of the cathode. Substituting $Q = eS_1 n_0$ into Eq. (3.31) gives

$$C(V_{c,1}) \simeq \frac{S_2}{S_1}\sqrt{\frac{S_1+S_2}{S_2}}C(0). \tag{3.34}$$

When the cathode is much larger than the anode, $S_2/S_1 \gg 1$, the maximum capacitance $C(V_{c,1}) \simeq C(0)S_2/S_1$. This result implies a tremendous growth in the capacitance at positive voltages $0 < V < V_{c,1}$. For voltages just below the critical value, so that $V_{c,1} - V \ll V_{c,1}$, we can examine this growth analytically. At $S_2/S_1 \gg 1$ we can ignore the term Q/eS_2 in Eq. (3.30) and we arrive at $(n_0a^2 - Qa^2/eS_1)^{3/2} = (V_{c,1} - V)/V_{im}$. Substituting this result for the first term of the sum in Eq. (3.31) (the inverse capacitance of the smaller electrode) and ignoring the second term (the inverse capacitance of the larger electrode), we find that the capacitance diverges approximately as

$$C(V) \simeq \frac{4}{3}\left(\frac{2}{5\alpha}\right)^{2/3}\left(\frac{V_{im}}{V_{c,1}-V}\right)^{1/3}\frac{\varepsilon S_1}{a}, \quad (0 < V < V_{c,1}) \tag{3.35}$$

before being truncated by the finite value of S_2 as given in Eq. (3.34). At $V = 0$, Eq. (3.35) approximately matches the capacitance $C(0)$ from Eq. (3.16).

At larger voltages $V > V_{c,1}$, the anode becomes depleted of ions and the capacitance collapses to a much smaller value. This value can be found through minimization of the total energy U with respect to Q under the condition $n_1 = 0$, which gives

$$C_{dep,1}(V) \simeq \sqrt{\frac{Na^3}{4\pi(V/V_{im}+\gamma)}}\frac{\varepsilon S_1}{a}, \quad (V > V_{c,1}). \tag{3.36}$$

In other words, the capacitance at large positive voltages is dominated by that of the growing depletion layer at the anode, as in Eq. (3.20) for the symmetric case.

Fig. 3.3 shows the capacitance as a function of voltage for different values of S_2/S_1, as calculated by numerical minimization of the total energy in Eq. (3.27). For $V > 0$, this figure illustrates the analytical results of Eqs. (3.33) – (3.36). For $V < 0$ it shows the predictions of the following subsection. Notice that at large values of S_2/S_1 the divergence in the capacitance near $V = V_{c,1}$ becomes increasingly pronounced.

3.4.2 Negative voltage

So far we have been talking about the case of a small anode and large cathode. We now consider the situation of negative voltage V, where the electrodes change roles

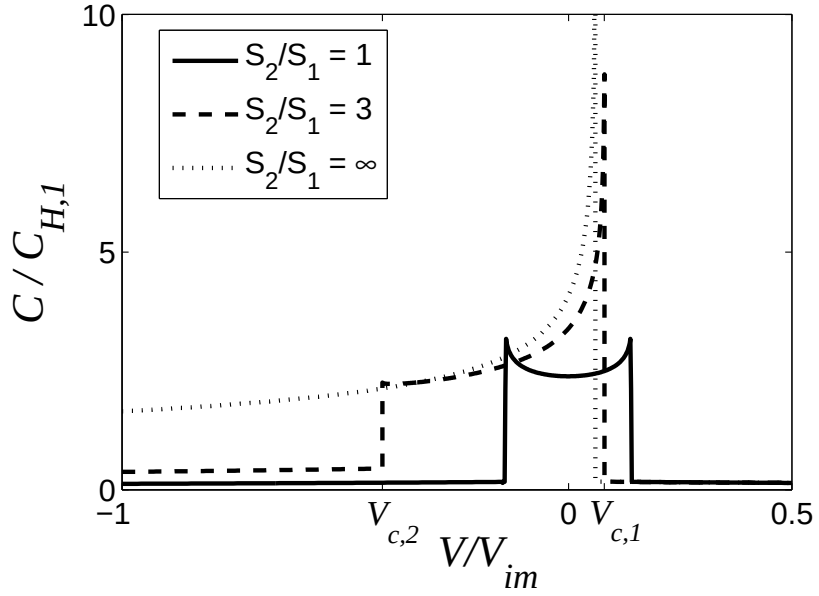

Figure 3.3: The capacitance as a function of voltage for different ratios S_2/S_1, as calculated by numerical minimization of the total energy, for $Na^3 = 0.01$. Threshold voltages $V_{c,1}$ and $V_{c,2}$ are shown for the dashed line only.

and the cathode area S_1 is smaller than the anode area S_2. This change in electrode roles suggests an asymmetry in the total capacitance with respect to the sign of the voltage. Below we examine the capacitance at negative voltages for two limiting cases: the moderately asymmetric case $S_2/S_1 \ll 1/\sqrt{Na^3}$ and the highly asymmetric case $S_2/S_1 \gg 1/\sqrt{Na^3}$.

Moderately asymmetric capacitor

If the two electrode areas are not too different, so that $S_2/S_1 \ll 1/\sqrt{Na^3}$, then the capacitance at negative voltages can be described using the same procedure as for positive voltage, beginning with Eqs. (3.30) – (3.31). The voltage $V_{c,2}$ at which the larger electrode becomes depleted of bound ions can be found by setting $Q = -eS_2n_0$ in Eq. (3.30), which gives

$$V_{c,2} = -\left(\frac{S_2}{S_1}\right)^{3/2} V_{c,1}. \tag{3.37}$$

The large electrode therefore becomes depleted at larger voltages (in absolute value) than the small electrode (see the dashed line in Fig. 3.3). The condition $S_2/S_1 \ll 1/\sqrt{Na^3}$ guarantees that $|V_{c,2}| < V_{im}$.

At larger negative voltages $V < V_{c,2}$, there is an apparent collapse in capacitance due to the depletion of bound ions at the larger electrode. The capacitance immediately prior to this voltage

$$C(V_{c,2}) \simeq \frac{S_1}{S_2}\sqrt{\frac{S_1+S_2}{S_1}}C(0) = \left(\frac{S_1}{S_2}\right)^{3/2} C(V_{c,1}). \tag{3.38}$$

This value is smaller than the maximum capacitance $C(V_{c,1})$ since the capacitance at $V_{c,2}$ is limited by the capacitance of the smaller electrode while at $V_{c,1}$ it is limited by the larger electrode. For voltages beyond the collapse point, $V < V_{c,2}$, the total capacitance can be found through minimization of U under the condition $n_2 = 0$, which yields

$$C_{dep,2}(V) \simeq \sqrt{\frac{Na^3}{4\pi(\gamma - V/V_{im})}}\frac{\varepsilon S_2}{a}, \quad (V < V_{c,2}). \tag{3.39}$$

This capacitance is similar to Eqs. (3.20) and (3.36), and is determined by the growing depletion layer at the larger electrode.

Highly asymmetric capacitor

We now consider the opposite limit of electrode areas, when S_2 and S_1 are so different that $S_2/S_1 \gg 1/\sqrt{Na^3}$. In this case there is no apparent collapse in the capacitance at any negative voltage $-V_{im} < V < 0$ (see the dotted line in Fig. 3.3). Rather, Eqs. (3.30) and (3.31) imply a continuous increase in capacitance with voltage as in Eq. (3.35):

$$C(V) \simeq \frac{4}{3}\left(\frac{2}{5\alpha}\right)^{2/3}\left(\frac{V_{im}}{V_{c,1}-V}\right)^{1/3}\frac{\varepsilon S_1}{a}, \quad (-V_{im} < V < V_{c,1}). \tag{3.40}$$

Notice that at $V = -V_{im}$ the capacitance becomes approximately equal to the Helmholtz value $C(-V_{im}) \simeq C_{H,1}$.

At larger negative voltages $V < -V_{im}$ our description of the total energy loses its validity, since Eq. (3.30) implies a near-complete filling of this electrode by bound ions, $n_1 a^2 \simeq 1$. Thus the assumption of a dipole-dipole interaction between bound ions is

no longer accurate. At $V \ll -V_{im}$, the capacitance of the smaller electrode should be dominated by the accumulation of complete ionic layers at the small (*negative*) electrode, as described by the theories of Refs. [53, 54, 55, 47, 12, 56]. This is opposite to the result of the symmetric case, where the capacitance at large negative voltages is determined by the growth of the depletion layer next to the *positive* electrode. Instead, the large difference between S_2 and S_1 guarantees that the capacitance of the smaller electrode is much lower, and it therefore determines the total. The corresponding capacitance at such large negative voltages is

$$C(V) \simeq \sqrt{\frac{-V_{im}}{4\pi V}}\frac{\varepsilon S_1}{a}, \quad (V \ll -V_{im}). \tag{3.41}$$

At $V = -V_{im}$, this capacitance also approaches the Helmholtz value $C(-V_{im}) \simeq C_{H,1}$, so that Eqs. (3.40) and (3.41) match at $V \simeq -V_{im}$.

Eqs. (3.40) and (3.41) indicate that in the limit $S_2/S_1 \gg 1/\sqrt{Na^3}$ the capacitance does not depend on the area of the large electrode S_2. Rather, it is totally determined by the physics of the double-layer near the small electrode. Therefore, we can view this result as the capacitance of a single small electrode ($S_2 \to \infty$). While the result of Eq. (3.41) is known [53, 54, 55, 47, 12, 56], we could not find that of Eq. (3.40) in the literature . In the range of its validity, the capacitance grows with increasing voltage V from $C \sim C_{H,1}$ at $V = -V_{im}$ and actually diverges at $V = V_{c,1}$. Thus the effective thickness d^* of a single interface vanishes at $V = V_{c,1}$! Of course, this result is valid only at zero temperature. As shown in next section, finite temperature truncates this divergence.

3.5 Temperature Dependence of Capacitance

In the previous sections, we derive capacitance by minimization of the total electrostatic energy and do not include any entropic effects associated with the finite thermal energy of ions. Here we consider the dependence of capacitance on temperature.

Until now, bound ions have been assumed to occupy their ground state configuration: a two-dimensional Wigner crystal. Since the capacitance is limited only by the resulting dipole-dipole interaction between ions, our prediction for the capacitance is highly dependent on the validity of this description. If thermal motion of bound ions

produces a significant correction to the repulsive interaction between them, than the capacitance will be different than our "zero-temperature" prediction of the previous sections.

In general, when the two electrodes have area S_1, S_2, the total free energy of the system can be written as

$$\begin{aligned} F &= (S_1 n_1 + S_2 n_2)\gamma u_{im} + U_{dep} + U_{dE} + \\ &\quad S_1 f(n_1) + S_2 f(n_2) - QV, \end{aligned} \tag{3.42}$$

where $f(n)$ represents the free energy per unit area of the two-dimensional collection of bound ions that forms at a given interface, which includes dipole-dipole repulsion and thermal motion along the metal surface. At low temperatures $k_B T \ll u_{dd}(n_0)$, bound ions are crystallized and $f(n) \simeq \alpha n u_{dd}(n)$, so that Eq. (3.42) becomes equal to Eq. (3.27) and we regain the results of our low-temperature theory. If the average free energy per ion along each metal surface is small enough that $df/dn \ll u_{im}$, and the voltage is small enough that we still have $n_1, n_2 \ll 1/a^2$, then the equilibrium requirements $\partial F/\partial n_1 = \partial F/\partial n_2 = 0$ imply

$$n_0 - n_1 = Q/eS_1 \tag{3.43}$$

$$n_2 - n_0 = Q/eS_2, \tag{3.44}$$

as before.

As a consequence, for sufficiently small voltages $|V| < V_c$, where neither metal surface is depleted of bound ions, the sum $n_1 + n_2 = 2n_0$ remains constant. The condition $\partial F/\partial Q = 0$, along with $\partial n_1/\partial Q = -1/eS_1$ and $\partial n_2/\partial Q = -1/eS_2$, gives

$$eV = f'(n_2) - f'(n_1). \tag{3.45}$$

Here, the $'$ denotes a derivative with respect to the argument. The capacitance dQ/dV is therefore

$$C = e^2 \left[\frac{f''(n_1)}{S_1} + \frac{f''(n_2)}{S_2} \right]^{-1}. \tag{3.46}$$

Generally speaking, Eq. (3.46) can be combined with Eqs. (3.43) – (3.45) to give an analytic relation for the capacitance as a function of voltage at a given temperature: $C(V,T)$. This section will focus primarily on the temperature dependence of the zero-voltage capacitance $C(0,T)$ and on the capacitance maximum $C_{max}(T)$.

3.5.1 Zero-voltage capacitance

According to Eq. (3.46), the capacitance at zero voltage can be written

$$C(0,T) = \frac{e^2}{f''(n_0)} \left(\frac{1}{S_1} + \frac{1}{S_2} \right)^{-1}, \tag{3.47}$$

so the capacitance is fully determined by the (temperature-dependent) free energy of ions along the metal surface, $f(n)$. The behavior of this contribution can be separated into three regimes of temperature.

Low Temperature

At very low temperature $k_B T \ll u_{dd}(n_0)$, one can imagine that each ion in the Wigner crystal undergoes small thermal oscillations in the confining potential created by its neighbors. If this potential is expanded to second-order in the displacement r from the potential energy minimum, then the average squared thermal displacement is

$$\langle r^2 \rangle \approx \frac{\varepsilon k_B T}{13.5 e^2 a^2 n^{5/2}}, \tag{3.48}$$

again assuming a triangular lattice of dipoles. The positional entropy of a bound ion, relative to an unbound state in the bulk, can be estimated as $\ln(\langle r^2 \rangle / a^2) - \ln(1/Na^3)$. The free energy per unit area $f(n)$ of bound ions is therefore

$$f(n) \simeq n \left[\alpha u_{dd}(n) - k_B T \ln \left(N \langle r^2 \rangle a \right) \right], \tag{3.49}$$

The corresponding zero-voltage capacitance

$$C(0,T) = C(0,0) \left[1 + \frac{2}{3\alpha} \frac{k_B T}{u_{dd}(n_0)} \right]^{-1}. \tag{3.50}$$

where $C(0,0)$ is the zero-voltage capacitance described by Eq. (3.32).

Intermediate Temperature

At sufficiently large temperatures that $k_B T \gg u_{dd}(n_0)$ but $k_B T \ll u_{im}$, the crystal-like order of dipoles is destroyed, and bound ions are better described as a two-dimensional ideal gas than as a Wigner crystal. In this limit, the free energy per unit area of bound ions $f(n)$ can be approximated as that of a two-dimensional ideal gas,

$$f_{id}(n) = -n k_B T \ln \left(\frac{Na^3}{na^2} \right). \tag{3.51}$$

Here we again define the entropy of an ion relative to the bulk.

The description of Eq. (3.51) assumes that ions are non-interacting, so that their free energy is determined purely by entropic motion. The effect of relatively weak interaction between ions can be included by a virial expansion of the free energy,

$$f \simeq f_{id} + n^2 k_B T B(T). \tag{3.52}$$

Here, $B(T)$ is the second virial coefficient, calculated from the dipole-dipole interaction energy $u(r)$ between bound ions as

$$\begin{aligned} B(T) &= \frac{1}{2}\int_0^\infty \left(1 - e^{-u(r)/k_B T}\right) 2\pi r dr, & (3.53)\\ &\approx 2.65 \left(\frac{e^2 a^2}{\varepsilon k_B T}\right)^{2/3}. & (3.54) \end{aligned}$$

By Eq. (3.47), the resulting capacitance is

$$C(0,T) = \frac{e^2 n_0}{k_B T}\left[1 + 5.3\left(\frac{2u_{dd}(n_0)}{k_B T}\right)^{2/3}\right]^{-1}\left(\frac{1}{S_1} + \frac{1}{S_2}\right)^{-1}. \tag{3.55}$$

If the temperature is low enough that $k_B T \ll u_{im}(Na^3)^{1/3}$, then all other corrections to the capacitance beyond that of the virial coefficient are parametrically smaller in Na^3.

One can estimate the transition temperature T_1 between Eqs. (3.50) and (3.55) by equating them, which gives

$$T_1 \approx 7.9\alpha^{3/5} u_{dd}(n_0)/k_B. \tag{3.56}$$

As expected, the transition occurs when the thermal energy is of the same order as the dipole-dipole interaction energy.

High Temperature

At much larger temperatures $k_B T \gg u_{im}$, ions no longer bind to the metal surface. Since at these temperatures the change in potential at a given electrode is small compared to the thermal energy, the attraction of ions to the metal produces only a small perturbation in the overall ion density. Ions therefore form a diffuse screening layer around each metal surface, with a width equal to the Debye-Hückel screening radius

$$r_s = \sqrt{\frac{\varepsilon k_B T}{4\pi e^2 N}}. \tag{3.57}$$

The resulting capacitance per unit area of the double-layer is $\varepsilon/4\pi r_s$, so that the total capacitance of the two double-layers in series is

$$C_{DH} = \frac{\varepsilon}{4\pi r_s}\left(\frac{1}{S_1} + \frac{1}{S_2}\right)^{-1}. \tag{3.58}$$

The crossover temperature T_2 between the Debye-Hückel capacitance C_{DH} and the intermediate-temperature value can be found by equating Eqs. (3.55) and (3.58), which gives

$$T_2 = 2\gamma u_{im}/k_B. \tag{3.59}$$

Fig. 3.4 shows a schematic depiction of $C(0)$ in all three regimes of temperature, plotted for two different values of the density Na^3.

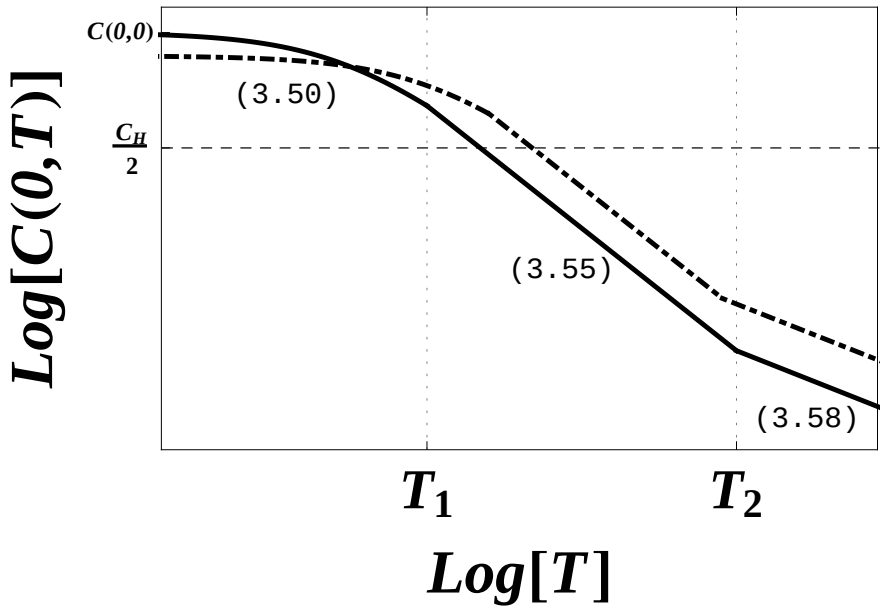

Figure 3.4: Schematic depiction of the temperature dependence of the zero-voltage capacitance of a parallel-plate capacitor. Numbers in parentheses indicate the formula describing each portion of the temperature dependence. The dash-dotted line corresponds to a higher value of the density Na^3, which produces a lower zero-temperature capacitance and a higher capacitance at large temperatures. The temperature T_1 is indicated for the solid line only.

3.5.2 Maximum capacitance

At zero temperature, the capacitance maximum is associated with a sharp discontinuity in the C-V curve, as shown in Figs. 3.2 and 3.3. At finite temperature, however, entropic effects will tend to smooth out these discontinuities, thereby shifting both the magnitude and position of the capacitance maximum.

At sufficiently low voltages that neither electrode is depleted of bound ions and $n_1, n_2 \ll 1/a^2$, Eq. (3.46) implies that the capacitance is extremized when

$$f'''(n_1) = \left(\frac{S_1}{S_2}\right)^2 f'''(n_2). \tag{3.60}$$

This relation can be used to find the capacitance maximum $C_{max}(T)$ at temperatures $T < T_2$. For high temperatures $T > T_2$, the capacitance is equal to C_{DH} and is essentially constant in voltage.

Below we derive the maximum capacitance for the symmetric case, $S_1/S_2 = 1$, and the highly asymmetric case, $S_1/S_2 \to 0$.

Symmetric capacitor

When the electrode areas are equal, $S_1 = S_2$, Eq. (3.60) becomes

$$f'''(n_1) = f'''(n_2). \tag{3.61}$$

This suggests that at $V = 0$, where $n_1 = n_2 = n_0$, there is always either a maximum or a local minimum in the capacitance. At low temperatures $T \ll T_1$, $V = 0$ is a local minimum. The maximum can be found by solving Eq. (3.61) and then substituting the results for n_1, n_2 into Eq. (3.46), which gives

$$C_{max}(T) \simeq C_{max}(0)\left(1 + 1.2\frac{(k_B T/\alpha u_{im})^{1/3}}{\sqrt{n_0 a^2}}\right)^{-1}. \qquad (T \ll T_1) \tag{3.62}$$

Here, $C_{max}(0)$ is the maximum capacitance at zero temperature, given in Eq. (3.18).

Qualitatively, this result can be explained by considering that the capacitance maximum at zero temperature is driven by a vanishing dipole-dipole interaction at the depleted electrode, which allows the capacitance of that electrode to diverge. At finite

temperature, the free energy of bound ions cannot fall below the thermal energy k_BT, so the capacitance of the nearly-depleted electrode remains finite. Setting $u_{dd}(n_1) = k_BT$ and solving for n_1, while setting $n_2 = 2n_0$, allows one to derive the result of Eq. (3.62) to within a numerical coefficient multiplying the temperature. Note that as T approaches T_1, the capacitance maximum approaches $C(0,T)$ as in Eq. (3.50).

For larger temperatures $T \gg T_1$, the capacitance maximum disappears and the function changes concavity around $V = 0$. Thus, the maximum capacitance becomes equal to the zero-voltage capacitance given in Eq. (3.55). A characteristic set of capacitance-voltage curves corresponding to this range of temperature is shown in Fig. 3.6.

Highly asymmetric capacitor

For the case $S_2 \gg S_1$, our zero-temperature theory in the previous section predicts a sharp divergence in the capacitance as V approaches $V_{c,1}$ [Eq. (3.35)], driven by a vanishing dipole-dipole repulsion at the smaller electrode. At finite temperature, this divergence is truncated by entropic effects, which inhibit the complete depletion of bound ions from the electrode surface. According to Eq. (3.60), for $S_1/S_2 \to 0$ the maximum is characterized by

$$f'''(n_1) = 0. \tag{3.63}$$

By Eq. (3.46), the corresponding capacitance $C = e^2 S_1 / f''(n_1)$.

At low temperatures $T < T_1$, the solution of Eq. (3.63) gives a capacitance

$$C_{max}(T) = \frac{0.32}{\alpha} \left(\frac{u_{im}}{k_BT} \right)^{1/3} \frac{\varepsilon S_1}{a}, \quad (T \ll T_1). \tag{3.64}$$

As in the symmetric case, this maximum occurs when n_1 declines sufficiently that $u_{dd}(n_1) \simeq k_BT$. In the limit that the temperature T approaches T_1, $C_{max} \simeq C(0,T)$, and there is no increase in capacitance at positive voltage.

At intermediate temperatures $T_1 < T < T_2$, the capacitance $C(V)$ at small voltages $|V| \ll k_BT/e$ is dominated by the two-dimensional entropy of ions bound to the metal surface S_1. As a consequence, the capacitance increases with negative voltage, where the density of ions n_1 increases and therefore their entropy declines. The capacitance continues to rise with negative voltage until $V \simeq -k_BT/e$, at which point the density of ions is large enough that the dipole-dipole repulsion $u_{dd}(n_1)$ is comparable to the

ideal gas free energy per ion $df_{id}(n_1)/dn_1$. At this point the capacitance achieves its maximum, which is again well-described by Eq. (3.64). Fig. 3.8 shows a characteristic set of C-V curves corresponding to this range of temperature.

At large temperatures $T > T_2$, the maximum capacitance becomes similar to the Helmholtz value $C_{H,1}$. The maximum occurs at large negative voltages $V < -k_BT/e < -V_{im}$, where the applied voltage is strong enough to collapse the ionic screening layer to the electrode surface and form a complete layer.

3.5.3 Comparison with ion-conducting glass experiment

Let us return to the case of a symmetric double-sided capacitor and compare our theory to the experiments of Ref. [21]. Capacitance-voltage characteristics for three different phosphosilicate glasses are shown in Fig. 1.5 together with our theoretical prediction for the relevant concentration $Na^3 = 0.1$ and temperature $T = 600$ K (heavy solid line). The theoretical curve is derived by a numerical minimization of the total free energy, as in Eq. (3.42), using $\varepsilon = 10$ for the bulk of the glass and $\varepsilon = 2.5$ for ions bound to the metal surface. This approximation is equivalent to using $\gamma = 4$. If one assumes a uniform dielectric constant ε, or $\gamma = 1$, then the theory predicts an even larger capacitance $C(0) \approx 3C_H$ (see Fig. 3.7), but it also predicts the capacitance to collapse at a smaller voltage than what is seen in experiment. To obtain better agreement with experiment one may need to consider the disorder potential acting on mobile ions in the glass, but this is outside the scope of the present work.

3.6 Monte Carlo Simulation

In order to test the analytic predictions of the previous sections, we present here the results of a simple Monte Carlo (MC) simulation that models the behavior of an ionic conductor between metal electrodes. As a computational convenience, we divide the system depicted in Fig. 1.3 into three slabs and disregard the thick neutral middle one, so that more computer time may be devoted to the anode and cathode sections in which interesting physics is occurring. This separation is in line with the above theory, which assumes that the two electrodes are separated by a distance much larger than any screening length scale, such that there is no interaction between the two electrodes'

double-layers.

Each remaining slab is treated as a square prism cell with volume $\Omega = L_x \times L_y \times L_z$, where $L_x = L_y$ and L_z is chosen so that the system is at least twice as thick as the depletion layer. The metallic electrode coincides with one of the cell's square faces. At $V = 0$, there is no difference between the two partial systems; each contains ΩN mobile positive ions, which are modeled as spheres with diameter $a = 2$Å that carry a charge e located at their center (the "primitive model"). These mobile ions are constrained to move on a cubic lattice with lattice constant a, placed so that $a/2$ is the distance of closest approach of an ion to the cell's walls. Mobile ions are subject to an excluded volume constraint, so that two of them cannot occupy the same site simultaneously. On this same lattice, at each of the $M_b = \Omega/a^3$ total lattice sites, there is a small fixed charge $-eNa^3$ which models the negative background. The MC program allows for Q/e ions to be taken from the anodic cell to the cathodic cell without changing the charge of the background. As we will see, this movement of Q/e ions is equivalent to applying a certain positive voltage V.

Every charge within a cell forms an electrostatic image in the metallic electrode surface ($z = 0$), *i.e.* a charge q at (x, y, z) has an image charge $-q$ located at $(x, y, -z)$. The total electrostatic energy $\mathcal{E}$ of the cell is calculated as 1/2 times the energy of a system twice as large composed of the real charges and their images, so that

$$\mathcal{E} = \frac{e^2}{4\varepsilon} \sum_{i,j;d_{ij}\neq 0}^{M_t} \frac{q_i q_j}{d_{ij}}. \tag{3.65}$$

Here, q_i denotes the charge of particle i, d_{ij} denotes the distance between particles i and j, and $M_t = 2(M_i + M_b)$ is the total number of particles in the system. For real mobile ions, $q_i = e$; for the mobile ions' images, $q_i = -e$; for the fixed background charges, $q_i = -eNa^3$; and for the images of the background charges, $q_i = eNa^3$. The dielectric constant is set to $\varepsilon = 5$ everywhere.

At the beginning of a MC simulation both the temperature T and the zero-voltage mobile ion density Na^3 are set. The positive ions are then initialized to random non-overlapping coordinates on the lattice and the initial energy is calculated from Eq. (3.65). After selecting an ion at random, the MC program attempts to reposition it to a random lattice site within a cubic volume of (4 Å)^3 centered on the ion's current position. For one in every 100 attempted moves the MC program expands this volume

to (20 Å)^3 in order to overcome the effects of any large, local energy barriers. The cell is given periodic boundaries, so that an ion exiting one face of the cell re-enters at the opposite face. The total electrostatic energy of the system, $\mathcal{E}$, is calculated after each attempted move. Moves are then accepted or rejected based on the standard Metropolis algorithm. To ensure thermalization, $8,000$ moves per mobile ion are attempted before any simulation data is collected. After thermalization, simulations attempt between 10^5 and 10^6 moves per mobile ion in the system, of which $\sim 10\% - 40\%$ are accepted.

In Fig. 3.5, the average ion density as function of the z coordinate is shown for a simulation of a $40 \times 40 \times 40$ Å^3 cell, with $T = 350K$ and $Na^3 = 0.01$. The accumulation of bound ions at the metal surface ($z = 1$Å) is clear, as is the depletion layer adjacent to it. As predicted, the system regains electroneutrality beyond the depletion layer, validating our assumption that the two double layers of the metallic electrodes can be simulated separately. The peaks in ion density at either edge of the neutral region likely correspond to over-charging by a strongly-correlated liquid of ions in the bulk [59, 22].

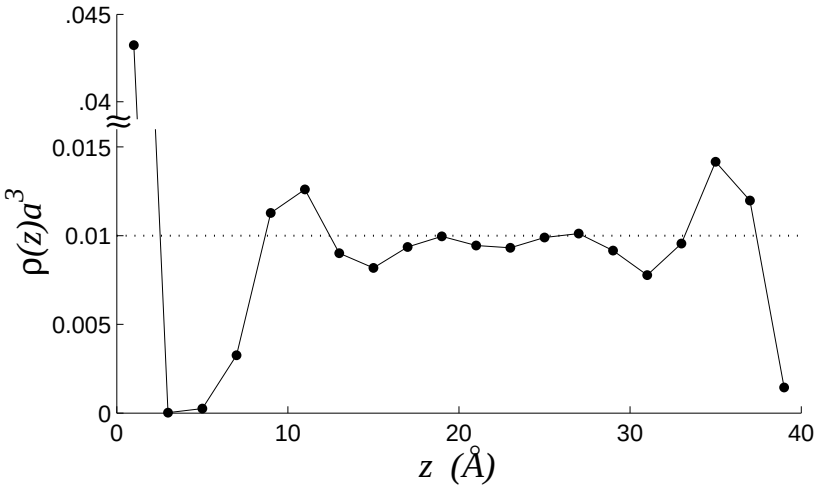

Figure 3.5: The average dimensionless ion density ρa^3 as a function of the distance z from the metal surface, as calculated from a MC simulation of a $40 \times 40 \times 40$ Å^3 cell at $Q = 0$. The dotted line shows the concentration which neutralizes the negative background.

The primary goal of the simulation is to obtain the full system's capacitance, $C = dQ/dV$. A change in voltage in the real system requires charge transfer, Q, from one

electrode to the other through the voltage source. In our simulation we apply a constant voltage $V \geq 0$ to the pair of cells by adding Q/e ions to one cell (cathodic side) and removing Q/e ions from the other cell (anodic side). In this way the electronic charge of each electrode is varied; the addition of Q/e ions to a cell corresponds to an addition of a charge $-Q$ to the electrode, which comes in the form of image charges for the added ions. The voltage that corresponds to this movement of charge is found through $V = d\mathcal{F}/dQ$, where $\mathcal{F} = F_a + F_c$ is the free energy of the full system, equal to the the sum of the anodic and cathodic free energies. In a given cell containing M_i positive ions, we used the Widom particle insertion method [60, 61] to obtain the change in either the anodic or cathodic cell's free energy $\Delta F_{a,c}$ caused by the addition of another positive ion,

$$\frac{\Delta F_{a,c}}{k_B T} = \ln\left(\rho(x,y,z)a^3/\langle \exp[-\Delta\mathcal{E}(x,y,z)/(k_B T)]\rangle\right). \tag{3.66}$$

Here, $\Delta\mathcal{E}(x,y,z)$ is the change in electrostatic energy due to a probe charge placed at (x,y,z) and $\rho(x,y,z)$ is the mean density of real positive ions at (x,y,z). The angle brackets denote a time average and the ratio of the quantities inside the natural log is independent of the position (x,y,z). At the beginning of the simulation, 20 lattice sites are selected as Widom insertion sites at which the quantities $\rho(x,y,z)$ and $\exp[-\Delta\mathcal{E}(x,y,z)/(k_B T)]$ are calculated after every attempted move. The corresponding values of $\Delta F_{a,c}$ obtained from each insertion site are averaged in order to give a final value.

We are free to set the free energy of the system at $Q = 0$ to zero, so that $\mathcal{F}(0) = 0$. Simulating the anode and cathode for $Q = 1, 2, 3...$, while employing the Widom insertion method, allowed us to determine the system's free energy as a function of Q,

$$\mathcal{F}(Q) = \mathcal{F}(Q-1) + \Delta F_c(Q) - \Delta F_a(Q). \tag{3.67}$$

This equation must be used iteratively to find $\mathcal{F}(Q-1)$ starting from $\mathcal{F}(0) = 0$. For the symmetric case ($S_1 = S_2$), this process is easily extended to negative voltages by taking $Q < 0$; positive ions are then attracted to the anode and repelled from the cathode. In the asymmetric case ($S1 < S2$), $\Delta F_c(Q) = \Delta F_a(-QS_1/S_2)$, so we need only to simulate the cathodic cell at positive and negative Q in order to calculate $\Delta F_a(Q)$ and $\mathcal{F}(Q)$.

Taking the discrete derivative of these data points gives $\mathcal{F}(Q) - \mathcal{F}(Q-e) = V(Q-$

$e/2$). Another derivative gives the capacitance of the system as a function of V,

$$C(V(Q)) = \frac{dQ}{dV} = \frac{e}{(V(Q+e/2) - V(Q-e/2))}, \tag{3.68}$$

where $V(Q) = [V(Q+e/2) + V(Q-e/2)]/2$.

Figure 3.6 shows the results of the simulation for a system with $S1 = S2 = 40 \times 40$ Å^2, $L_z = 20$Å, and $Na^3 = 0.01$. Capacitance as a function of voltage is shown for three values of the temperature, along with the analytic predictions explained in section 3.5. These temperatures fall within the range $T_1 \lesssim T < T_2$, and as predicted, the maximum capacitance occurs at zero voltage while the capacitance collapse is smeared over a voltage range proportional to $k_B T/e$.

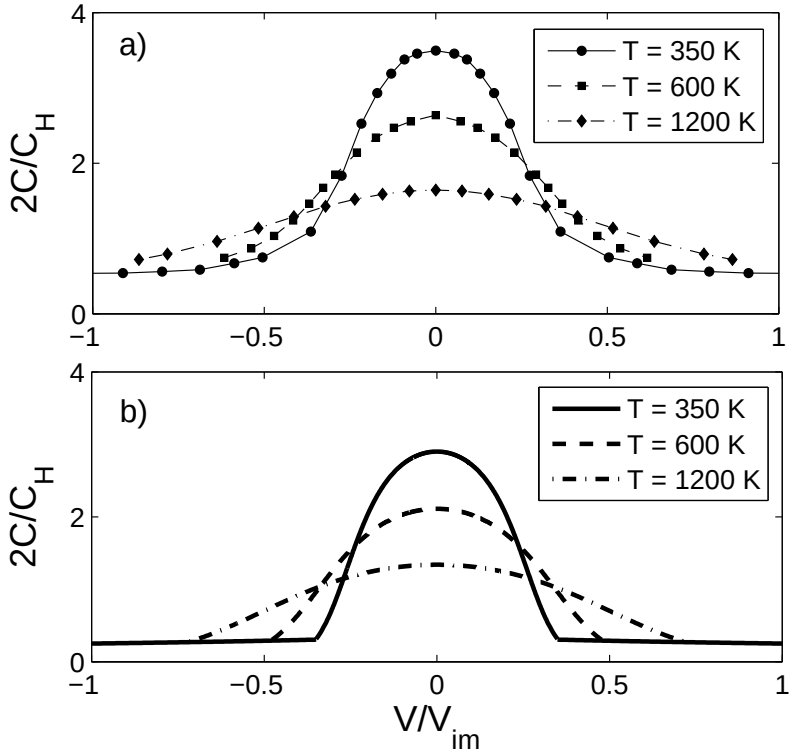

Figure 3.6: Capacitance as a function of voltage for a symmetric parallel-plate capacitor at various temperatures $T_1 \lesssim T < T_2$, using $Na^3 = 0.01$, $\varepsilon = 5$, and $\gamma = 1$. a) Results from a Monte Carlo simulation of the OCP model. Error bars for the MC data are smaller than the symbols. b) Analytic predictions, as explained in section 3.5.

In order to quantify the finite-size effects of our simulation cell, we examined the capacitance at zero voltage, $C(0,T)$, obtained from three "slab-shaped" simulation volumes of size $L \times L \times L/2$, with $L = 40$, 60, and 80 Å. For $Na^3 = 0.01$, $C(0,T)$ was seen to scale linearly with $1/L$ at all values of the temperature that we examined ($T =$ 350, 600, and 1200 K). In each case, the value of $C(0,T)$ obtained by extrapolation to infinite system size was within 16% of the value of $C(0,T)$ corresponding to $L = 40$ Å. This difference was within the uncertainty of our simulation for all temperatures except 1200 K. We also checked that there was no dependence of the capacitance on the aspect ratio of our simulation cell by examining $C(0,T)$ in three cubic cells with side length $L = 20$, 40, and 60 Å. The resulting value of $C(0,T)$ again scaled linearly with $1/L$ and, within uncertainty, the extrapolated values of $C(0,T)$ agreed with those found in the slab geometry. These results allow us to conclude that the $40 \times 40 \times 20$ Å simulation cell provides a good approximation of an infinite system. All MC results presented below correspond to this choice.

The temperatures explored by our MC simulation fall in the intermediate temperature range $T_1 \lesssim T < T_2$, and so the capacitance should be described by Eq. (3.55). Indeed, as shown in Fig. 3.7, the temperature dependence of $C(0,T)$ obtained from simulations is in good agreement with the analytical prediction of Eq. (3.55). Results from a numerical minimization of the total free energy [Eq. (3.42)] are also shown. Results are plotted as a function of absolute temperature as well as dimensionless temperature $T^* = k_B T/(e^2/\varepsilon a)$.

Unfortunately, the low-temperature predictions of our theory, corresponding to $T \ll T_1$, could be not be examined directly since these temperatures correspond to an extremely low acceptance rate in our MC simulation. Nonetheless, we can get an idea of the zero-temperature capacitance by examining the behavior of the total electrostatic energy $\mathcal{E}$. Since at zero temperature the total free energy becomes equal to $\mathcal{E}$, the capacitance C approaches $(d^2\mathcal{E}/dQ^2)^{-1}$ at low temperatures. Examining $(d^2\mathcal{E}/dQ^2)^{-1}$ as a function of temperature and extrapolating to $T = 0$ allows us to make a rough estimate of the zero-temperature capacitance $C(0,0)$. For $Na^3 = 0.01$, the result is $2C(0,0)/C_H \approx 7$, which is significantly higher than the theoretical prediction of $2C(0,0)/C_H = 4.5$ given by Eq. (3.16). This enhanced capacitance may be the result of screening of the dipole interaction by mobile ions in the bulk, which suppresses the interaction of distant dipoles

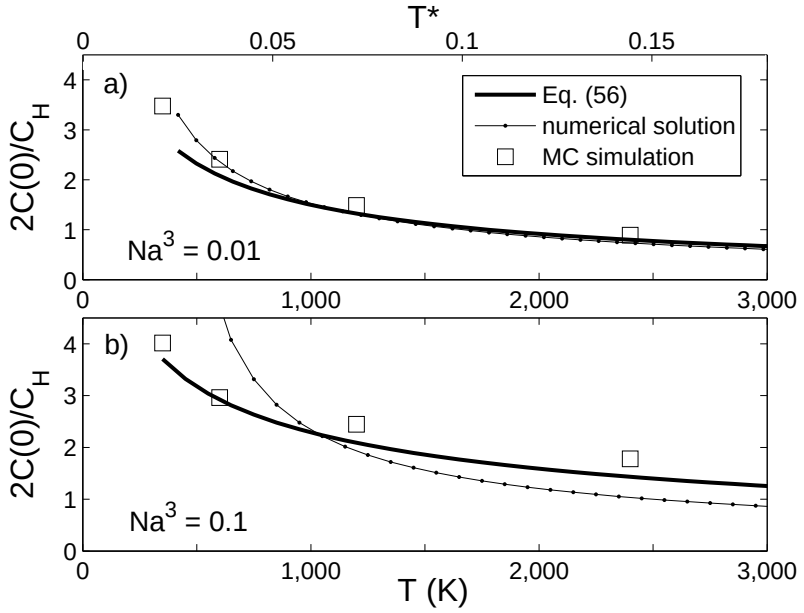

Figure 3.7: Capacitance at zero voltage, $C(0,T)$, as a function of temperature for a symmetric system $S_1 = S_2$ at two different values of the density Na^3. Squares represent the MC data using $S = 40 \times 40\text{Å}^2$, while the prediction of Eq. (3.55) is shown by the thick black curve. Results are plotted as a function of absolute temperature (lower axis) as well as dimensionless temperature $T^* = k_B T/(e^2/\varepsilon a)$ (upper axis). The error bars for the MC data are smaller than the symbols. a) $Na^3 = 0.01$. b) $Na^3 = 0.1$.

and therefore reduces the effective value of α. At larger ion density, the discrepancy between our low-temperature theory and the projected zero-temperature capacitance from simulation becomes even more pronounced. For $Na^3 = 0.03, 0.1, 0.3$ we estimate $2C(0,0)/C_H = 6.5 \pm 1$, as compared to $2C(0,0)/C_H = 3.5, 2.5, 2.0$ given by Eq. (3.16). These results are consistent with the interpretation based on screening of dipole-dipole repulsion by ions of the bulk. Indeed, at larger ion densities the bulk becomes more effective at screening because it is separated from the metal surface by a thinner depletion layer.

As a rudimentary test of the extent to which the dipole interaction is screened by bulk ions, we performed a MC simulation of a $40 \times 40 \times 20$ Å^3 simulation cell in which one of the ions was fixed to the center of the metal surface ($x = y = 0$, $z = a/2$). The time-averaged density of ions $\rho(x,y,z)$ was then recorded at every lattice site in the simulation cell, from which the mean electric potential $\phi(x,y,z = a/2)$ at the metal

surface could be reconstructed. In order to isolate the contribution of bulk ions to the potential from that of strongly-correlated ions on the metal surface, the simulation was run with $n_0 S$ ions removed from the system. In this way we simulated the anodic side of a capacitor at $V = V_c$, where the metal surface is depleted of bound ions. At a density corresponding to $Na^3 = 0.01$ and a temperature $T = 350$ K, we found that the potential ϕ surrounding the ion was well described by $\phi(r, z = a/2) = ea^2/2\varepsilon r^3 \cdot \exp(-r/r_{sb})$, where $r = \sqrt{x^2 + y^2}$ is the azimuthal distance from the bound ion and r_{sb} is a length scale which characterizes the range of the screened dipole potential. We found $r_s \approx 4.5a$, which is smaller than the average distance $n_0^{-1/2} \approx 6a$ between bound ions at zero voltage. If this expression $e\phi(n^{-1/2})$ is substituted for the dipole-dipole energy u_{dd}, then the resulting prediction for zero-voltage capacitance at $Na^3 = 0.01$ is significantly enhanced: $2C(0)/C_H = 12$ as compared to 4.5 from Eq. (3.16). In reality, the observed capacitance from MC simulations is between these two values, $2C(0)/C_H \approx 7$, and this discrepancy may be the result of a non-additive response of bulk charges to dipoles at the surface (non-linear screening).

Finally, we also considered the simulation of a highly asymmetric capacitor, where S_2 is infinite and $S1 = 40 \times 40$ Å^2. We again examine the case $Na^3 = 0.01$, $T = 600$K, and use $L_z = 20$ Å. The results are shown in Fig. 3.8, along with the analytic predictions of section 3.5 for different values of the temperature.

3.7 Low-voltage capacitance peak in asymmetric ionic liquids

Up to this point we have discussed the OCP model primarily as it applies to ion-conducting glasses at moderately high temperatures where only the smallest ion (cation) is mobile. Qualitative agreement of our predictions with experimental data shows that the OCP model is a reasonable zero-order approximation.

In this section we discuss other possible applications of the OCP model, as mentioned in the introduction. One application which immediately comes to mind is to super-ionic crystals, where only the smallest positive ionic species (such as Na^+ or Li^+) is mobile. In this case there is no reason for a frozen disorder, so that in super-ionic crystals the OCP model should work even better than in ion-conducting glasses.

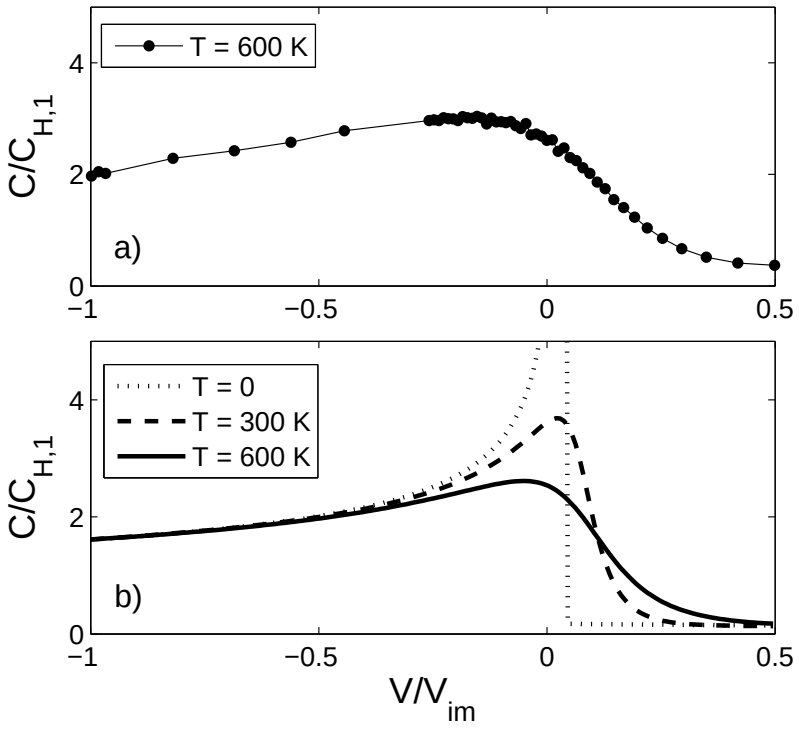

Figure 3.8: The capacitance of a highly asymmetric capacitor, $S_2/S_1 \to \infty$, where only surface 1 determines the capacitance. a) Results from a MC simulation. Error bars are smaller than the symbols. b) Analytic predictions for various temperatures, as explained in section 3.5. Note that the capacitance diverges at $T \to 0$. Compare these results to those of the OCP model in Fig. 2.4

Perhaps more interesting is the application to ionic liquids, which have recently attracted considerable attention [12, 62, 41, 63]. In ionic liquids, both positive and negative ions are mobile. In order to get spontaneous polarization near the electrodes at zero voltage, and thereby obtain the low-voltage peak in capacitance predicted by the OCP model, one should consider a strongly asymmetric ionic liquid.

We begin by considering ionic liquids composed of monovalent cations, which we model as rigid spheres with diameter a, and much larger monovalent anions, modeled by rigid spheres with diameter $A \gg a$. For example, one may have in mind the ionic liquid made of Na^+ cations and large non-coordinating anions such as the "BARF" anion ($[B[3,5-(CF_3)_2C_6H_3]_4]^-$) [64]. In such a liquid anions fill most of the space and form

a weakly-compressible negative background. The maximum energy of attraction of the anion to its image in the metal surface, $e^2/2\varepsilon A$, is much smaller than the corresponding image attraction $e^2/2\varepsilon a$ for a cation. Because of their small size, cations easily move between anions. The cations are strongly attracted to the metal plates and therefore rearrange themselves to form the EDL. Thus, we may assume that anions form an analog of the negative background in the OCP model. The maximum density of such a background is approximately $1/A^3$. Thus, we can expect that the capacitance $C(V,T)$ is similar to what we predict in the OPC model, if for N we use $N \sim 1/A^3$, or in other words $Na^3 \to (a/A)^3$. For example, if $A/a = 100^{1/3} = 4.6$ we should get a capacitance $C(0,T)$ similar to the case $Na^3 = 0.01$ studied above for the OCP model.

In order to verify these predictions, we ran MC simulations of the primitive hard sphere model of an ionic liquid between equal-sized metallic electrodes. In these simulations, monovalent cations and anions are given a diameter a and A, respectively, and placed with a particular volume density N in a square prism simulation cell with volume $\Omega = L \times L \times L/2$. The electrode surface is again chosen to coincide with the $z = 0$ plane, so that an ion of charge $q = \pm e$ whose center is at position (x, y, z) has an image charge $-q$ at $(x, y, -z)$. The voltage of the electrode is varied by changing the number of cations M_c in the system, as in simulations of the OCP model, while the number of anions $M_a = \Omega N$ remains constant. The corresponding electronic charge in the electrode is $Q = e(M_a - M_c)$ and the capacitance dQ/dV can be determined from the resulting voltage. A very similar simulation method was used by previous authors [40, 65] to examine the capacitance of ionic liquids, but the effect of asymmetric ion size was not explored.

Since in this case anions are mobile, unlike in the OCP model, a change in voltage should correspond to a changing number of anions as well as cations in the vicinity of the metal surface. Therefore, one may object to our method of modifying the charge of the electrode by changing only the number of cations in the system. For example, one may imagine inducing a charge $Q = -2e$ in the electrode by democratically adding one cation and removing one anion from the simulation cell rather than by adding two cations. The difference between these two methods, however, is only an infinitesimal change in the bulk ion densities of the simulation cell; the physics of the metal interface is not affected. To ensure that the capacitance in our simulation is independent of the

method of charge transfer, we repeated all of our simulations using both a method where the charge Q is modified by changing only the number of anions M_a and a method where M_a and M_b are changed simultaneously by equal and opposite amounts. No noticeable change was observed to any of the results presented below.

The microscopic rules of the simulation are identical to those of the OCP model, except that ions are not constrained to move on a lattice and there is no fixed negative background. The energy of a particular configuration of ions is also identically calculated, with the exception that the hard-core repulsion between ions should be added explicitly to Eq. (3.65). That is,

$$\mathcal{E} = \frac{1}{4}\sum_{i,j}^{M_t} u(d_{i,j}), \tag{3.69}$$

where $M_t = 2(M_a + M_c)$ is the total number of charges in the system (ions plus images), and the two-particle interaction energy $u(d_{i,j})$ is

$$u(d_{i,j}) = \begin{cases} \infty, & d_{i,j} < (D_i + D_j)/2 \\ q_i q_j / \varepsilon d_{ij}, & d_{i,j} > (D_i + D_j)/2 \end{cases}. \tag{3.70}$$

Here, D_i denotes the diameter of ion i; $D_i = a$ for cations and $D_i = A$ for anions.

In addition to the method of Eq. (3.68) for calculating capacitance, where the voltage is inferred from the change in free energy of the system, for these simulations we used a method where the voltage is measured directly for a given value of Q, so that determination of the free energy is unnecessary for calculating capacitance. The voltage is measured by defining a "measurement volume" near the back of the simulation cell — occupying the range $-L/4 < x < L/4$, $-L/4 < y < L/4$, $L/4 < z < 3L/8$ — inside of which the electric potential is measured. After performing thermalization of the initial random configuration (50,000 moves per mobile ion), the total electric potential $\phi(x, y, z)$ is measured at 500 equally-spaced points within the measurement volume after every $3(M_a + M_c)$ attempted moves. These measured values of potential are then averaged both temporally and spatially to produce a value for the electric potential $\bar{\phi}(Q)$ of the electrode relative to the bulk. The corresponding voltage between the two electrodes is $V = \bar{\phi}(Q) - \bar{\phi}(-Q)$, and the capacitance is determined from the discrete derivative $\Delta Q/\Delta V$. The results produced by this second method were compared with

those produced by the method of the previous section for four different sets of simulation parameters, and the results were indiscriminable. Below we present results from only the second, more time effective method.

Figure 3.9 shows the resulting capacitance for ion liquids with asymmetry $A/a = 4$ and $A/a = 2$ at various temperatures. Here the temperature is presented in dimensionless units $T^* = k_B T/(e^2/\varepsilon a)$ in order to facilitate comparisons with literature [65, 40, 66]. Our simulations use the same values for the cation size and dielectric constant as in the OCP case, $a = 2$ Å and $\varepsilon = 5$, so that the temperature scale $e^2/\varepsilon a k_B \approx 16700$ K and the range of data $0.02 < T^* < 0.18$ corresponds to 350 K $\leq T \leq$ 3000 K. For a more typical value of the cation diameter $a \sim 8$ Å, this range corresponds to 100 K $\lesssim T \lesssim$ 750 K. The size of the simulation cell for the $A/a = 4$ case was $L = 80$ Å, and in the case $A/a = 2$ we used $L = 40$ Å. The dimensionless ion density $\rho_b^* = M_a(a^3 + A^3)/\Omega$ was $\rho_b^* = 0.5$. An examination of finite size effects, as in the previous section, suggests that our results for capacitance are accurate to within 18%. As predicted above, our numerical results for ionic liquids with $A/a = 4$ and 2 are close to the results for the OCP model with $Na^3 = 0.01$ and 0.1, respectively.

While Fig. 3.9 shows the capacitance of the two-electrode system, the capacitance of a single interface can also be easily determined from our MC simulations by looking at the derivative $d\bar{\phi}/dQ$. As an example, Fig. 2.4 shows this capacitance as a function of dimensionless voltage V/V_{im} for the case $A/a = 2$ at a temperature $T^* = 0.036$ and density $\rho_b^* = 0.5$. The asymmetry in capacitance with voltage is similar to what we observed in the OCP model (Fig. 3.8).

Thus far we have focused on the effects of asymmetric ion size, but we note that there is another way to make a strongly asymmetric ion liquid. Namely, cations and anions may have the same radius a but different absolute values of charge. One can imagine, for example, that cations are multivalent and have charge $+Ze$ while anions have charge $-e$. In this case cations are much more strongly attracted to their $-Ze$ images, so that together they again create a dipole layer on the surface of the metal. Because there are Z anions per one cation, anions form a thicker negatively-charged layer centered farther from the metal surface than the cations. This anion layer is analogous to the depletion layer of in the OCP theory, with a dimensionless concentration of cations $Na^3 \sim 1/(Z+1)$. In order to estimate the capacitance, we can use the results of the

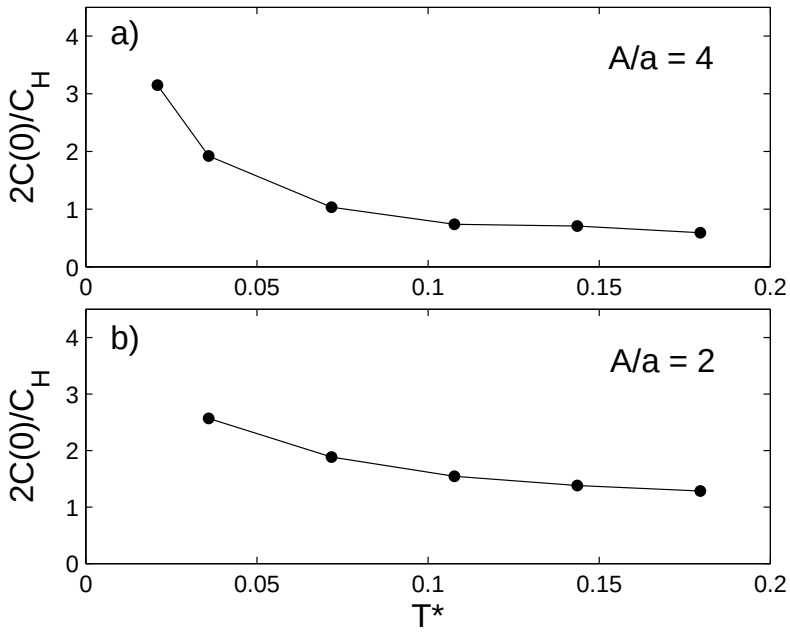

Figure 3.9: The capacitance of a primitive model ionic liquid between metallic electrodes as a function of temperature. The density of ions in each case is $\rho_b^* = 0.5$. Error bars are smaller than the symbols. a) $A/a = 4$. b) $A/a = 2$. Compare these results to those of the OCP model in Fig. 3.7

. .

OCP model with $Na^3 \to 1/(Z+1)$.

This prediction can be checked by our MC methods by simulating an ionic liquid with trivalent cations ($Z = 3$) and a neutralizing concentration of monovalent anions, both with the same diameter a. We consider the case where the dimensionless temperature, normalized to the larger charge of the cation, is $T^* = k_B T/(Z^2 e^2/\varepsilon a) = 0.11$ and the density is $\rho_b^* = 0.5$. The resulting capacitance is shown in Fig. 3.10 as a function of the dimensionless voltage V/V_{im}, where $V_{im} = Ze/2\varepsilon a$. The C-V curve is again very similar to that of the OCP model, with a maximum $C/C_H > 1$ and a smaller capacitance at positive voltage, where Z-ions are depleted from the electrode surface.

Even closer imitation of the OCP model can likely be obtained by combining a large charge asymmetry $Z \gg 1$ with a large asymmetry of ion size $A/a \gg 1$.

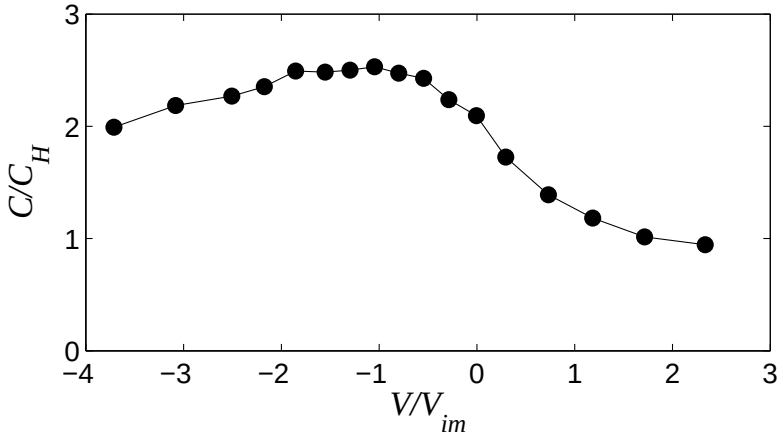

Figure 3.10: The capacitance of a single metal/ionic liquid interface as a function of voltage for an ionic liquid with trivalent cations and monovalent anions with equal diameter. The dimensionless temperature $T^* = k_BT/(Z^2e^2/\varepsilon a) = 0.11$ and the density is $\rho_b^* = 0.5$. Error bars are smaller than the symbols. Compare these results to those of the OCP model in Fig. 3.8.

3.8 Aqueous solution of a Z:1 salt

Another system for which the OCP model gives a zero-order approximation is that of an aqueous solution of a salt with multivalent cations with charge Ze ("Z-ions") and monovalent anions, for example $LaCl_3$. In such a solution Z-ions are strongly attracted to their $-Ze$ images in the metal electrode and so a number of them form compact dipoles at the interface. On the other hand, attraction of anions to their images is much weaker, so that at room temperature they do not form dipoles but rather stay in the solution and effectively form a negative OCP model background with charge density $-eZN$, where N is the concentration of salt. If we again use the theory of Sec. 3.3 to balance the depletion layer energy with the energy of Z-ions condensed on the metal surface, we arrive at Eq. (3.11) for the surface concentration n_0 of Z-ions. Remarkably, both n_0 and the capacitance at $T = V = 0$ do not depend on Z (one can guess this from the fact that the corresponding results in section 3.3 do not depend on the elementary charge e).

For $LaCl_3$ we can examine the case where $N = 0.5$ M when the salt is totally dissociated. This concentration corresponds to $Na^3 \sim 0.1$, if for the diameter of the

hydrated La^{+3} ion we use $a = 6$ Å. Thus, it is tempting to apply to this case the above finite temperature calculations of capacitance for $Na^3 = 0.1$.

One may worry, however, that the depletion layer, where the concentration of La^{+3} ions vanishes, is not uniformly charged by Cl^- ions with their average density $-3eN$. This may happen because the positive potential ϕ_s near the surface of the metal, which develops to balance the image attraction of Z-ions to the metal, is much larger than k_BT/e and therefore results in the exponential growth of Cl^- concentration near the metal surface. For the surface potential we get $Ze\phi_s = Z^2e^2/2\varepsilon a - k_BT\ln(na^2/Na^3)$, where the second term comes from the entropy that a Z-ion loses at the surface in comparison with the bulk solution. For $LaCl_3$, using $a = 6$ Å, $\varepsilon = 80$, $T = 300$ K, and $Na^3 = 0.1$, we get that $Z^2e^2/2\varepsilon a = 5.3k_BT$ and $\ln(n_0a^2/Na^3) < 1$, and therefore, $e\phi_s$ is equal to only $1.7k_BT$. This allows us to ignore (as a zero-order approximation) the non-uniformity of the concentration of Cl^- in the depletion layer. Then we can use the temperature-dependent results we obtained for the OCP model in Section 3.5. Applying these results requires only the scaling of the temperature in units of $Z^2e^2/\varepsilon a$. For $LaCl_3$, using $\varepsilon = 80$ and $a = 6$ Å, we find that the temperature unit $Z^2e^2/\varepsilon a$ is 0.37 of that for glass (where $Z = 1$, $\varepsilon = 5$, and $a = 2$ Å). Thus, for $N \sim 0.5$ M at $T = 300$ K we arrive at the same ratio $C(0)/C_H = 2.5$ for the capacitance of a single interface as for the OCP model with $Na^3 = 0.1$ at $T = 800$ K (Fig. 3.7b).

This prediction can be checked by running a MC simulation identical to the one described in the previous section. Fig. 3.11 shows the resulting capacitance per unit area C/S of a single interface as a function of voltage for the salt concentrations $N = 0.5$ M and $N = 1.5$ M, using the temperature $T = 300$ K and the estimated hydrated diameters $a = 6$ Å and $A = 4$ Å for La^{+3} and Cl^-, respectively. The simulation cell is given a size $L = 100$ Å. For $N = 0.5$ M and 1.5 M, the maximum capacitance is larger than the Helmholtz value by 2.0 and 2.3 times, respectively. The data presented in Fig. 3.11 corresponds to the range of electrode charge $|\Delta Q| < ZeN\Omega/2$, where $ZeN\Omega$ represents the total cation charge in the simulation volume. Restricting our simulation to this range ensures that the bulk ion concentration is not changed significantly by the addition/removal of Z-ions to the cell that is associated with finite voltage.

The results of Fig. 3.11 are qualitatively similar to those of the OCP model given in Fig. 3.8. The capacitance is asymmetric with respect to voltage, acquiring a larger value

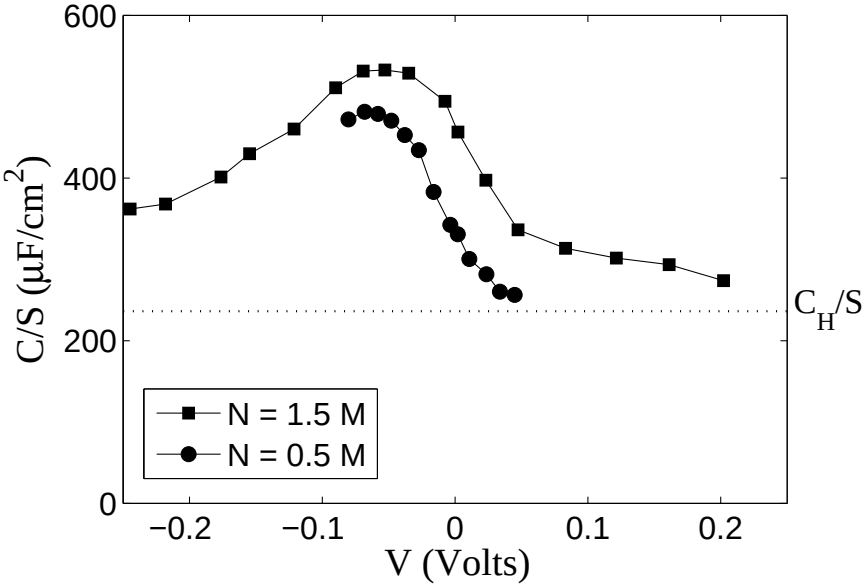

Figure 3.11: The capacitance per unit area C/S of an aqueous solution of $LaCl_3$ at a metal electrode, as determined by our MC simulation using the primitive hard sphere model. The La^{+3} cation has a hydrated diameter $a = 6$ Å, while the Cl^- anion has a diameter $A = 4$ Å. The temperature is $T = 300$ K and the uniform dielectric constant $\varepsilon = 80$. Error bars are smaller than the symbol size. The dotted line shows the Helmholtz value $C_H/S \approx 236$ μF/cm^2. Compare these results to those of the OCP model in Fig. 3.8.

at negative voltages where Z-ions accumulate at the metal surface and bind strongly to their image charges. At positive voltages, Z-ions are depleted from the electrode surface and the capacitance collapses. At large positive voltages $V \gg k_BT/e \approx 26$ mV, negative anions become strongly bound to the electrode by the applied voltage and they approach complete filling of an ionic layer. In this limit the capacitance approaches $\varepsilon/2\pi A = C_H \cdot a/A$.

3.9 Summary and applications to pseudo-capacitance

In this Chapter we have presented a theory to explain how the capacitance of the metal/ionic conductor interface can be significantly larger than the Helmholtz capacitance C_H. In other words, we have shown how the apparent thickness of the double layer

d^* can be smaller than the ion radius. This surprising conclusion is obtained by abandoning the mean-field approximation and considering instead the behavior of discrete charges next to the metal surface. While mean field theories cannot explain how d^* can be smaller than the physical separation between the electrode and its countercharge, we have shown that very large capacitance is a natural result for an EDL composed of discrete, correlated ions. We have worked within the approximation of a "one-component plasma" model, where only one species of ion is mobile, and described its behavior over the full range of temperature. We have further argued that our results can be easily extended to strongly asymmetric ionic liquids. A simple Monte Carlo simulation confirms our analytical predictions at realistic temperatures. At very low temperatures, the EDL capacitance is limited only by the weak repulsion between ion-image dipoles at the metal surface, which for a single interface produces a sharp capacitance peak that diverges as $T^{-1/3}$.

Qualitatively, our theory explains all the main features of the experiment in Ref. [21]. The authors of Ref. [21] relate their observations to theories of so-called "pseudo-capacitance", a term used by Conway and coworkers for the rare cases of anomalously large EDL capacitance (see [49] and references therein). Pseudo-capacitance is said to result from specific adsorption of cations to the metal surface, where the cations are neutralized. In this sense Conway's theory is similar to ours. However, his theory of pseudo-capacitance does not explain what happens with the negative charge of excess anions, which remains in the bulk and which in our theory plays a pivotal role. The existing theory of pseudo-capacitance also does not explicitly specify the form of the repulsion between bound ions, and therefore does not arrive at a closed result. We take care to address both of these points in the present (OCP) model, and we arrive at definite predictions for capacitance. Thus, one may consider our theory to be an improved theory of pseudo-capacitance, if by this term one understands a capacitance larger than the Helmholtz value. We emphasize, however, that our theory does not assume any Faradaic effects, so that our result is in fact a standard capacitance and the prefix "pseudo-" is unnecessary.

Chapter 4

Non-mean-field screening by multivalent counterions

Theoretical and experimental studies of highly charged, insulating, macro-ions in electrolyte solutions have predicted [67, 68, 69, 70] and demonstrated [71, 72, 73, 74] the existence of charge inversion, the result of oppositely charged counter ions over compensating the original charge of the macro-ion on which they condense, effectively reversing the sign of the macro-ion. If the multivalent ions have a binding energy greater than k_BT, charge inversion is observable through electrophoresis [70, 74]. Charge inversion may have applications in gene therapy where the goal is to introduce a new piece of DNA into a cell's nucleus [75, 76, 77]. This process is complicated by both the cell's membrane and the new DNA carrying a negative charge. The ability to manipulate the DNA's net charge through charge inversion could reduce the difficulty associated with the repulsive force between DNA and the cell membrane.

This chapter focuses on the concentration of ions as a function of distance form the macro-ion, rather than on the capacitance of the interface. Even though there is not an explicit metallic surface in the system, image charges and lateral correlations still manage to play a central role in determining the distribution of ions and can be used to explain the origin of charge inversion.

4.1 How is a highly charged macro-ion screened by multivalent counterions?

It is possible for many materials to play the role of the macro-ion [78]. The charged surface of mica, colloidal particles, DNA, and lipid membranes are just a few of the macro-ions suitable for charge inversion that also have importance in chemistry and biology. Counterion candidates are just as numerous, from multivalent metal ions, such as La^{+3} in $LaCl_3$, and charged micelles, to small colloidal particles and dendrimers. These multivalent counterions, each with charge Ze are referred to as Z-ions for convenience.

The fundamental aspects of screening are illustrated by considering the simple geometry of a solid occupying the half space $x \leq 0$, whose surface at $x = 0$ has a large uniform surface charge density $-\sigma$. The surface charge is screened by an aqueous solution of positive, spherical Z-ions with radius a, which occupies the rest of space $x > 0$ (see Fig. 4.2). Both the macroion and the aqueous solution have dielectric constant $\varepsilon \simeq 80$. If all of the Z-ions were to condense on the macro-ion's surface, their total charge per unit area would equal σ. In such a neutral system, the concentration of Z-ions $N(x) \to 0$ at $x \to \infty$. The main goal of this chapter is to discuss the behavior of $N(x)$. The solution of the Poisson-Boltzmann (PB) equation for this problem has been known for nearly a century [13, 14]. The Gouy-Chapman solution is

$$N(x) = \frac{1}{2\pi Z^2 l_B} \frac{1}{(\lambda + x - a)^2}, \tag{4.1}$$

where $\lambda = e/2\pi\sigma l_B Z$ is the Gouy-Chapman length, and $l_B = e^2/(\varepsilon k_B T) \simeq 0.71$ nm is the Bjerrum length. We have modified the standard Gouy-Chapman formula, taking into account the finite radius of the Z-ions, which can not approach the surface closer than $x = a$.

It was shown [67, 22, 78, 79, 73, 80, 69, 72, 81] that the Gouy-Chapman solution fails when both σ and Z are large enough. The reason it fails is that, in addition to λ, there is a second length scale in the problem due to the discreteness of charge. When the condensed Z-ions neutralize the charge of the plane, the two-dimensional concentration of Z-ions is $n = \sigma/Ze$, and the surface area per ion, the Wigner-Seitz cell, can be approximated as a disc of radius b such that $\pi b^2 = 1/n$. Thus, $b = (\pi n)^{-1/2} = (Ze/\pi\sigma)^{1/2}$ and $2b$ is approximately the distance between Z-ions. We can construct the

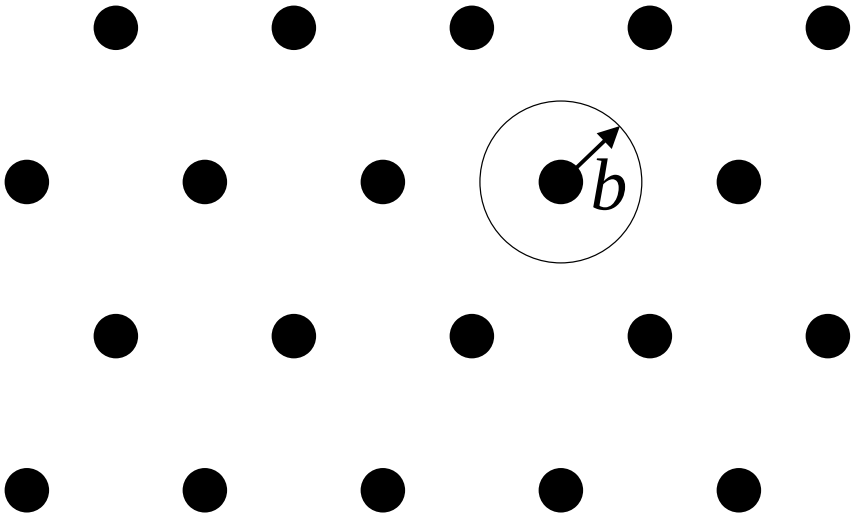

Figure 4.1: Z-ions form a two-dimensional Wigner Crystal on the uniformly charged background of the macro-ion's surface when the Coulomb interaction among Z-ions dominates the influence of thermal motion at the surface. The hexagonal Wigner-Seitz cell is approximated as a disc of radius b.

dimensionless ratio

$$\frac{b}{\lambda} = 2\Gamma \ , \quad \Gamma = \frac{Z^2 e^2/\varepsilon b}{k_B T} \ . \tag{4.2}$$

Here Γ is the dimensionless Coulomb coupling constant, or the inverse dimensionless temperature measured in the units of a typical interaction energy between Z-ions. For example, at $Z = 3$ and DNA like $\sigma = 0.95e$ nm^{-2} used in this Chapter , we get $\Gamma = 6.4$, $\lambda \simeq 0.79$ nm and $b \simeq 1.0$ nm. Thus, the Coulomb repulsion energy of the Z-ions dominates the thermal energy. The result is a strongly correlated liquid, which has short-range order similar to a Wigner crystal [67, 22, 78, 79, 73, 80, 69, 72, 81, 82, 83, 84, 70] and is located, practically, at the very surface of the macroion. This Chapter deals only with the strong coupling case: $\Gamma \gg 1$. Another definition for a Coulomb coupling parameter, $\Xi = 2\Gamma^2$, was introduced in [69], and of course, in the limit $\Gamma \gg 1$, $\Xi \gg 1$ as well. It should be stressed that this failure of Gouy-Chapman is not caused by ignoring image charges as it was in Chapters 2 and 3, but rather the failure occurs because of lateral correlations, which are ignored by mean-field theories.

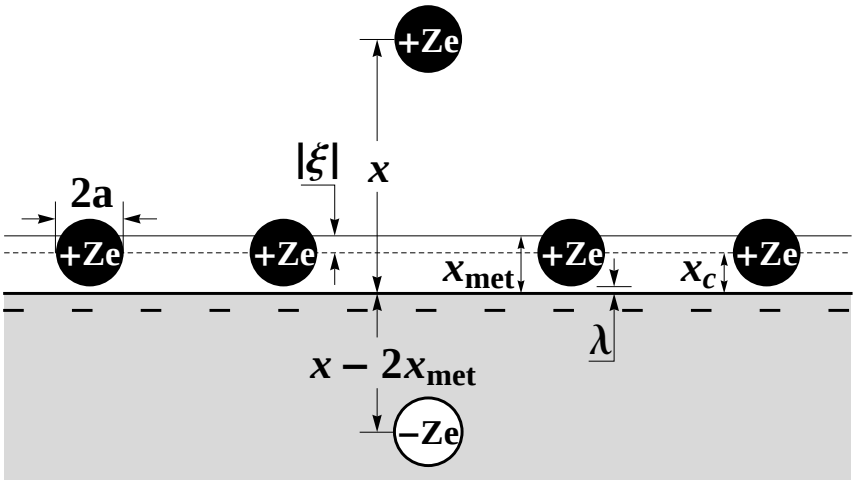

Figure 4.2: A stray positive Z-ion (elevated black sphere) at a distance x from the surface (thick line) of a negatively charged planar macroion (shaded region). Other Z-ion (black spheres), condensed at the surface are on average a distance λ above the macro-ion's surface. The dashed line indicates the average distance, $x_c = a+\lambda$, from the macro-ion's surface to the adsorbed Z-ions' centers. The stray Z-ion and its negative image charge (white sphere) are equidistant from the effective metallic surface, which is shown by the thin line at $x_met = x_c + |\xi|$.

4.2 The image charge returns

Mean-field treatments, along the lines of PB theory, fail at $\Gamma \gg 1$, since when a Z-ion strays away from the plane to distances $x - a \ll b$, the electric field of his neighbors has no significant $\widehat{x}$ projection. In this range, the stray Z-ion is only affected by the electric field of its Wigner-Seitz cell (a disk of radius b). Therefore, at $x - a \ll b$, the surface charge of the macroion is unscreened, and the electric field is $2\pi\sigma/\varepsilon$. Thus, for $0 < x - a \ll b$,

$$N(x) = \frac{\sigma}{Ze\lambda} \exp[-(x-a)/\lambda]. \tag{4.3}$$

(Here following [78] we used an expression for $N(a)$ that ignores the atomic structure of water, while [67, 22] tried to take this structure into account).

Remarkably, the same length λ characterizes both this exponential decay and the Gouy-Chapman solution, equation (4.1). It is clear that the dramatic difference between the exponential decay of equation (4.3) and the power law decay of equation (4.1) is due

to the effects of correlations. Equation (4.3) was first obtained in [67, 22]. Then it was re-derived in [69, 72] and confirmed by Monte Carlo (MC) simulations in [81]. Below we again confirm equation (4.3) at $0 < x - a \ll b$ by MC simulations. However, the focus of this Chapter is on the non-PB behavior of $N(x)$ at larger distances $x - a > b$, which has been predicted in [67, 22] but to our knowledge has never been verified analytically or numerically.

To bring this prediction to mind, let us focus on a single, stray Z-ion located above the macro-ion's surface at $x > a + b$ (Fig. 4.2). Refs. [67, 22] argue that the negative charge of the correlation hole, $-Ze$, will spread to a disc of size $\sim x$ as neighboring Z-ions move to occupy the Wigner-Seitz cell the stray Z-ion left behind. This is similar to what happens in a metallic surface under the influence of an external charge. In fact, this metal-like polarization of the SCL on the surface of the macroion can actually be described by an image charge that appears in the body of the macroion. Because the centers of the Z-ions which form the SCL are typically located at a distance $x_c = a + \lambda$ above the surface (see Fig. 4.2) it is natural to think that the effective metallic surface is at $x_{met} = x_c$ and therefore the image is located at $-x+2x_{met}$. The attractive interaction energy between the stray Z-ion and its image is then [85], for $x - x_{met} \gtrsim b$,

$$U_{im}(x) = -\frac{Z^2 e^2}{4\varepsilon(x - x_{met})}. \tag{4.4}$$

This attractive image interaction, of course, is a correlation effect.

The goal of this Chapter is to verify, by a Monte Carlo (MC) simulation and an analytical calculation, that a SCL on the insulating surface of a macroion does behave as a metal, and a stray Z-ion has potential energy $U_{im}(x)$. The plan of the Chapter is as follows. In section 4.3 we describe our MC procedure. In section 4.4, we present our MC results for the screening of a spherical macroion by Z-ions. To a first approximation they confirm that a stray Z-ion at $x > a + b$ has potential energy $U_{im}(x)$. This is the most important result of this Chapter .

At a more detailed level, we see in section 4.4 that to more accurately fit equation (4.4) to our MC data the effective metallic surface must be lifted slightly above x_c. We find that a shift of 0.21 nm provides the best fit. This shift is explained in section 4.5 where we analytically derive equation (4.4), showing that there is indeed an attractive interaction energy between the stray Z-ion and its image. We further prove

that the effective metallic surface should be lifted slightly by $-\xi = |\xi|$, where 2ξ is the linear screening length of the SCL. In other words, x_{met}, in equation (4.4) should be replaced by $x_{met} = x_c - \xi = x_c + |\xi|$. We show that, theoretically, $\xi = -0.20$ nm, in reasonable agreement with the MC simulation. The fact that a Wigner-crystal-like SCL has a negative screening radius was predicted theoretically [86] and confirmed experimentally for a low-density two-dimensional electron gas in silicon MOSFETs and GaAs heterojunctions [87, 88] (see also a recent paper [89]).

In section 4.6 we add a small concentration of monovalent salt (for example, NaCl) to our system. We show that the attractive image interaction persists in this system; however, the attraction is weaker due to screening.

4.3 Monte Carlo Simulation

Our setup is similar to the simulations found in [81, 90, 91, 92, 93, 94]. Our system is contained within a spherical cell with radius $r_{max} = 10.0$ nm. Centered within the cell is a spherical macroion with charge $Q_M = -300e$ and radius $R_M = 5.0$ nm ($-\sigma = -0.95$ e/nm^2). The system is populated by 100 Z-ions of charge $3e$ and radius $a = 0.4$ nm. The mobile particles are initialized to random non-overlapping coordinates. The wall of the spherical cell has a distance of closest approach of 0 so that a Z-ion may be placed with its center at the wall. Therefore all Z-ions are found at a radial distance r within the range $R_M + a < r \leq r_{max}$. After initializing the system, the total electrostatic energy of the system is calculated as

$$\mathcal{E} = \frac{e^2}{2\varepsilon} \sum_{i,j;i\neq j}^{101} \frac{q_i q_j}{d_{ij}}, \tag{4.5}$$

where particle i has charge q_i ($q_1 = Q_M$, and for $i > 1$, $q_i = Ze$) located at the center of a hard sphere with radius η_i ($\eta_1 = R_M$, and for $i > 1$, $\eta_i = a$). The distance between particles i and j is d_{ij}. The dielectric constant is set to $\varepsilon = 80$ everywhere and there are no interactions with anything outside of the cell.

Selecting a particle at random, the MC program attempts to reposition it randomly within a cubic volume of $(3.2\text{ nm})^3$ centered on the particle's current position. The total electrostatic energy of the system, $\mathcal{E}$, is calculated after each attempted move. Modeled as hard spheres, if any of the particles overlap after an attempted move, such

that $d_{ij} < \eta_i + \eta_j$ the move is rejected. Additionally, any attempted move that places a particle outside of the cell, $r > r_{max}$, is also rejected. Otherwise, moves are accepted or rejected based on the traditional Metropolis algorithm. Simulations attempt 52 billion moves, of which $\sim 4\%$ are accepted, resulting in each particle being moved an average of 20 million times. This low acceptance rate is due to most of the Z-ions being condensed on the macroion surface where their average separation is $\sim b = 1.0$ nm; one can increase the rate to $\sim 8\%$ by shrinking the volume in which the Z-ion is randomly repositioned to $(1.6 \text{ nm})^3$. To ensure thermalization, 5 million moves are attempted before beginning the analysis of $N(r)$, the Z-ion's radial distribution.

Following thermalization, $N(r)$ is computed after every 20,000 attempted moves by dividing the simulation space around the central macroion into bins that are concentric spherical shells of thickness 0.1 nm, counting the ion population within each bin, and then calculating the average Z-ion density of each bin. We now introduce the empiric mean field potential, $\phi(r)$, which corresponds to the MC $N(r)$, and is calculated from the radial distributions of the ions in the following way. First, the electric field is determined at the outer edge of each spherical shell by applying Gauss' Law to the integrated charge. Then, the potential $\phi(r)$ is calculated by discreetly integrating the electric field in the radial direction. The empiric mean-field potential, $\phi(r)$, has nothing to do with the PB potential obtained by a solution of the spherical PB equation because, due to correlation effects, the MC $N(r)$ differs from equation (4.1). In the present case, Z-ions are strongly condensed at the surface of the macroion, and therefore the potential $\phi(r)$ decays so fast with r that the interaction energy of a stray Z-ion, $Ze\phi(r)$, becomes less than k_BT already at $r > 5.65$ nm.

The main point of this Chapter is that the concentration of Z-ions, $N(r)$, at a distance r from the center of the macroion, is only weakly influenced by the empiric mean-field potential energy $Ze\phi(r)$ and is mostly determined by the attractive correlation energy $U_c(r)$. We extract $U_c(r) - U_c(r_{max})$ from the simulation data assuming that Z-ions that stray from the macroion surface are Boltzmann distributed according to,

$$N(r) = N(r_{max}) \exp\left(-\frac{Ze\phi(r)}{k_BT} - \frac{U_c(r) - U_c(r_{max})}{k_BT}\right), \tag{4.6}$$

so that the change in the attractive correlation energy for a Z-ion moved from r_{max} to

r is

$$U_c(r) - U_c(r_{max}) = -k_B T \ln\left(\frac{N(r)}{N(r_{max})}\right) - Ze\phi(r), \tag{4.7}$$

where we took into account that $\phi(r_{max}) = 0$ because our system is neutral.

We need to recalculate the theoretical form of U_{im} for a spherical macroion geometry (see Fig. 4.3), to test that, for $r - R_{met} \gtrsim b$,

$$\Delta U(r) \equiv \Big[U_c(r) - U_c(r_{max})\Big] - \Big[U_{im}(r) - U_{im}(r_{max})\Big] = 0. \tag{4.8}$$

It is known [85] that a charge Ze at a distance $r > R_{met}$ from the center of a conducting sphere with radius R_{met} and a net charge of $-Ze$, induces two image charges within the sphere. The charge $q' = -ZeR_{met}/r$ is located at a distance $r' = R_{met}^2/r$ from the sphere's center, and the compensating charge $-q'$ is located at the center of the sphere. The net charge of the macroion and the SCL, $-Ze$, accounts for the departure of the stray Z-ion and is also fixed at the center of the sphere.

In the presence of these three charges a stray Z-ion, located at r, has potential energy given by

$$U_{im}(r) = -\frac{(Ze)^2}{r\varepsilon} + \frac{Zeq'}{2(r-r')\varepsilon} - \frac{Zeq'}{2r\varepsilon}. \tag{4.9}$$

The net charge $-Ze$ has fixed magnitude and position because, unlike charges q' and $-q'$, it is not created by the stray Z-ion polarizing the SCL; therefore, the interaction term that involves the net charge does not include a factor of 1/2. In the limit $x = r - R_M \ll R_M$, we recover the planar $U_{im}(x)$ of equation (4.4), because $U_{im}(r)$ is dominated by the influence of charge $q' \simeq -Ze$ located at $r' \simeq R_{met} - r$.

The first term within the parentheses of equation (4.9) is written for the case when all but one of the mobile charges (Z-ions) are located, as in metal, at the surface. This term then describes a stray Z-ion's attraction to the fraction of Q_M left uncompensated due to its departure. In other words, this term is used to exclude the stray Z-ion's self interaction with its contribution to the mean-field potential[1] .

[1] Actually, $N(r)$ has a tail at $r > R_M + a$. As a result, when a stray Z-ion is located at $r > R_M + a$, depletion of the mean distribution not only occurs at the surface of the macroion, but a small fraction, δ, of the total depletion also occurs at distances larger than r. For $r = 6.1$ nm this fraction is 0.02. As a result, the absolute value of this interaction energy is smaller than Z^2e^2/r by $\sim 2\%$. In equation (4.9) and below we neglect this small effect.

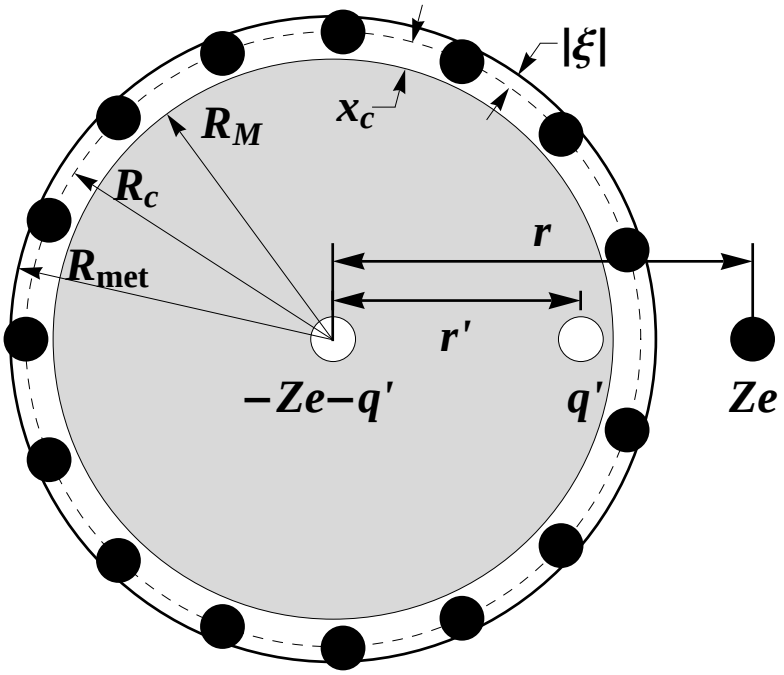

Figure 4.3: The generalization of Fig. 4.2 to a spherical geometry. A stray Z-ion with charge Ze is shown in a cross-sectional view at a distance r from the center of a spherical macroion with charge Q_M, which is covered by condensed Z-ions (black spheres). The condensed Z-ions are located at an average distance of $R_c \equiv R_M + x_c = R_M + a + \lambda$ from the center of the macroion. The stray Z-ion makes a correlation hole with charge $-Ze$, where the concentration of Z-ions is depleted. The resulting correlation potential can be modeled as if the Z-ion were near a metallic sphere with effective radius $R_{met} = R_c + |\xi|$. The image charges, $-Ze$ and $-q'$ located at the center, and q' located at a distance r' away from the center, are shown by white spheres.

To compare equation (4.9) to the simulation in the next section, we take $R_{met} = R_M + x_c \equiv R_c$, which aligns the metallic surface with the average position of the centers of the Z-ions that comprise the SCL (see Fig. 4.3). Because our macroion is a sphere and not a plane, the magnitude of its electric field drops as $E \propto 1/r^2$ at $r > R_M$. Therefore, $E = 2\pi\sigma/\varepsilon$, used to calculate λ, should be modified slightly since the Z-ion's centers are never closer than a to the macroion's surface. We introduce $\sigma_s = \sigma[R_M/(R_M + a)]^2$ to correct the electric field. This leads to, $\sigma_s = 0.819\ e/\text{nm}^2$, $\lambda_s = 0.0913$ nm, $\Gamma_s = 5.9$, and $R_{met} = 5.49$ nm.

4.4 Results of MC simulation

$\Delta U(r)$ (equation (4.8)), the difference between the attractive correlation energy extracted from the MC simulation and the result of the image theory is plotted in Fig. 4.4 for $R_{met} = 5.49$ nm (green circles). As expected, when $r - R_{met} \lesssim b$, i.e. at $r \lesssim 6.5$ nm the difference is significantly less than zero since in this range the SCL does not function well as a metal due to its discreteness, and, therefore, the attractive correlation energy, $U_c(r)$, saturates. However, there is also weaker disagreement for $r \gtrsim 6.5$nm, which decreases with distance from the macroion. This suggests that we have improperly identified the radius of the effective metallic sphere used to calculate $U_{im}(r)$. To allow for the adjustment of R_{met}, we introduce the length $|\xi|$ so that

$$R_{met} = R_c + |\xi|. \tag{4.10}$$

By minimizing the root-mean-square of $\Delta U(r)$ with respect to $|\xi|$, on the interval 6.4 nm $\leq r \leq$ 7.4 nm, we determined that $|\xi| \simeq 0.21$ nm provides the best fit for $\Delta U(r) = 0$. The quality of this fit is illustrated in Fig. 4.4 (red diamonds). This small correction $|\xi|$ to R_c indicates that the foundation of equation (4.9), the attractive image interaction, is sound.

In section 4.5, we analytically calculate $U_{im}(x)$ in order to find the necessary adjustment in R_{met} by considering the response of a SCL, made up of adsorbed Z-ions on a planar macroion, to the presence of a single stray Z-ion above the SCL. It is determined that the SCL screens the potential of the stray Z-ion with a negative screening length, 2ξ, where $\xi = -0.20$ nm. This moves the effective metallic surface further away from the macroion's surface by $|\xi| = 0.20$ nm in reasonable agreement with the MC data (see Fig. 4.2 and Fig. 4.3).

In Fig. 4.5, the concentration $N(r)$ obtained from the MC simulation is compared to

$$N(r) = N(r_{max}) \exp\left(-\frac{Ze\phi(r)}{k_B T} - \frac{U_{im}(r) - U_{im}(r_{max})}{k_B T}\right), \tag{4.11}$$

which uses $\xi = -0.21$ nm to calculate $U_{im}(r)$ (both $\phi(r)$ and $N(r_{max})$ are obtained from the MC simulation). The agreement between the MC data and equation (4.11) is obvious when $r \gtrsim 6.5$ nm. In Fig. 4.5, we also compare equation (4.3), modified for a

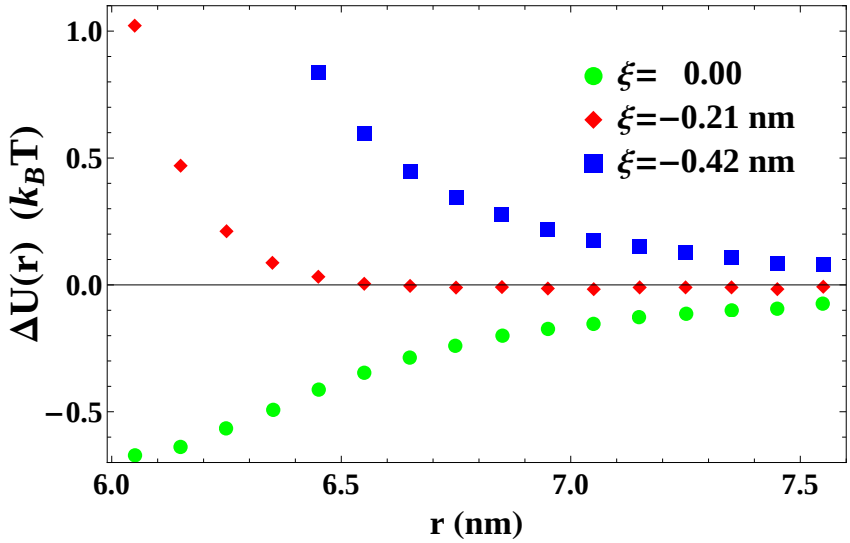

Figure 4.4: The difference, $\Delta U(r)$ (equation (4.8)), between the correlation attraction energy extracted from the MC simulation and the result of the image theory, as a function of a stray Z-ion's distance from the center of the macroion for three different values of the adsorbed Z-ion's screening length, 2ξ. The length, $|\xi|$, determines the increased radius, $R_{met} = R_M + a + \lambda + |\xi|$, of the effective metallic sphere used to calculate $U_{im}(r)$ (Eq (4.9)). The green circles correspond to $\xi = 0$, assumed in the original theory of [67, 22]. The red diamonds correspond to the best fit to zero, $\xi = -0.21$ nm. The blue squares correspond to, $\xi = -0.42$ nm and are shown for comparison.

spherical geometry,

$$N(r) = \frac{\sigma_s}{Ze\lambda_s} \exp\left[-\frac{(r - R_M - a)}{\lambda_s}\right], \tag{4.12}$$

to the MC concentration data. At small distances, $r - R_M + a \lesssim b$, i.e. $r \lesssim 5.8$ nm, we find good agreement with the exponential decay predicted in [67, 22] and confirmed in [69, 72, 81].

Let us now comment on what happens at larger distances from the macroion, which are not shown in Fig. 4.5 and can not be studied well with the small size of the simulation cell used in this Chapter . According to [67, 22], at distances larger than

$$\Lambda = \left(\frac{e\lambda}{2\pi Z\sigma l_B}\right)^{1/2} \exp\left(\frac{|\mu|}{2k_BT}\right) \tag{4.13}$$

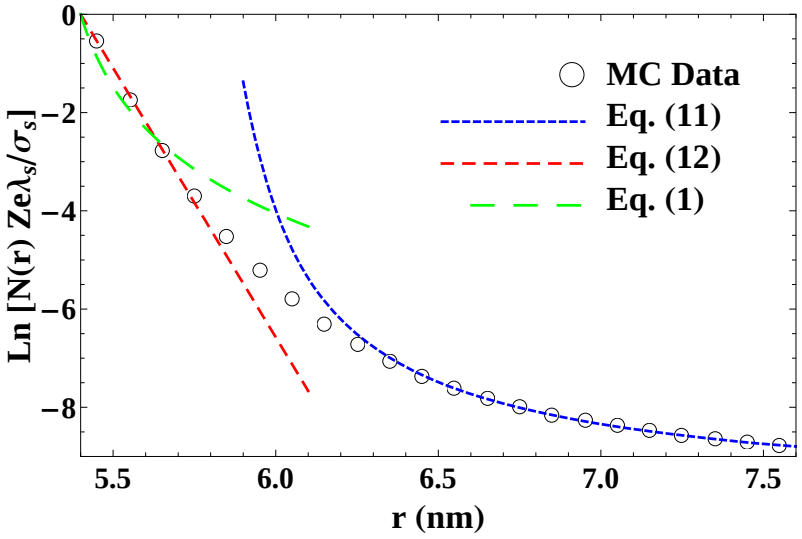

Figure 4.5: Concentration of Z-ions, $N(r)$, as a function of distance from the center of the macroion, starting at $R_M + a = 5.4$ nm. The circles represent the data from the MC simulation. The result of the image theory, equation (4.11), is shown by short, blue dashes. The medium length, red dashes show equation (4.12). The long, green dashes show the Gouy-Chapman solution (equation (4.1)), with λ_s substituted for λ. The error bars for the MC data are smaller than the size of the symbols.

from the planar macroion the PB approximation takes over and

$$N(x) = \frac{1}{2\pi Z^2 l_B} \frac{1}{(\Lambda + x - a)^2}. \tag{4.14}$$

Here μ is the chemical potential of a Z-ion in a SCL. It has been shown that for a SCL on a charged background (one-component plasma), at $1 < \Gamma < 15$, μ is approximated well by [22, 95],

$$\mu = -k_B T(1.65\Gamma - 2.61\Gamma^{1/4} + 0.26 \ln \Gamma + 1.95), \tag{4.15}$$

where the first term of this expansion corresponds to the chemical potential of a Wigner Crystal. For our parameters, $Z = 3$ and $\sigma = \sigma_s = 0.819e$ nm^{-2}, this leads to the length $\Lambda = 5.18$nm. Then, the approximate extension of equation (4.14) to the spherical geometry using $x = r - R_M$ at $r = 7.55$ nm gives $\ln[N(r)Ze\lambda_s/\sigma_s] = -8.65$, very close to the MC result -8.77 (see Fig. 4.5). The idea behind the results of equation (4.13) and equation (4.14) is that the correlation physics at small distances $x - x_c \ll \Lambda$, produces

a new boundary condition on the concentration of Z-ions for the long distance solution of the PB equation [67, 22].

The authors of a recent paper have already [96] studied $N(r)$ at large distances by MC simulation in a much larger spherical cell and found that it is in agreement with the predictions of the PB approach based on the correlation driven boundary condition. They, however, did not identify the image domain of distances r which we concentrate here upon. Thus, all three asymptotic regimes, predicted in [67, 22], namely equation (4.3) at $x - a < b$, equation (4.4) at $b < x - a \ll \Lambda$, and equation (4.14) at $x - a > \Lambda$ are now confirmed by MC simulations.

We have shown above that the standard mean-field theory [13, 14] fails to describe screening by multivalent counterions. Let us now show that another mean-field approximation, which we call the empiric mean-field, fails more dramatically. The empiric mean-field potential, $\phi(r)$, was introduced in section 4.3 and is obtained using the distribution of charge realized in our MC simulation. In Fig. 4.6, we compare the Z-ion concentration obtained from the MC simulation to the Z-ion concentration predicted using the empiric mean-field potential,

$$N(r) = N_0 \exp\left(-\frac{Ze\phi(r)}{k_B T}\right). \tag{4.16}$$

Here, $N_0 = 2.18 \times 10^{-2}$ nm^{-3} is the concentration necessary to normalize the number of Z-ions, in the range 5.4 nm $< r <$ 10.0 nm, to 100. Clearly, the empiric mean-field potential is not self-consistent; equation (4.16) predicts that there are many more Z-ions, at $r >$ 6.0 nm, than are actually present in the distribution that produced $\phi(r)$. The distribution of the Z-ions, for $r - R_{met} \gtrsim b$, is strongly influenced by the attractive correlation interaction and, therefore, cannot be predicted by the empiric mean-field interaction alone.

4.5 Theory of image potential and effective metallic surface

In this section we return to the plane geometry of Fig. 4.2 and analytically derive equation (4.4) for $U_{im}(x)$. In the process of this derivation, we find the theoretical location, x_{met}, of the effective metallic surface. The probe charge, a stray Z-ion, is

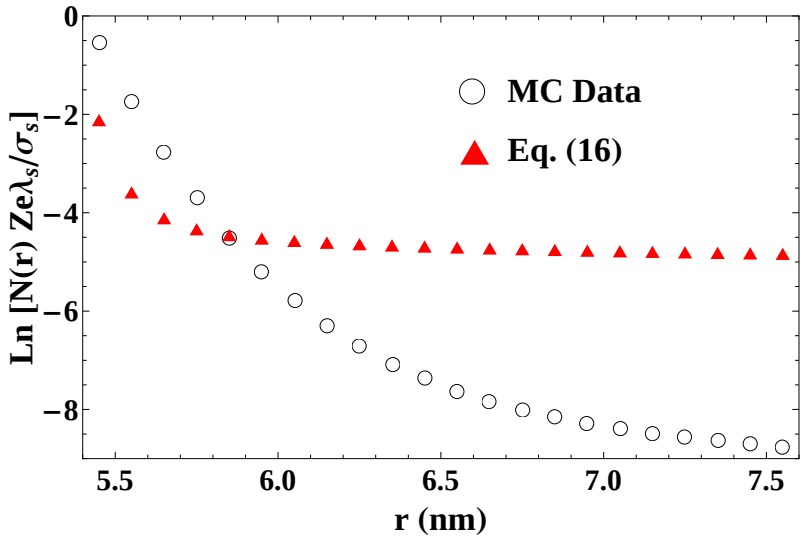

Figure 4.6: Concentration of Z-ions, $N(r)$, as a function of distance from the center of the macroion. The MC concentration (circles; the same data as in Fig. 4.5) differs strongly from the concentration of Z-ions (red triangles) obtained from equation (4.16) with the empiric mean-field potential potential $\phi(r)$.

positioned far above the plane at $x' = x \gg b$ and $\varrho = 0$, where x' is the axis and ϱ is the radius of the cylindrical coordinate system (x', ϱ, θ). A SCL of Z-ions is located in the (ϱ,θ) plane at $x' = x_c$, where the typical distance that separates adjacent Z-ions is b.

The plan of this section consists of, (1) determining the analytic solution for the total potential of the system, $\psi(\varrho, x')$, (2) presenting it as a sum of two potentials: one of the stray Z-ion and the other of the induced charge density of the SCL, $\psi_{ind}(\varrho, x')$ (the potential of a point like image) and (3) finding the position of the effective metallic plane, x_{met}, so that the attractive interaction energy $\frac{1}{2}Ze\psi_{ind}(0, x) = U_{im}(x)$. Below, we show that $x_{met} = x_c - \xi$, where 2ξ is the screening length of the SCL, which we also calculate.

To find the potential $\psi(\varrho, x')$ we solve Poisson's equation,

$$\nabla^2\psi\left(\varrho, x'\right) = -\frac{4\pi}{\varepsilon}\rho(\varrho, x'), \tag{4.17}$$

where $\rho(\varrho, x') = \rho_{ext}(\varrho, x') + \rho_{ind}(\varrho, x')$, with $\rho_{ext} = Ze\delta(\varrho)\delta(x' - x)/(\pi\varrho)$, and the

charge density that is induced within the SCL is given by

$$\begin{aligned}\rho_{ind}(\varrho, x') &= Ze\left[n\Big(\psi(\varrho, x_c)\Big) - n(0)\right]\delta(x' - x_c) \\ &= Ze\psi(\varrho, x_c)\frac{dn}{d\psi}\delta(x' - x_c) \\ &= -(Ze)^2\psi(\varrho, x_c)\frac{dn}{d\mu}\delta(x' - x_c). \end{aligned} \tag{4.18}$$

Here, $n(\psi)$, is the number of Z-ions per unit area as a function of the local total potential, $\psi(\varrho, x_c)$, and μ is the chemical potential of the SCL. We consider the case, $x - x_c \gg b$, when the stray Z-ion produces a weak potential in the $x' = x_c$ plane ($Ze\psi(\varrho, x_c)/k_BT \ll 1$). This allows us to linearize ϱ_{ind} with respect to ψ, in equation (4.18). Rewriting equation (4.17) with the help of equation (4.18) results in

$$\nabla^2\psi\left(\varrho, x'\right) = -\frac{4\pi}{\varepsilon}\rho_{ext}(\varrho, x') + \frac{1}{\xi}\psi(\varrho, x_c)\delta(x' - x_c), \tag{4.19}$$

where,

$$\xi = \frac{\varepsilon}{4\pi(Ze)^2}\frac{d\mu}{dn} = \frac{1}{2\kappa}, \tag{4.20}$$

and κ is the inverse screening length of the SCL of adsorbed Z-ions [89, 97].

In order to calculate ξ we use $\mu(n)$ as given by equation (4.15) and the definition of Γ from equation (4.2) and $b = (\pi n)^{-1/2}$. For $Z = 3$, $\sigma = \sigma_s = 0.819\ e/\text{nm}^2$ and $\varepsilon = 80$, we find that $\xi = -0.20$ nm.

In order to solve equation (4.19) for $\psi(\varrho, x')$, we substitute

$$\psi(\varrho, x') = \int_0^\infty kA_k(x')J_0(k\varrho)dk, \tag{4.21}$$

into equation (4.19), where $A_k(x')$ are the coefficients of the expansion and $J_0(k\varrho)$ is the zeroth order Bessel function. As demonstrated in Appendix B, this yields [97]

$$\begin{aligned}\psi(\varrho, x') = &\frac{Ze}{\varepsilon}\frac{1}{\sqrt{(x - x')^2 + \varrho^2}} - \\ &\frac{Ze}{\varepsilon}\int_0^\infty \frac{1}{2k\xi + 1}\exp\left[-k(x' + x - 2x_c)\right]J_0(k\varrho)dk,\end{aligned} \tag{4.22}$$

Because the screening length $\xi < 0$, the second term diverges. To obtain a solution despite this pole, following [89], we consider the contribution to $\psi(\varrho, x')$ from $k \ll 1/|\xi|$,

only. Such an approach is valid if the stray Z-ion, and the observation point x', are a large distance away from the SCL: $(x - x_c), (x' - x_c) \gg |\xi|$. This allows us to expand $1/(2k\xi + 1)$ in equation (4.22) around $k = 0$, so that $1/(2k\xi + 1) \simeq 1 - 2k\xi$, and we arrive at

$$\psi(\varrho, x') = \frac{Ze}{\varepsilon\sqrt{\varrho^2 + (x - x')^2}} - \frac{Ze}{\varepsilon\sqrt{\varrho^2 + (x' + x - 2x_c)^2}} + \frac{2(x' + x - 2x_c)Ze\xi}{\varepsilon\left[\varrho^2 + (x' + x - 2x_c)^2\right]^{3/2}}. \tag{4.23}$$

The first term of equation (4.23) is the potential created directly by the stray Z-ion. The other two terms are the first two terms of the expansion of the induced potential, $\psi_{ind}(\varrho, x')$, with respect to ξ. We are now in a position to recast $\psi_{ind}(0, x)$ at $(x - x_c) \gg |\xi|$, as being created by an image charge a distance s below the stray Z-ion,

$$\begin{aligned} \frac{1}{2}Ze\psi_{ind}(0, x) &= -\frac{(Ze)^2}{4(x - x_c)\varepsilon} + \xi\frac{(Ze)^2}{4(x - x_c)^2\varepsilon} \\ &\simeq -\frac{(Ze)^2}{2s\varepsilon} = U_{im}(x), \end{aligned} \tag{4.24}$$

where, $s = 2(x - x_c + \xi)$. Specifying that the metallic plane must lie half way between the real charge and the image charge sets its position at $x_{met} = x - s/2 = x_c - \xi$. Therefore the effective metallic plane is found a distance ξ above the plane of the adsorbed Z-ion's centers (Fig. 4.2). This agrees with the statement of [89], that the potential created by the stray Z-ion is negative in the $x' = x_c$ plane. The theoretical value $\xi = -0.20$ nm is in reasonable agreement with our MC result, $\xi = -0.21$ nm (section 4.4). Moreover, we have demonstrated that the image attraction predicted in [67, 22] can be derived analytically in the limit $x \gg b$.

4.6 Screening the image by adding 1:1 salt

In this section we modify our system to include a small concentration of 1:1 salt molecules such as NaCl. By taking into account the effect of screening on the attractive interaction energy between a stray Z-ion and its image, U_{im}, we obtain a new prediction for the concentration of Z-ions, $N(r)$, which is in reasonable agreement with

the new MC results. In calculating U_{im} we assume that the concentration c of 1:1 salt is so small that the total potential ψ at any point in the bulk solution ($r \gtrsim 6.0$ nm) obeys the linearized Poisson-Boltzmann equation,

$$\nabla^2\psi = \kappa_b^2\psi, \tag{4.25}$$

where $1/\kappa_b$ is the Debye-Hückel (DH) screening length,

$$\frac{1}{\kappa_b} = \sqrt{\frac{\varepsilon k_B T}{8\pi e^2 c}}. \tag{4.26}$$

The exact solution of equation (4.25) for a point charge a distance $r - R_{met}$ away from the surface of a grounded metallic sphere in a weak electrolyte is known [98]; however, we will avoid the complexity of this solution and approximate the spherical macroion and its SCL as a grounded metallic plane. As seen in Fig. 4.7, where equation (4.4) is used to calculate $N(r)$ (short blue dashes) for $c = 0$, one obtains reasonable agreement with the MC $N(r)$ (circles) without using equation (4.9) as we did in section 4.4. This demonstrates that the influence of the total central charge, $-Ze - q'$, is very small. The reason for this is that when a stray Z-ion is close to the macroion surface, the total central charge is much smaller than the image charge q'. Additionally, the central charge is much farther from the stray Z-ion than the image charge q'. When the system includes 1:1 salt, the influence of the total central charge is further reduced due to screening.

Consider a Z-ion which is submerged in a weak electrolyte solution with dielectric constant ε, and is a distance $x - x_{met}$ above a grounded metallic plane located at x_{met} (see Fig. 4.2). For this system, the solution to equation (4.25), subject to the boundary condition $\psi(x_{met}) = 0$, can be found using the method of images [98]. To satisfy the boundary condition, the image potential must exactly cancel the potential of our Z-ion in the metallic plane. Such an image potential is provided by the DH screened potential of a charge $(-Ze)$ located at $x' = -x + 2x_{met}$.

The interaction energy of a stray Z-ion with its screened image is now readily calculated and is given by,

$$U_{im}(x) = -\frac{Z^2e^2}{4\varepsilon(x - x_{met})}\exp(-2\kappa_b[x - x_{met}]). \tag{4.27}$$

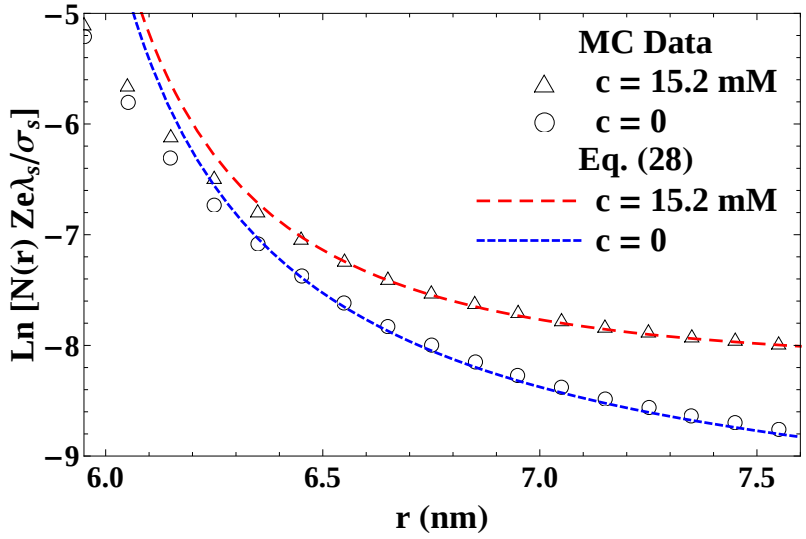

Figure 4.7: Concentration of Z-ions, $N(r)$, in a weak electrolyte solution, as a function of distance from the center of the macroion. The shapes represent the data from the MC simulations for two different concentrations of 1:1 salt: 15.2 mM (triangles), and 0 (circles). The result of the screened image theory, equation (4.28) with $x = r - R_{met} + x_{met}$, is shown by medium length red dashes for c=15.2 mM, and short blue dashes for c=0. The error bars for the MC data are smaller than the size of the symbols.

In the limit of infinite dilution $c \to 0$, or equivalently $\kappa_b \to 0$, equation (4.27) is equal to equation (4.4), as expected. Onsager and Samaras [99] obtained the same result, but with the opposite sign, for an ion's interaction with its image at an electrolyte-air interface resulting in a repulsive force. To compare equation (4.27) to the spherical geometry of our MC simulation, we take $x = r + x_{met} - R_{met}$ using $R_{met} = R_c + |\xi|$.

The MC simulation described in section 4.3 was modified to include M 1:1 salt molecules, resulting in M ions of charge e and M ions of charge $-e$. All of the monovalent salt ions have their charge at the center of a hard sphere with radius $\eta = 0.2$ nm. We studied a 1:1 salt concentrations of 15.2 mM corresponding to the addition of $M = 34$ salt molecules to the solution. The following changes were made to the MC simulation to properly incorporate the new ions. The sum used to calculate the total electrostatic energy of the system (equation (4.5)) was changed to include the monovalent ions, and the monovalent ions were also incorporated into the calculation of the empiric mean-field potential $\phi(r)$.

In Fig. 4.7, the concentration N(r) obtained from the MC simulations is compared to

$$N(r) = N(r_0) \exp\Bigg(- \frac{Ze[\phi(r) - \phi(r_0)]}{k_B T} - \frac{U_{im}(r) - U_{im}(r_0)}{k_B T} \Bigg), \tag{4.28}$$

which uses $\xi = -0.21$ nm to calculate $U_{im}(x)$ (equation (4.27)) (both $\phi(r)$ and $N(r_0)$ are obtained from the MC simulations). Because there are no screening particles outside of the simulation cell, Z-ions near the wall of the cell are repelled from this interface [68] even though there is not a jump in the dielectric constant. To keep this effect separate from the image interaction of interest, we chose our reference point at $r_0 = 8.05$ nm instead of r_{max}. Because the stray Z-ion's attraction to the image is reduced by screening, we see that in Fig. 4.7 the concentration of Z-ions is higher at distances $r > 60$ nm when 1:1 salt is present in the solution. Even with the addition of 1:1 salt to the solution the agreement between the MC data and equation (4.28) for $r \gtrsim 6.5$ nm is reasonable, demonstrating that the metallic behavior of the SCL on the macroion surface survives, and that the image attraction is still important to determining the Z-ion's concentration.

4.7 Summary and the origin of charge inversion

To summarize, we have studied the role of correlations among adsorbed Z-ions in attracting stray Z-ions and influencing their distribution in the screening atmosphere. Adsorbed Z-ions on the surface of the macroion form a strongly correlated liquid (SCL). The SCL acts as an effective metallic surface for Z-ions that stray from the macroion surface to distances larger than the average distance between Z-ions of the SCL. Using Monte Carlo (MC) simulations, we verified the theoretical prediction [67, 22] that a stray Z-ion is attracted to its electrostatic image created behind the effective metallic surface. As a small correction to [67, 22], however, our MC simulation showed that the effective metallic surface is not aligned with the average position of the adsorbed Z-ion's centers, but is slightly above the adsorbed Z-ion's centers. This offset was calculated analytically to be $|\xi|$, where 2ξ is the screening length of the SCL. Our analytic theory is in reasonable agreement with the MC data. Extending the original image theory of

[67, 22], we demonstrated that the attractive image interaction, while screened, persists in a weak electrolyte.

In [70] the attractive image interaction, which we have studied here, was used to interpret the origin of the negative chemical potential of the condensed Z-ions (equation 4.15). As a stray Z-ion, attracted to its image, approaches the surface of the macroion it reaches a distance, $r \sim R_M + b$, where the SCL fails to act as a good metal and the correlation attraction $U_c(r)$ saturates at $\mu \sim -Z^2e^2/4\varepsilon b$; this saturation can be seen in Fig. 4.5 as the growth of $\Delta U(r)$ at $r < 6.5$ nm. It is this negative chemical potential, brought about by the attractive image interaction, at $r \gtrsim R_{met} + b$, which drives charge inversion (over compensation of the macroion's bare charge with condensed Z-ions), a phenomenon that has generated much interest [67, 22, 78, 79, 73, 80, 69, 72, 81]. Thus, we believe that this work helps to clarify the origin of charge inversion.

Chapter 5

Conclusion

This thesis presents a new theory for the capacitance of the electric double layer (EDL), which was developed in Refs. [32, 51, 52]. This theory lays the groundwork for a new understanding of the EDL in a regime where ions are strongly attracted to their images in a metallic electrode, $u_{im} \gg k_B T$. Through the careful consideration of these electrostatic image charges *and* lateral ion-ion correlations we have demonstrated that $C > C_H$ is possible. This is in strong contrast to mean-field theories, such as Gouy-Chapman-Stern [13, 14, 15] and the more recent work of Kornyshev [12], Kilic [47] and Oldham [56], which all predict that capacitance may not be larger than C_H. Moreover, even Modified Poisson Boltzmann theories that account for the attraction of ions to their images, but overlook lateral correlations, claim C_H as the maximum capacitance [43]. Returning to the pioneering work of Torrie [39], the Monte Carlo (MC) simulations presented in this thesis treat the electrode as a conductor, by the inclusion of image charges. By simulating dense electrolyte systems at low temperatures, where $u_{im} \gg k_B T$, we have obtained capacitance results that confirm $C > C_H$ is possible for the primitive model.

In addition to allowing large capacitance, image charges and lateral correlations were shown to be important in determining the concentration of multivalent ions around a highly charged macro-ion. Through MC simulation, we confirmed that the origin of charge inversion can be explained through the lateral ion-ion and ion-image correlations.

This final Chapter will serve to summarize the main results and describe interesting directions for theory and simulation.

5.1 Capacitance of room temperature ionic liquids

In Chapter 2, Monte Carlo simulations of a room temperature ionic liquid (RTIL) in contact with a conducting electrode were performed using the restricted primitive model. Capacitance values as large as $3C_H$ were obtained. When the metallic electrode is a good conductor, the $C(V)$ curve has a "bell-shape" with a peak at $V = 0$. On the other hand, when the simulated electrode is not a perfect metal the $C(V)$ curve is "camel-shaped", meaning that the capacitance first grows with V, reaches a maximum and then decays at larger V. These results are interpreted through a semi-quantitative analytical theory based on the weak repulsion between ion-image dipoles at the surface of the electrode. These conclusions are in qualitative agreement with experimental data.

There are a number of effects ignored by the restricted primitive model, such as ion size asymmetry, ion polarizability and disorder at the electrode surface. Despite this, our results may be quite relevant for real-world experiments on room temperature ionic liquids. If a dielectric constant $\varepsilon \sim 3$ is included to crudely account for the polarizability of the ions, we would obtain $C \sim 3\varepsilon C_H = 18\ \mu\mathrm{F/cm}^2$, a value that is in agreement with typical capacitance measurements on RTILs [18, 19, 20]. This suggests that the restricted primitive model does in fact contain the necessary elements to reasonably model some RTILs.

To further develop the semi-quantitative theory used in this Chapter , it would be beneficial for the role of neutral pairs to be examined more closely through simulations, perhaps addressing the role of their polarization as they respond to the excess charge at the electrode surface. Along the same lines, a rigorous examination of the correlations among excess ions at the electrode surface would serve to validate the basis of the theoretical model.

The results of our current theory suggest a potential method for increasing the capacitance of energy storage devices based on an RTIL electrolyte: reduce the interaction energy between adjacent ions through the presence of electrostatic images. We have described a geometry in which ions form compact ion-image dipoles that are weakly interacting on the planar surface of an electrode. The interaction energy between ions can be reduced further if ions enter a 2-D metallic slit or a 1-D metallic pore where image charges more effectively screen the potential of each ion. A number of papers

have already begun to address these possibilities [100, 101], achieving capacitances in excess of $10C_H$ within MC simulations.

5.2 Capacitance within the one component plasma approximation

Chapter 3 built off of the observation that $C > C_H$ was observed in simulations with asymmetrically sized ions in Sec. 2.5.2. We imagined a system in which one ion is so large that it is sterically prohibited from motion, while the other is small enough to move through the hollow spaces between the larger ions. By treating this case in the approximation of a "one-component plasma" model, where only one ion species is mobile while the other forms a uniformly charged background, we were able to develop a theoretical understanding over the full range of temperature. This theory again abandons the mean-field approximation and predicts large capacitance, $C > C_H$, due to weak interaction of ion-image dipoles at the electrode surface. Further, MC simulations confirm that even for strongly asymmetric RTIL, where all ions are still mobile, our analytical predictions still apply.

Qualitatively, our theory explains all the main features of the experiment in Ref. [21]. The authors of Ref. [21] relate their observations to theories of so-called "pseudo-capacitance", a term used by Conway and coworkers for the rare cases of anomalously large EDL capacitance (see [49] and references therein). Pseudo-capacitance is said to result from specific adsorption of cations to the metal surface, where the cations are neutralized. In this sense Conway's theory is similar to ours. However, his theory of pseudo-capacitance does not explain what happens with the negative charge of excess anions, which remains in the bulk and which in our theory plays a pivotal role. The existing theory of pseudo-capacitance also does not explicitly specify the form of the repulsion between bound ions, and therefore does not arrive at a closed result. We take care to address both of these points in the present (OCP) model, and we arrive at definite predictions for capacitance. Thus, one may consider our theory to be an improved theory of pseudo-capacitance, if by this term one understands a capacitance larger than the Helmholtz value. We emphasize, however, that our theory does not assume any Faradaic effects, so that our result is in fact a standard capacitance and the

prefix "pseudo-" is unnecessary.

5.3 Attractive image charges without a metallic electrode

Chapter 4 confirmed the theoretical predictions made in Refs. [67, 22] for the distribution of multivalent Z-ions in the screening atmosphere around a highly charged macro-ion. In this theory, adsorbed Z-ions on the surface of the macroion form a strongly correlated liquid (SCL). The SCL acts as an effective metallic surface for Z-ions that stray from the macroion surface to distances larger than the average distance between Z-ions of the SCL. Using Monte Carlo (MC) simulations, we verified that a stray Z-ion is attracted to its electrostatic image created behind the effective metallic surface. As a small correction to [67, 22], however, our MC simulation showed that the effective metallic surface is not aligned with the average position of the adsorbed Z-ion's centers, but is slightly above the adsorbed Z-ion's centers. This offset was calculated analytically to be $|\xi|$, where 2ξ is the screening length of the SCL. Our analytic theory is in reasonable agreement with the MC data. Extending the original image theory of [67, 22], we demonstrated that the attractive image interaction, while screened, persists in a weak electrolyte.

In [70] the attractive image interaction, which we have studied here, was used to interpret the origin of the negative chemical potential of the condensed Z-ions (equation 4.15). As a stray Z-ion, attracted to its image, approaches the surface of the macroion it reaches a distance, $r \sim R_M + b$, where the SCL fails to act as a good metal and the correlation attraction $U_c(r)$ saturates at $\mu \sim -Z^2e^2/4\epsilon b$; this saturation can be seen in figure 4.5 as the growth of $\Delta U(r)$ at $r < 6.5$ nm. It is this negative chemical potential, brought about by the attractive image interaction, at $r \gtrsim R_{met} + b$, which drives charge inversion (over compensation of the macroion's bare charge with condensed Z-ions), a phenomenon that has generated much interest [67, 22, 78, 79, 73, 80, 69, 72, 81]. Thus, we believe that this paper helps to clarify the origin of charge inversion.

References

[1] G. Roza. *Potassium*. Rosen Central, 2007.

[2] Ronald A. Guidotti and Patrick Masset. Thermally activated ("thermal") battery technology: Part i: An overview. *Journal of Power Sources*, 161(2):1443–1449, October 2006.

[3] Z. Wang, G.F. Naterer, K.S. Gabriel, E. Secnik, R. Gravelsins, and V. Daggupati. Thermal design of a solar hydrogen plant with a copper-chlorine cycle and molten salt energy storage. *International Journal of Hydrogen Energy*, In Press, Corrected Proof:–, 2011.

[4] P. Walden. Molecular weights and electrical conductivity of several fused salts. *Bull. Acad. Sci. St. Petersburg*, 405:422, 1914.

[5] J. S. Wilkes and M. J. Zaworotko. Air and water stable 1 - ethyl - 3 - methylimidazolium based ionic liquids. *J. Chem. Soc. Chem. Commun*, 13:965967, 1992.

[6] J. Fuller, R. T Carlin, H. C De Long, and D. Haworth. Structure of 1-ethyl-3-methylimidazolium hexafluorophosphate: model for room temperature molten salts. *J. Chem. Soc., Chem. Commun.*, 3:299300, 1994.

[7] Philippe Hapiot and Corinne Lagrost. Electrochemical reactivity in room-temperature ionic liquids. *Chemical Reviews*, 108(7):2238–2264, 2008, http://pubs.acs.org/doi/pdf/10.1021/cr0680686. PMID: 18564878.

[8] Google scholar search - intitle:"molten salt", intitle:"ionic liquid". http://scholar.google.com, March 2011.

[9] M. J Earle and K. R Seddon. Ionic liquids. green solvents for the future. *Pure and applied chemistry*, 72(7):13911398, 2000.

[10] Maciej Galinski, Andrzej Lewandowski, and Izabela Stepniak. Ionic liquids as electrolytes. *Electrochimica Acta*, 51(26):5567–5580, August 2006.

[11] Yu Xia, Jeong Ho Cho, Jiyoul Lee, P. Paul Ruden, and C. Daniel Frisbie. Comparison of the mobilitycarrier density relation in polymer and single-crystal organic transistors employing vacuum and liquid gate dielectrics. *Advanced Materials*, 21(21):2174–2179, 2009.

[12] Alexei A. Kornyshev. Double-Layer in ionic liquids: paradigm change? *The Journal of Physical Chemistry B*, 111(20):5545–5557, May 2007.

[13] M. Gouy. Sur la constitution de la charge lectrique la surface d'un lectrolyte. *Journal de Physique Thorique et Applique*, 9(1):12, 1910.

[14] David Leonard Chapman. LI. a contribution to the theory of electrocapillarity. *Philosophical Magazine Series 6*, 25(148):475, 1913.

[15] O. Stern. Zur theorie der elektrolytischen doppelschicht. *Zeitschrift fr Elektrochemie*, 30:508–516, 1924.

[16] H. Helmholtz. Ueber einige gesetze der vertheilung elektrischer strme in krperlichen leitern mit anwendung auf die thierisch-elektrischen versuche. *Annalen der Physik und Chemie*, 165(6):211–233, 1853.

[17] H.L.F. von Helmholtz. Some laws concerning the distribution of electric currents in volume conductors with applications to experiments on animal electricity. *Proceedings of the IEEE*, 92(5):868–870, 2004.

[18] Md. Mominul Islam, Muhammad Tanzirul Alam, and Takeo Ohsaka. Electrical Double-Layer structure in ionic liquids: A corroboration of the theoretical model by experimental results. *The Journal of Physical Chemistry C*, 112(42):16568–16574, October 2008.

[19] Md. Mominul Islam, Muhammad Tanzirul Alam, Takeyoshi Okajima, and Takeo Ohsaka. Electrical double layer structure in ionic liquids: An understanding of

the unusual CapacitancePotential curve at a nonmetallic electrode. *The Journal of Physical Chemistry C*, 113(9):3386–3389, March 2009.

[20] Vera Lockett, Rossen Sedev, John Ralston, Mike Horne, and Theo Rodopoulos. Differential capacitance of the electrical double layer in Imidazolium-Based ionic liquids: Influence of potential, cation size, and temperature. *The Journal of Physical Chemistry C*, 112(19):7486–7495, May 2008.

[21] C.R. Mariappan, T.P. Heins, and B. Roling. Electrode polarization in glassy electrolytes: Large interfacial capacitance values and indication for pseudocapacitive charge storage. *Solid State Ionics*, 181(19-20):859–863, July 2010.

[22] B. I. Shklovskii. Screening of a macroion by multivalent ions: Correlation-induced inversion of charge. *Physical Review E*, 60(5):5802, November 1999.

[23] Muhammad Tanzirul Alam, Md. Mominul Islam, Takeyoshi Okajima, and Takeo Ohsaka. Measurements of differential capacitance in room temperature ionic liquid at mercury, glassy carbon and gold electrode interfaces. *Electrochemistry Communications*, 9(9):2370 – 2374, 2007.

[24] Muhammad Tanzirul Alam, Md. Mominul Islam, Takeyoshi Okajima, and Takeo Ohsaka. Capacitance measurements in a series of room-temperature ionic liquids at glassy carbon and gold electrode interfaces. *The Journal of Physical Chemistry C*, 112(42):16600–16608, 2008, http://pubs.acs.org/doi/pdf/10.1021/jp804620m.

[25] C. Nanjundiah, S. F. McDevitt, and V. R. Koch. Differential capacitance measurements in solvent-free ionic liquids at hg and c interfaces. *Journal of The Electrochemical Society*, 144(10):3392–3397, 1997.

[26] Maxim V. Fedorov and Alexei A. Kornyshev. Towards understanding the structure and capacitance of electrical double layer in ionic liquids. *Electrochimica Acta*, 53(23):6835 – 6840, 2008. EXPLORING FRONTIERS OF ELECTROCHEMISTRY Selection of papers from the 58th Annual Meeting of the International Society of Electrochemistry 10-14 September 2007, Banff, Canada.

[27] Maxim V. Fedorov and Alexei A. Kornyshev. Ionic liquid near a charged wall: Structure and capacitance of electrical double layer. *The Journal of Physical Chemistry B*, 112(38):11868–11872, 2008.

[28] M.V. Fedorov, N. Georgi, and A.A. Kornyshev. Double layer in ionic liquids: The nature of the camel shape of capacitance. *Electrochemistry Communications*, 12(2):296 – 299, 2010.

[29] Martin Trulsson, Jenny Algotsson, Jan Forsman, and Clifford E. Woodward. Differential capacitance of room temperature ionic liquids: The role of dispersion forces. *The Journal of Physical Chemistry Letters*, 1(8):1191–1195, 2010, http://pubs.acs.org/doi/pdf/10.1021/jz900412t.

[30] Stanislaw Lamperski and Jacek Klos. Grand canonical monte carlo investigations of electrical double layer in molten salts. *The Journal of Chemical Physics*, 129(16):164503, 2008.

[31] Jacek Klos and Stanislaw Lamperski. Electrical double layer properties in diameter asymmetric molten salt investigated by grand canonical monte carlo method. *The Journal of Physical Chemistry C*, 114(31):13329–13333, 2010, http://pubs.acs.org/doi/pdf/10.1021/jp104402u.

[32] M. S. Loth, Brian Skinner, and B. I. Shklovskii. Anomalously large capacitance of an ionic liquid described by the restricted primitive model. *Phys. Rev. E*, 82(5):056102, Nov 2010.

[33] John O'M. Bockris, Amulya K.N. Reddy, and Maria E. Gamboa-Aldeco. *Modern Electrochemistry 2A: Fundamentals of Electrodics*. Springer, 2nd edition, January 2001.

[34] Dezso Boda, Douglas Henderson, Kwong-Yu Chan, and Darsh T. Wasan. Low temperature anomalies in the properties of the electrochemical interface. *Chemical Physics Letters*, 308(5-6):473–478, July 1999.

[35] Dezso Boda, Douglas Henderson, and Kwong-Yu Chan. Monte carlo study of the capacitance of the double layer in a model molten salt. *The Journal of Chemical Physics*, 110(11):5346, 1999.

[36] Michael B. Partenskii and Peter C. Jordan. The admissible sign of the differential capacity, instabilities, and phase transitions at electrified interfaces. *The Journal of Chemical Physics*, 99(4):2992, 1993.

[37] Stanislaw Lamperski, Christopher W. Outhwaite, and Lutful B. Bhuiyan. The electric Double-Layer differential capacitance at and near zero surface charge for a restricted primitive model electrolyte. *The Journal of Physical Chemistry B*, 113(26):8925–8929, July 2009.

[38] Douglas Henderson, Stanisaw Lamperski, Christopher W. Outhwaite, and Lutful Bari Bhuiyan. A mean spherical approximation study of the capacitance of an electric double layer formed by a high density electrolyte. *Collection of Czechoslovak Chemical Communications*, 75(3):303–312, 2010.

[39] G. M. Torrie. Electrical double layers. II. monte carlo and HNC studies of image effects. *The Journal of Chemical Physics*, 76(9):4615, 1982.

[40] M. Alawneh and D. Henderson. Monte carlo simulation of the double layer at an electrode including the effect of a dielectric boundary. *Molecular Simulation*, 33(6):541, 2007.

[41] M Pounds, S Tazi, M Salanne, and P A Madden. Ion adsorption at a metallic electrode: an ab initio based simulation study. *Journal of Physics: Condensed Matter*, 21(42):424109, 2009.

[42] Christopher W Outhwaite and Lutful B Bhuiyan. An improved modified Poisson-Boltzmann equation in electric-double-layer theory. *J. Chem. Soc., Faraday Trans. 2*, 79:707–718, 1983.

[43] Christopher Outhwaite, Stanislaw Lamperski, and Lutful Bari Bhuiyan. Influence of electrode polarization on the capacitance of an electric double layer at and around zero surface charge. *Molecular Physics*, 109(1):21–26, 2011.

[44] Daan Frenkel and Berend Smit. *Understanding Molecular Simulation, Second Edition: From Algorithms to Applications*. Academic Press, 2 edition, November 2001.

[45] Yan Levin and Michael E. Fisher. Criticality in the hard-sphere ionic fluid. *Physica A: Statistical and Theoretical Physics*, 225(2):164–220, March 1996.

[46] J. Topping. On the mutual potential energy of a plane network of doublets. *Proceedings of the Royal Society of London. Series A, Containing Papers of a Mathematical and Physical Character*, 114(766):67–72, February 1927. ArticleType: research-article / Full publication date: Feb. 1, 1927 / Copyright 1927 The Royal Society.

[47] Mustafa Sabri Kilic, Martin Z. Bazant, and Armand Ajdari. Steric effects in the dynamics of electrolytes at large applied voltages. i. double-layer charging. *Physical Review E*, 75(2):021502, February 2007.

[48] Hector D. Abruna, Yasuyuki Kiya, and Jay C. Henderson. Batteries and electrochemical capacitors. *Physics Today*, 61(12):43, 2008.

[49] B. E. Conway. *Electrochemical supercapacitors: scientific fundamentals and technological applications*. Springer, 1999.

[50] C. A. Angell, C. Liu, and E. Sanchez. Rubbery solid electrolytes with dominant cationic transport and high ambient conductivity. *Nature*, 362(6416):137–139, March 1993.

[51] Brian Skinner, M. S. Loth, and B. I. Shklovskii. Capacitance of the double layer formed at the Metal/Ionic-Conductor interface: How large can it be? *Physical Review Letters*, 104(12):128302, March 2010.

[52] M. S. Loth, Brian Skinner, and B. I. Shklovskii. Non-mean-field theory of anomalously large double layer capacitance. *Physical Review E*, 82(1):016107, July 2010.

[53] V. Freise. Zur theorie der diffusen doppelschicht (theory of the diffuse double layer). *Zeitschrift fr Elektrochemie*, 56:822–827, 1952.

[54] Itamar Borukhov, David Andelman, and Henri Orland. Steric effects in electrolytes: A modified Poisson-Boltzmann equation. *Physical Review Letters*, 79(3):435, July 1997.

[55] T. T. Nguyen and B. I. Shklovskii. Adsorption of charged particles on an oppositely charged surface: Oscillating inversion of charge. *Physical Review E*, 64(4):041407, 2001.

[56] Keith B. Oldham. A Gouy-Chapman-Stern model of the double layer at a (metal)/(ionic liquid) interface. *Journal of Electroanalytical Chemistry*, 613(2):131–138, February 2008.

[57] Steven Baldelli. Surface structure at the ionic LiquidElectrified metal interface. *Accounts of Chemical Research*, 41(3):421–431, March 2008.

[58] Gerald D. Mahan. *Many Particle Physics*. Springer, 3nd edition, January 2000.

[59] M S Loth and B I Shklovskii. Non-mean-field screening by multivalent counterions. *Journal of Physics: Condensed Matter*, 21(42):424104, 2009.

[60] B. Widom. Structure of interfaces from uniformity of the chemical potential. *Journal of Statistical Physics*, 19(6):563–574, 1978.

[61] Bo R. Svensson and Clifford E. Woodward. Widom's method for uniform and non-uniform electrolyte solutions. *Molecular Physics: An International Journal at the Interface Between Chemistry and Physics*, 64(2):247, 1988.

[62] Stewart K. Reed, Oliver J. Lanning, and Paul A. Madden. Electrochemical interface between an ionic liquid and a model metallic electrode. *The Journal of Chemical Physics*, 126(8):084704, 2007.

[63] Carlos Pinilla, M. G. Del Ppolo, Jorge Kohanoff, and R. M. Lynden-Bell. Polarization relaxation in an ionic liquid confined between electrified walls. *The Journal of Physical Chemistry B*, 111(18):4877–4884, May 2007.

[64] Ingo Krossing and Ines Raabe. Noncoordinating AnionsFact or fiction? a survey of likely candidates. *Angewandte Chemie International Edition*, 43(16):2066–2090, 2004.

[65] M. Alawneh, D. Henderson, C. W. Outhwaite, and L. B. Bhuiyan. The effect of dielectric polarization of the electrode on anomalous temperature effects in the electrical double layer. *Molecular Simulation*, 34(5):501, 2008.

[66] J. Reszko-Zygmunt, S. Sokoowski, D. Henderson, and D. Boda. Temperature dependence of the double layer capacitance for the restricted primitive model of an electrolyte solution from a density functional approach. *The Journal of Chemical Physics*, 122(8):084504, 2005.

[67] V. I. Perel and B. I. Shklovskii. Screening of a macroion by multivalent ions: a new boundary condition for the Poisson-Boltzmann equation and charge inversion. *Physica A: Statistical Mechanics and its Applications*, 274(3-4):446–453, December 1999.

[68] Roland R. Netz. Debye-hückel theory for interfacial geometries. *Physical Review E*, 60(3):3174, 1999.

[69] A. G Moreira and R. R Netz. Strong-coupling theory for counter-ion distributions. *Europhysics Letters (EPL)*, 52(6):705–711, 2000.

[70] T. T. Nguyen, A. Yu. Grosberg, and B. I. Shklovskii. Screening of a charged particle by multivalent counterions in salty water: Strong charge inversion. *The Journal of Chemical Physics*, 113(3):1110, 2000.

[71] Y. Wang, K. Kimura, Q. Huang, P.L. Dubin, and W. Jaeger. Effects of salt on polyelectrolyte-micelle coacervation. *Macromolecules*, 32(21):7128–7134, 1999.

[72] Yoram Burak, David Andelman, and Henri Orland. Test-charge theory for the electric double layer. *Physical Review E*, 70(1):016102, July 2004.

[73] H. Boroudjerdi, Y.-W. Kim, A. Naji, R.R. Netz, X. Schlagberger, and A. Serr. Statics and dynamics of strongly charged soft matter. *Physics Reports*, 416(3-4):129–199, September 2005.

[74] K. Besteman, K. Van Eijk, and SG Lemay. Charge inversion accompanies DNA condensation by multivalent ions. *Nature Physics*, 3(9):641–644, 2007.

[75] P.L. Felgner. Nonviral strategies for gene therapy. *Scientific American*, 86(1):103, 1997.

[76] P.S. Kuhn, Y. Levin, and M.C. Barbosa. Charge inversion in DNA-amphiphile complexes: possible application to gene therapy. *Physica A: Statistical Mechanics and its Applications*, 274(1-2):8–18, 1999.

[77] M. Silva, P.S. Kuhn, and L.S. Lucena. DNA solutions with multivalent salts and amphiphiles. *Physica A: Statistical Mechanics and its Applications*, 296(1-2):31–41, 2001.

[78] A. Yu. Grosberg, T. T. Nguyen, and B. I. Shklovskii. Colloquium: The physics of charge inversion in chemical and biological systems. *Reviews of Modern Physics*, 74(2):329, April 2002.

[79] Yan Levin. Electrostatic correlations: from plasma to biology. *Reports on Progress in Physics*, 65(11):1577–1632, 2002.

[80] Ren Messina. Electrostatics in soft matter. *Journal of Physics: Condensed Matter*, 21(11):113102, 2009.

[81] Andr G. Moreira and Roland R. Netz. Binding of similarly charged plates with counterions only. *Physical Review Letters*, 87(7):078301, July 2001.

[82] Ioulia Rouzina and Victor A. Bloomfield. Macroion attraction due to electrostatic correlation between screening counterions. 1. mobile Surface-Adsorbed ions and diffuse ion cloud. *The Journal of Physical Chemistry*, 100(23):9977–9989, January 1996.

[83] Niels Grnbech-Jensen, Robert J. Mashl, Robijn F. Bruinsma, and William M. Gelbart. Counterion-Induced attraction between rigid polyelectrolytes. *Physical Review Letters*, 78(12):2477, March 1997.

[84] B. I. Shklovskii. Wigner crystal model of counterion induced bundle formation of rodlike polyelectrolytes. *Physical Review Letters*, 82(16):3268, April 1999.

[85] L D Landau, L. P. Pitaevskii, and E.M. Lifshitz. *Electrodynamics of Continuous Media, Second Edition: Volume 8*. Butterworth-Heinemann, 2 edition, January 1984.

[86] M. S. Bello, E. I. Levin, B. I. Shklovskii, and A. L. Efros. Density of localized states in the surface impurity band of a metal-insulator-semiconductor structure. *Soviet Physics - JETP*, 53:822, 1981.

[87] S. V. Kravchenko, D. A. Rinberg, S. G. Semenchinsky, and V. M. Pudalov. Evidence for the influence of electron-electron interaction on the chemical potential of the two-dimensional electron gas. *Physical Review B*, 42(6):3741, 1990.

[88] J. P. Eisenstein, L. N. Pfeiffer, and K. W. West. Negative compressibility of interacting two-dimensional electron and quasiparticle gases. *Physical Review Letters*, 68(5):674, February 1992.

[89] A. L. Efros. Negative density of states: Screening, einstein relation, and negative diffusion. *Physical Review B*, 78(15):155130, oct 2008.

[90] O. Lenz and C. Holm. Simulation of charge reversal in salty environments: Giant overcharging? *The European Physical Journal E*, 26(1-2):191–195, 2008.

[91] Alexandre Diehl and Yan Levin. Smoluchowski equation and the colloidal charge reversal. *The Journal of Chemical Physics*, 125(5):054902, 2006.

[92] Alexandre Diehl and Yan Levin. Colloidal charge reversal: Dependence on the ionic size and the electrolyte concentration. *The Journal of Chemical Physics*, 129(12):124506, 2008.

[93] M. Quesada-Prez, A. Martn-Molina, and R. Hidalgo-lvarez. Simulation of electric double layers undergoing charge inversion: mixtures of mono- and multivalent ions. *Langmuir*, 21(20):9231–9237, 2005.

[94] Alberto Martin-Molina, Jose Alberto Maroto-Centeno, Roque Hidalgo-Alvarez, and Manuel Quesada-Perez. Testing one component plasma models on colloidal overcharging phenomena. *The Journal of Chemical Physics*, 125(14):144906, 2006.

[95] Hiroo Totsuji. Numerical experiment on two-dimensional electron liquids. thermodynamic properties and onset of short-range order. *Physical Review A*, 17(1):399, January 1978.

[96] Alexandre P. dos Santos, Alexandre Diehl, and Yan Levin. Electrostatic correlations in colloidal suspensions: Density profiles and effective charges beyond the PoissonBoltzmann theory. *The Journal of Chemical Physics*, 130(12):124110, 2009.

[97] Tsuneya Ando, Alan B. Fowler, and Frank Stern. Electronic properties of two-dimensional systems. *Reviews of Modern Physics*, 54(2):437, April 1982.

[98] Hiroyuki Ohshima. Electrostatic interaction between two spherical colloidal particles. *Advances in Colloid and Interface Science*, 53:77–102, September 1994.

[99] Lars Onsager and Nicholas N. T. Samaras. The surface tension of Debye-Huckel electrolytes. *The Journal of Chemical Physics*, 2(8):528, 1934.

[100] S Kondrat and A Kornyshev. Superionic state in double-layer capacitors with nanoporous electrodes. *Journal of Physics: Condensed Matter*, 23(2):022201, 2011.

[101] Brian Skinner, Tianran Chen, M. S Loth, and B. I Shklovskii. Theory of volumetric capacitance of an electric double layer supercapacitor. *1101.1064*, January 2011.

Appendix A

Acronyms

Care has been taken in this thesis to minimize the use of jargon and acronyms, but this cannot always be achieved. This appendix contains a table of acronyms and their meaning.

A.1 Acronyms

Table A.1: Acronyms

Acronym	Meaning
EDL	Electric double-layer
RTIL	Room temperature ionic liquid
$C(V)$	Capacitance as a function of voltage
GCS	Gouy-Chapman-Stern
PB	Poisson-Boltzmann
C_H	Helmholtz Capacitance
RPM	Restricted primitive model
PM	Primitive model
MC	Monte Carlo
OCP	One component plasma

Appendix B

Potential derivation

B.1 Calculation of the total potential

This appendix gives a formal derivation of Eq. 4.22. Starting from,

$$\nabla^2\psi\left(\varrho,x'\right)=-\frac{4\pi}{\varepsilon}\rho_{ext}(\varrho,x')+\frac{1}{\xi}\psi(\varrho,x_c)\delta(x'-x_c), \tag{B.1}$$

I introduce

$$\psi(\varrho,x')=\int_0^\infty kA_k(x')J_0(kr)dk, \tag{B.2}$$

and specify that,

$$\rho_{ext}=Ze\delta(\varrho)\delta(x'-x)/\pi\varrho, \tag{B.3}$$

Upon substitution one obtains, in cylindrical coordinates,

$$\nabla^2\int_0^\infty kA_k(x')J_0(k\varrho)dk=-\frac{4\pi}{\varepsilon}Ze\frac{\delta(\varrho)}{\pi\varrho}\delta(x'-x)+\frac{1}{\xi}\int_0^\infty kA_k(x_c)J_0(k\varrho)\delta(x'-x_c)dk. \tag{B.4}$$

Applying the cylindrical Laplacian operator in the L.H.S of Eq. B.4 gives,

$$\frac{\partial^2}{\partial x'^2}\int_0^\infty kA_k(x')J_0(k\varrho)dk-\int_0^\infty k^3A_k(x')J_0(k\varrho)dk, \tag{B.5}$$

where I have used

$$\frac{1}{\varrho}\frac{\partial}{\partial\varrho}\left(\varrho\frac{\partial}{\partial\varrho}J_0(k\varrho)\right)=-k^2J_0(k\varrho). \tag{B.6}$$

Both sides of Eq. B.4 are multiplied by $rJ_0(k\varrho)$ and radially integrated from zero to infinity, and after applying

$$\int_0^\infty J_0(k\varrho)\delta(\varrho)d\varrho=\frac{1}{2} \tag{B.7}$$

$$\int_0^\infty J_\nu(k\varrho)J_\nu(k'\varrho)\varrho d\varrho = \frac{1}{k}\delta(k-k'), \tag{B.8}$$

the result is

$$\frac{\partial^2}{\partial x'^2}A_k(x') - k^2 A_k(x') - \frac{2}{\xi}A_k(x_c)\delta(x'-x_c) + \frac{2Ze}{\varepsilon}\delta(x'-x) = 0. \tag{B.9}$$

Using the fourier transform of $A_k(x')$,

$$A_k(x') = \frac{1}{\sqrt{2\pi}}\int_{-\infty}^{\infty} e^{iyx'}A_k(y)dy. \tag{B.10}$$

one can rewrite Eq. B.9, and solve for the fourier transform of $A_k(x')$,

$$\frac{1}{\sqrt{2\pi}}\int_{-\infty}^{\infty} e^{iyyx'}A_k(y)dy = \frac{1}{(iy)^2-k^2}\left(\frac{1}{\xi}A_k(x_c) - \frac{2Ze}{\varepsilon}e^{iyx}\right). \tag{B.11}$$

Applying the inverse fourier transform to both sides of Eq. B.11 gives

$$A_k(x') = -\frac{A_k(x_c)}{\xi k}e^{-kx'} + \frac{Ze}{\varepsilon k}e^{k(x'-x)}, \tag{B.12}$$

where,

$$A_k(x_c) = -\frac{Ze}{\varepsilon}e^{-kx_c}\frac{1}{k+1/\xi}. \tag{B.13}$$

Upon substituting $A_k(x')$ into Eq. B.2, the final solution is obtained for the system's electrostatic potential as a function of the coordinates ϱ and x',

$$\psi(\varrho,x') = \frac{Ze}{\varepsilon}\int_0^\infty \left(e^{k(x'-x)} - \frac{1}{2k\xi+1}e^{-k(x'+x-2x_c)}\right)J_0(k\varrho)dk. \tag{B.14}$$